DROPLET - POWDER IMPACT INTERACTION IN THREE DIMENSIONAL PRINTING

by

TAILIN FAN

B. S., Beijing University of Agricultural Engineering, 1982
M.S., McGill University, 1985

Submitted to the Department of Mechanical Engineering
in Partial Fulfillment of the Requirements
for the Degree of

Doctor of Philosophy
in Mechanical Engineering

at the

MASSACHUSETTS INSTITUTE OF TECHNOLOGY

September 1995

Signature of Author _____
Department of Mechanical Engineering

Certified by _____
Emanuel M. Sachs
Associate Professor of Mechanical Engineering
Laboratory for Manufacturing and Productivity
Thesis Supervisor

Accepted by _____
Ain A. Sonin
Chairman of Graduate Committee

DROPLET - POWDER IMPACT INTERACTION IN THREE DIMENSIONAL PRINTING

by

TAILIN FAN

Submitted to the Department of Mechanical Engineering
on August 25, 1995
in partial fulfillment of the requirements for the degree of
Doctor of Philosophy in Mechanical Engineering

ABSTRACT

Three Dimensional Printing builds solid objects using computer-controlled inkjet printing of a liquid binder into powder materials. Typically, binder droplets size of tens of microns in diameter impinge at a speed ca. 10 meters per second on a loosely laid-out powder bed. The liquid binder mixes with the powder to form particulate aggregates and then connects them into the designed shape. It was found that powder bed deformation and powder ejection occur under these conditions. The connections between droplet-powder bed impact and the qualities of printed parts were studied. The surface texture of printed parts was modified through control of the cohesive strength of the powder bed. Microscopic observations of the impact of single droplets on various powder beds were carried out using stroboscopic photography. The impact speed of each droplet was measured individually. Micrographs of the impact events revealed that particulate aggregates, surrounded by an impact crater of a diameter ca. 300 micrometers, were formed in ca. 1 millisecond. The impact behavior of a single droplet on a deformable powder medium was analyzed and compared with impact phenomena of various other material systems. A model was formulated based on these findings to describe the development of the aggregate and its penetration into the powder bed. The model was used to predict the final depth of the aggregate based on measurable powder bed and impact parameters. These predictions fit well with experimental measurements made with varied impact speeds and powder materials. The study of single droplet impact on loose powder beds provides insights into binder-powder interaction at a microscopic level. The penetration model can be used as an effective tool in investigations for determining optimal printing conditions. This study represents the first time photographic observation and modeling of single droplet impact on deformable particular media were performed at the aforementioned temporal and spatial scales.

Thesis Supervisor:	Dr. Emanuel M. Sachs
Title:	Associate Professor of Mechanical Engineering
Thesis Committee:	Professor Michael J. Cima, Department of Material Science;
	Professor Ain A. Sonin, Department of Mechanical Engineering

This thesis is dedicated to my mother and late father,
who instilled in me their values and aspirations for higher learning,
and my wife, Shu Zhang, who with my son Rui have stood by me all these years
and have lent me the strongest support each and every day.

ACKNOWLEDGMENTS

My sincere thanks goes to my thesis advisor, Professor Emanuel Sachs, who established and led our research project into one of the most active programs at MIT. I am grateful for his guidance and inspiration. Without his strong support, this thesis could not have taken on its present form. I extend to him my best regards and wishes.

I would also like to thank the members of my thesis committee, Professor Michael Cima of the Department of Material Science, and Professor Ain Sonin of the Department of Mechanical Engineering, for their invaluable suggestions and ideas in the development of this thesis.

The skill and dedication of our research staff, David Brancazio and James Serdy, are assets to the project every student in the group immensely appreciates. I thank them for all their help and friendship. Former staff Tim Anderson's contribution to experiment instrumentation is very gratefully recognized.

It is a joyous experience to work in a coherent research team as vibrant as the one which converged at Three Dimensional Printing. I feel fortunate to have had the companionship of each of these students: Tara Arthur, Won Bang, Scott Borland, Jain Charnnarong, Seth Close, Alain Curodeau, Mark Eichler, Bugra Giritlioglu, Jason Grau, Honglin Guo, Haeseong Jee, Satbir Khanuja, Anne Kohnen, John Lee, Steve Michaels, Daniel Nammour, Chris Richardson, David Robinson, Mike Rynerson, Christopher Shutts, Chris Stratton, Earl Sun, Hon Tang, Gail Thornton, Ben Wu, Ed Wulonis and Jae Yoo. Your work has not only printed itself into those little white parts, but also into my fondest memory.

It is impossible to list all of the numerous support staff. A special thanks goes to Fred Cote for his outstanding machine shop supervision job. If there be an award for "Friend to Researchers" at MIT, Fred is the first one I would nominate.

Finally, the very reason I could have completed this work: my family. My parents blessed me, their youngest son, with their deepest love. My brothers' and sisters' care for my mother in her advanced age made it possible for me come across the ocean to MIT. I

always will be indebted to my wife, Shu, and my son, Rui, for the sacrifices they have made in these many years. While taking care of me, and raising a son, Shu has managed to put herself through college and graduate school. Shu, by the time you get your Ph.D. at Harvard next year, you will have in truth accomplished a work many times as much. To all my beloved family, thank you so much.

TABLE OF CONTENTS

LIST OF FIGURES

LIST OF TABLES

CHAPTER 1

INTRODUCTION

1.1 The Three Dimensional Printing Process

Rapid prototyping technologies are a new category of computer aided manufacturing processes. Three Dimensional Printing (3DP) is one of them. 3DP shares a common technological feature with other rapid prototyping technologies, that is, to build three dimensional objects directly using information derived from the CAD file of the objects, and by adding and bonding materials to them in a successive manner. As with most of these technologies, a layer-by-layer additive strategy is adopted, which builds three dimensional objects in a sequence of two dimensional layers, each layer representing one of the cross sections of the object under construction. This strategy simplifies and standardizes the processing of CAD data and creates a condition in which complicated geometry can be produced through repetitive execution of the same type of operation throughout the building process. This unified approach makes it possible for the machine hardware and software developers to anticipate and resolve most of the complexities in data processing, material handling and object building, and to make the manufacturing process a routine turnkey operation. Then the designers will be able to concentrate on their design work without being concerned by the manufacturing issues. Research and development is carried out at MIT to fully explore the potentials and constraints of the Three Dimensional Printing process. The goal is to establish an scientific and technological foundation of the process, so that 3DP systems can be developed to the point that the printing one day does become a turnkey operation.

Three Dimensional Printing builds parts from fine powder particles. Figure 1.1 illustrates the printing cycle. The powder is spread over a powder bed by a roller in thin layers of a thickness about 200 μm. The particles are selectively bonded by a liquid binder, which is dispensed in streams of discrete tiny droplets by a printhead similar to those used in ink-jet printing. The printhead passes the powder bed in a pattern of raster scanning (Figure 1.2). Turning the binder droplet stream on and off is controlled by the cross-

sectional data generated from the CAD model. After a cross section of the part is printed, the movable bottom of the powder bed is lowered by one layer of thickness and fresh powder is added to the top to create a new layer for printing. The printing cycle is repeated until all of the cross sections of the part are printed.

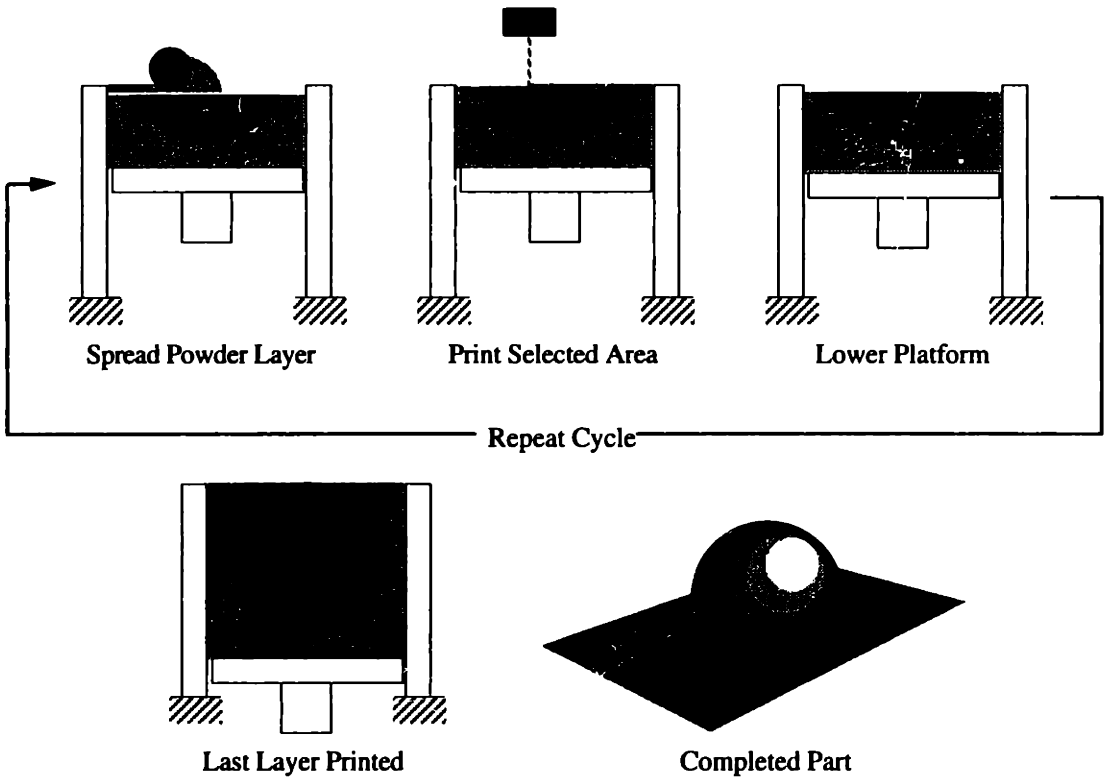

Figure 1.1 Operational sequence in Three Dimensional Printing.

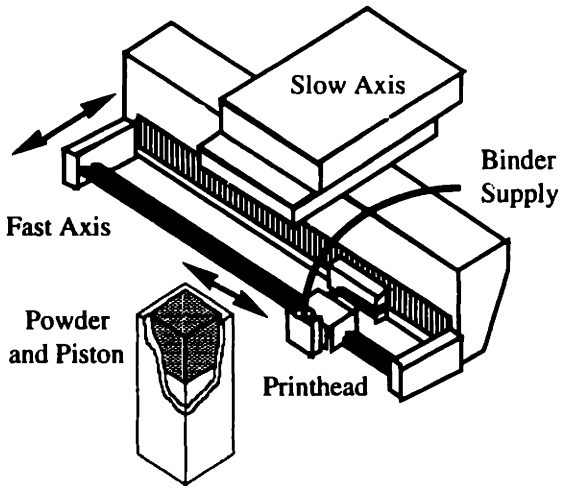

Figure 1.2 Printing motions in 3DP

Throughout the printing operation, unbound particles are left in place to support the unconnected printed regions. These particles are removed during post-processing after the printing is completed. The exact post processing method depends on the powder and binder materials used. It normally involves thermal cycles of heating and sintering, which strengthen the bonds between powder particles and give the printed part mechanical strength required by its function.

The usage of powder and liquid binding materials makes Three Dimensional Printing a highly versatile manufacturing process. Parts can be built directly with materials proper for its final usage. Many potential applications are under study to take this advantage. Alumina powder with colloidal silica binder is used in direct production of high temperature molds for metal casting [Sachs, et al.]. Stainless steel powder with latex emulsion binder is used to produce metal matrix preforms. After being infiltrated with metal alloys, these preforms can be used as injection molds to produce polymer products. Bio-compatible polymer materials can be printed with solvents to produce medical devices. Besides printing binder, active materials can also be introduced into the structure by further injection. Hormones and other drugs can be printed into porous structures made by Three Dimensional Printing to produce controlled-release drug delivering systems.

1.2 Impact Interaction between Binder Droplets and Powder Beds

Three Dimensional Printing uses continuous ink-jet printheads to dispense liquid binder in streams of droplets. Typically the droplets are 80 μm in diameter, generated at the rate of 60,000 drops per second. When printed into a powder bed individually, each droplet will create an aggregate of powder particles. It is called a "primitive ball" in this thesis. In raster scanning printing, the droplets are printed consecutively with certain spatial overlapping to ensure the aggregates to form into a linear structure. The linear structure will be referred to as a "primitive line" hereafter. A layer of the part is printed line by line through repeated raster scanning. These primitive lines within a layer and between layers are bound together by binder liquid migrated through their boundaries. This action is called "stitching." A part will delaminate or crack without the stitching. Sufficient stitching is very important to forming an integral part.

The droplets reach the powder bed with a speed about 9 - 10 m/sec. The droplet velocity is primarily determined by the flow rate and nozzle size. Flow rate determines the rate at which the part is printed; higher flow rate is necessary in order to increase throughput. Smaller nozzle is essential for producing smaller droplets; smaller droplets are required for reducing the minimal printed feature size. To have higher production rate and fine features, the droplet speed needs to be correspondingly high. Meanwhile, droplets at higher speed reach powder bed in less time and subject to less air disturbances, which helps increase the placement accuracy of the droplets.

However, higher droplet speed also creates problems. The main problem associated with high speed printing is the deformation of the powder bed caused by droplet impact. Powder beds employed in Three Dimensional Printing prior to when this study was started were prepared by piling up powder loosely and leveling it by counter-rolling. The packing density of these beds were around 40%. Without other locking mechanisms, the powder particles stayed put mainly due to gravity and inter-particle friction. These beds were a delicate medium, susceptible even to pressures as minute as that from impact by microscopic droplets. Printing disturbed the powder bed, and the disturbed bed structures were transfixed into the part being built. Droplet impacts has a profound influence on the

quality of printed parts. Among the quality issues related to droplet impacts are the surface quality, the dimensional accuracy, and the integrity of the part.

This research is a study on how the liquid droplet interacts with a loose powder bed in the context of Three Dimensional Printing. The primary goal is to understand the implications of droplet impact interaction with the powder bed on 3DP process and the quality of its products. Raster-scanning printing of droplets on loose powder beds were closely observed and the resulted part structures were examined. Conclusions drawn from these observations were confirmed by new-rounds of printing with specially designed powder bed conditions. In order to delineate the most important mechanisms involved in the droplet-powder impact interaction, we took an approach of examining the interaction between a single droplet and the powder bed, with the assumption that the mechanisms delineated from this study are also at work when multiple droplets interact with the powder bed. Single droplet impacts were studied in this research first by high-speed single-frame stroboscopic photography. Then, based on the observations, we constructed a model to describe the formation of a primitive ball structure and its penetration into the powder bed. This model predicts through simulation what the penetration depth will be based on the properties of the liquid droplet and the powder bed. Further impact experiments were conducted to compare the model prediction with the observed penetration data.

1.3 Characteristics of the Material System

Droplet impact on powders in general may occur to vastly different material systems under very broad ranges of impact conditions. This study has been conducted to understand those problems encountered in producing ceramic molds for metal casting by Three Dimensional Printing. The material properties and parameters are within the scope relevant to this application in its current stage of development.

In Three Dimensional Printing, as in any printing, it is vital to select the liquid agent and the medium being printed so that the liquid would be able to adhere to the printing medium. The material studied in this research are water based solutions and alumina powder. Under normal conditions, water and water based solutions wet the alumina particles very well. Liquid-powder impact under non-wetting conditions is not within the scope of this study.

Three Dimensional Printing has been primarily developed for industrial applications. Minimum feature size, surface finish and dimensional accuracy are major performance indices. Their limits are determined by the size of the droplet and size of the powder particles, whichever is larger. So the application requirements set a limit to the maximum sizes of droplet and powder particles. Except for special applications, droplet larger than a few hundred micrometers and powders in a similar range may not produce structures fine enough to satisfy these requirements.

The lower limit of the particle size arises from powder handling issues. Powders with particle size of one micrometer or smaller exhibit high cohesive strength [Kendall]. These powders cannot be spread into thin layers unless they are granulated into larger granules or suspended in liquid first. The size of power particles used in Three Dimensional Printing is in the range of a few microns to 30 microns. This is also the particle size range studied in this research.

The lower limit on droplet size is a more complicated issue. Even though reducing the size of droplets has the potential of producing finer features and achieving higher dimensional accuracy in printed parts, this method is only effective before that the droplet size gets so small that the size of powder particles becomes the dominating factor in determining minimal feature size. Meanwhile, since producing smaller droplets requires using nozzles of smaller opening, there are always certain practical limitations from nozzle considerations on the droplet size reduction. In Three Dimensional Printing, the liquid binders carry solid particles of one kind or another as the active binding agent; nozzle clogging causes concern when these binders are used with small nozzles. On the current 3DP machine, nozzles with diameters of 40 microns or larger work satisfactorily over a long period of time in producing droplets of the size around 80 microns in diameter. Consequently, this study focuses on droplets in this size range.

It was mentioned before that alumina powder beds in Three Dimensional Printing typically have packing densities in the range 35 - 40% for the flaky powder and higher for spherical powder due to the natural tendency of the latter to flow better. The average pore size, the size of voids in between particles, is often found to be around 5 μm. A primary effort in the five-year history of Three Dimension Printing has been developing a printing

machine and a process for producing porous alumina molds used in metal casting, the characteristics of the powder bed as described have been kept as described because they are found suitable for the mold application. The porous structure facilitates channels for gas to escape during the casting and makes it easy to remove the shell after the casting. It was on these powder beds that the powder bed deformation due to droplet impact drew the attention of research and motivated this study. This study focuses on the impact behavior of deformable powder beds. Powder beds strengthened by methods designed to eliminate the deformation are not in the scope of the model developed in this study.

1.4 Contributions of This Research

In the domain of impact research, this thesis for the first time studied the impact interaction between microscopic droplets and semi-infinite porous media consisted of fine particulate solids. The impact process of such system were photographed and modeled for the first time. Previous and current impact studies in all fields mostly focus on the deformation of the projectile and/or penetration of the targets; this study is original as it found and emphasized on the constructive aspect of the impact phenomena within its material system, that is, the formation of a granulate structural element. This led to a unique approach of modeling the cratering process, given in Chapter 5.

In the domain of Three Dimensional Printing research and development, work reported in this thesis for the first time identified the connection between droplet-powder impact interaction and major quality issues in 3DP. This research provides a framework for exploring various methods to control droplet-powder interaction and refine the printing process.

1.5 Organization of the Thesis

The research summarized in this thesis was motivated by a desire to minimize the adverse effects associated with droplet impacts and to take advantage of any useful effects the impacts may offer. We started with observing the consequences of the droplet's impact in terms of the geometric features rendered to the primitive structures. Chapter 2 discusses these observations, with an emphasis on how the powder bed modification changes the

results of the interaction. Findings in this chapter point to the necessity of examining a single droplet's impact on a loose powder bed closely.

A high-speed single-frame stroboscopic photography study on single droplet impacts on loose powder is discussed in Chapter 3. The equipment developed for this study and the experimental procedures are described. This study allows visualization of the fast dynamic process which finishes in a time less than one millisecond. The findings in this chapter provide the experimental evidences for constructing a model to delineate the impact process.

Studies found in existing literature are mostly for material systems different from that concerned in this research. Studies on impact phenomena between liquid droplets and fine powders at the geometric and time scales covered in this thesis have not yet been found in any literature. Chapter 4 cross references literature found in subject areas adjacent to the research on droplet - loose powder impact. Impact phenomena have been broadly studied in many fields, with either practical or theoretical interests. Comparing the similarities and differences of the phenomena, and investigating the state of affairs in these fields provide the background information for the modeling and experimental actions discussed in the next two chapters.

A penetration depth model for the primitive ball formed by a single droplet's impact in a loose powder bed is developed in Chapter 5. It draws on the experimental evidences discussed in Chapter 3, and contrasts them with impact observations reported on different material systems. The model approximates the penetration process as one in which the droplet mixes with powder along the way as the mixture moves into the powder bed. Viewing the mixture as one system and the surrounding powder particles as another, the model uses the principle of momentum conservation and considers the dissipating effect of the powder bed's resistance to penetration to derive the equation of motion of the droplet - powder mixture.

Chapter 6 discusses the experiment on penetration depth of the primitive ball structure. After an account of the equipment which was developed for powder sample testing and experimental procedures, the observed penetration data are compared with the predictions made by the simulation based on the model given in Chapter 5. A discussion

on the comparison and further exploration of the model is given. The findings from the experiment and the simulation of a single droplet is used to interpret phenomena found in multiple droplet impact on powder beds in Three Dimensional Printing.

Chapter 2

IMPACT PHENOMENA AND TOPOGRAPHY OF 3DP PARTS

2.1 Introduction

Primary applications of Three Dimensional Printing are direct productions of ceramic molds for metal casting and metal tooling for injection molding. These applications demand a high degree of control over part dimension and surface finish. For example, the surface of casting cores or molds should have a roughness RMS value in the range 1.3 to 3.0 μm.

The texture and roughness of a surface on a manufactured object are determined by the process by which the object is produced. The surface quality is the product of the processing method, tool geometry, material properties of the tool and the work piece, and the operating conditions. Variations of these factors cause changes to the physical and/or chemical processes and produce different surface textures and roughness.

The achievement of fine surface finish is a challenge for all rapid-prototying techniques based on additive processes. These additive processes share a common feature in that the layered building procedure produces stepped surfaces on the sides of the product. Limitations on the production rate and physical processes often require the layer thickness to be in the range of 76 μm to 254 μm. These layers are clearly evident in the form of a surface relief with an approximately constant period.

There are other factors that affect the texture of all surfaces, regardless of their shapes, orientation and location. In Three Dimensional Printing, the granular nature of the bulk material and the interactions between the binder and powder are such factors. The ink-jet printing action is accompanied by a plethora of phenomena: the mechanical impacts of the binder droplets on the powder bed, the capillary forces acting on the powder particles, the percolation of the liquid binder through the pore networks, and the phase change of the binder in the powder bed.

When printing is done on a loose powder bed by raster-scanning, the binder droplet impact interaction with the powder and the binder deposition pattern give the part surfaces a distinctive, corrugated texture, which accounts for the major part of the surface roughness on horizontal surfaces. This chapter describes experimental findings in how the topography of parts produced by this process are influenced by droplet impacts under various powder bed conditions.

2.2 A Geometric-Physical Model of Three Dimensional Printing Process

In order to study how the physical printing process affects the final quality of products of Three Dimensional Printing, it is helpful to formulate a geometric-physical model of the printing process. The model is geometric in the sense that it conceptually breaks down a printed part into basic constituent elements; and that the overall geometric character of the part are interpreted in terms of the generic geometric characteristics of these elements. In this respect an analogy can be drawn between Three Dimensional Printing and computer graphics. A raster scanned screen image in computer graphics is a collection of pixels of uniform shape and varied brightness. A part created by Three Dimensional Printing also consists of fundamental units which may not be further broken down. The geometric view provides us with a framework for analyzing and designing part characteristics such as surface textures without going into details of the physical process.

On the other hand, the model is physical by emphasizing that the geometric idealization is constrained by physical limitations. In other words, the geometric primitives have volumes and shapes determined by the physical process. Knowing what are physically realizable and their required conditions are especially important for design and improvement of the printing process.

Three Dimensional Printing by raster scanning creates parts in a hierarchy of three levels of primitive structures. The smallest primitive structure is an aggregate of powder particles, bonded together by a single droplet. The experimentally observed shape of such aggregates is roughly spherical. It is called a "primitive ball" in this thesis. Figure 2.1 shows a scanning electronic microscope (SEM) photograph of a primitive ball, made of alumina powder (nominal size 30 μm), photographed by Alan Lauder. These primitive balls were created by printing droplets in large drop-to-drop spacing to avoid overlapping of droplets. The general spherical shape of these powder aggregates is apparently due to

the capillary forces of the liquid binder which act on the powder particles and pull them together. The powder particles shown in this photograph are in fact platelets of irregular shapes. It appears from the photograph that the particles on the surface of the primitive ball are oriented in a way conforming to the spherical shape of the liquid droplet. This suggests that there was substantial particle rearrangement while the primitive ball was formed.

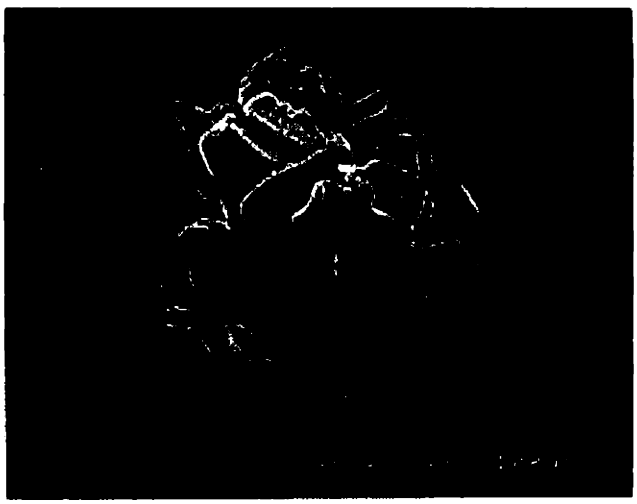

Figure 2.1 A primitive ball (30 μm Al_2O_3 powder).

When a succession of liquid droplets is printed with drop-to-drop spacing smaller than the droplet diameter (overlapping), the result is a filament structure. It is referred to in this thesis as a primitive line. The longitudinal geometry of the primitive line depends on the extent of droplet overlapping. If the droplets are deposited a droplet's diameter apart, the line structure will become a string of primitive balls, marginally connected on either ends. This will lower the mechanical strength of the part. In Three Dimensional Printing, mechanical strength is ensured by sufficient droplet overlapping. Typically, the machine executes raster scanning at a speed of 1.5 m/sec. and generates 60,000 droplets per second. Under this condition, the drop-to-drop distance is 25 μm. Given a droplet size of 80 μm, three droplets will partially overlap each other over the distance of one droplet diameter. Figure 2.2 shows primitive line created this way [Lauder]. It appears that the droplet overlapping greatly diminished diameter variations along the line.

Figure 2.2 A primitive line (320 grit Al_2O_3 powder).

Two more features of the primitive line in Figure 2.2 are noteworthy. The curved top of the line suggests that the line is cylindrical. This is a common feature of primitive lines created in loose powder beds. The circular cross section has the same origin as the spherical primitive balls. Capillary forces and particle rearrangement are essential in rendering this cylindrical geometry. The importance of powder particle mobility in forming this shape becomes obvious by comparing Figure 2.2 with primitive lines created in cohesive powder beds shown in figures of later sections, e.g. Figure 2.8.

The third important feature in Figure 2.2 is that the primitive line was situated in a groove, with its top lower than the original top surface of the powder bed, and was also separated from the side walls by a gap. The groove was created by powder ejection induced by droplet impacts, as discussed in the remaining sections of this chapter, and by the downward movement of the primitive structure into the powder bed, which is also resulted from droplet impacts, and will be discussed in the later chapters of this thesis.

The third level of primitive structure is created when primitive lines are printed side by side. The liquid binder permeates through the lines and 'stitches' them together to form a primitive sheet. The primitive sheet has an outline representing a cross section of the part under construction. Each primitive sheet printed by raster scanning can be viewed as an ensemble of primitive lines with some overlapping between the lines. By stacking these sheets together and binding them with percolating liquid binder, the three dimensional geometry of a part is rendered.

2.3 Impact Cratering and Topography of Primitive Sheets

The importance of impact cratering during Three Dimensional Printing was identified in the course of a study aimed at improving the smoothness of top surfaces of printed parts [Fan, et al., 1992]. By examining the printing process closely, it became obvious that the binder liquid jet of a speed of around 10 meters per second caused substantial powder particle movement. This finding was further supported by evidences collected through stroboscopic photographs of the printing process.

A 35 mm SLR camera took photographs of the target area back-lighted by a strobe flash of 0.7 microsecond duration. The strobe light was triggered by the same computer program controlling the scanning motion of the printhead. The horizontal field of view was 13 mm. It took 9 ms for the printhead to travel through this field. Figure 2.3 shows the printing in action on a loose powder bed. From the photograph it is seen that powders were ejected into the air, and did not settle until 6 ms after the printing stream passed the site.

Figure 2.3 Printing on a loose powder bed.

The groove around the printed line (Figure 2.2) was the result of this process. Figure 2.4 further illustrates the structure of the groove. On each side of the primitive line

a gap separates the primitive line from the wall of the groove. This created a barrier inhibiting the lateral capillary movement (leaking) of the liquid into the powder bed. The result is that primitive lines printed on loose powder beds have better lateral definition. On the other hand, the existence of the gap sets a lower limit for line spacing: even if another line is intended to be printed right beside the line first printed, there would not be enough powder available at the gap region to form the new line.

On the rims of the trench, the ejected powder particles pile up irregularly. Since the rim is the place where the next line will be printed, the irregularity of the pile-up will be transfixed into the new primitive line. Consequently, printing of a loose powder bed is mostly done on a surface which is incessantly disturbed by the on-going printing process. It is clear from observing the printing of single primitive line that impact cratering has an adverse effect on the surface structure of printed part.

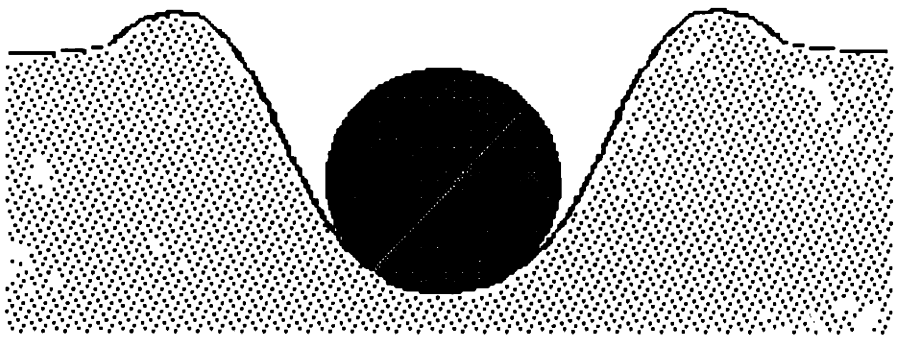

Figure 2.4 Impact cratering disturbs the powder bed surface.

Figure 2.5 shows the top surface of a sample printed on a loose powder bed. The corrugated surface texture found here is an artifact of the raster pattern and primitive line formation. The part was printed with a line spacing of 178 micrometers. Surface profiles measured across the printing direction featured corrugation with a period corresponding to the printing line spacing, upon which a height variation of higher frequency but smaller amplitude (in the range of particle size) is superimposed. The procession of regular corrugation is speckled with peaks or valleys of exceptional size, so that out-of-range cut-offs are often seen on the printouts of a profilometer (DekTak II) with a maximum measurement range ± 15 μm. The Ra values of those profiles are larger than 15 μm.

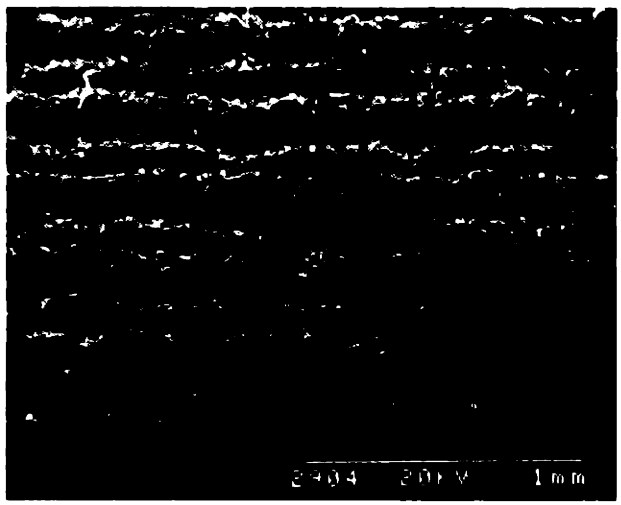

Figure 2.5 A surface printed on a loose powder bed.

While the high-frequency, smaller-amplitude random raggedness reflects the size and shape of the individual particles, the exceptionally large peaks and valleys in the surface profile can be attributed to the ejection-induced powder pile-up. Crooked or broken sections, uneven width and humps can be found along such lines. On the surface, these blemishes degrade the surface quality; when built into the part, they become bulk defects affecting the part integrity.

In order to show that a larger portion of the roughness of parts printed on loose powder beds was attributable to the excessive particle ejection incurred by printing impacts, printing experiments were conducted in which the powder movements were restrained. These experiments, described in the next section, produced parts featuring much more regular surface textures.

2.4 Surface Roughness Dependency on Powder Particle Retention

Based on the assumption that the irregularities on the horizontal surfaces of printed parts originate from the impact-cratering induced powder particle movements, two methods were developed to counteract the printing impacts. Experiments were conducted to examine the effects of these methods. The approach was to increase the cohesive strength of the powder bed, so that the powder particles would be by and large kept in place when they were subjected to the impacts of binder droplets.

2.4.1 Printing on Steamed Powder Layers

The first method experimented was to increase the powder bed cohesive strength by introducing moisture into the powder bed. Steam was generated by an electric heater and guided onto the powder bed surface by a hood made of polymer foam board. The steam flow was directed towards the wall of the hood, so that large droplets in the steam would be intercepted by the wall and would not hit the powder bed surface to cause gross cratering. The setup is illustrated in Figure 2.6.

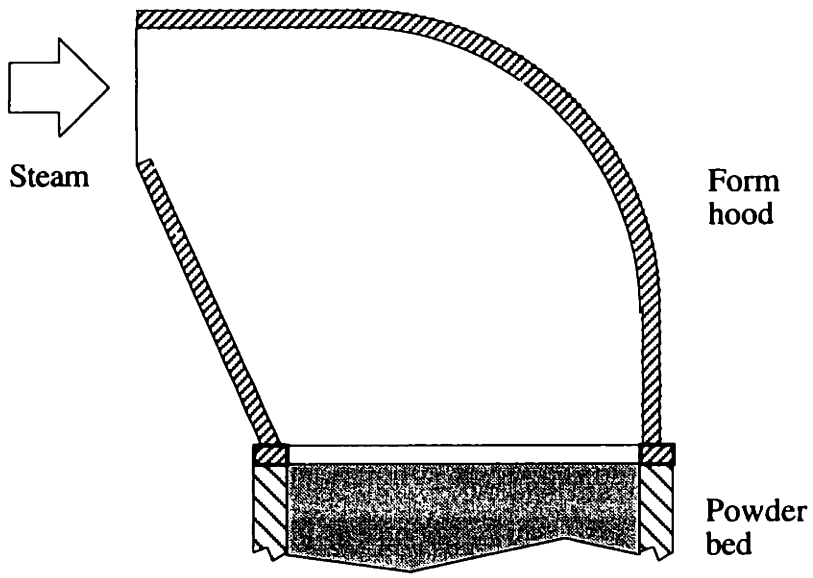

Figure 2.6 Introducing moisture into the powder bed.

The condensation of hot steam on powder particles makes steaming a very effective way of introducing moisture into powder beds. With the moisture added, the powder bed showed no sign of ejected particles during the printing. Slight settlement of the surface was noticed along the printed lines. These suggested that the moisture from the condensed steam increased the shear strength of the powder bed enough to withstand the impact pressure. Capillary forces of the binder did, however, caused the powder matrix to collapse.

Figure 2.7 is a SEM photograph of the surface of a part printed on steamed powder bed. Compared with Figure 2.5, it can be seen that the controlling of impact motion of

particles resulted in a much more regular texture of the surface: straighter lines and more uniform corrugation, as expected.

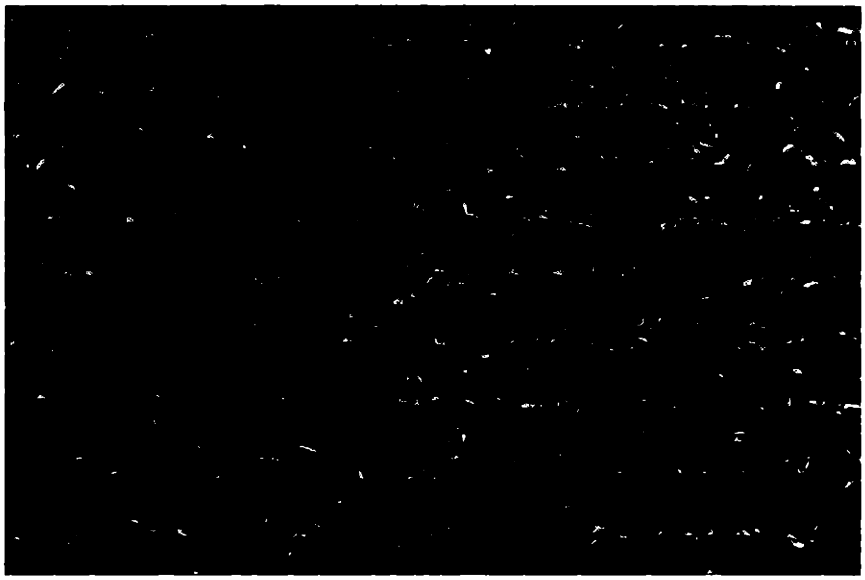

Figure 2.7 A surface printed on a steamed powder bed.

The surface roughness measured by the profilometer (DekTak II) confirmed these observations. The large variations of the peak-and-valley feature is subdued, and the Ra value (across the printed lines) was reduced to 11 μm. The remaining roughness is largely due to the corrugation. This was evident from Ra values measured along the printed lines, which was about 6.6 μm, much lower than that across the printed lines.

2.4.2 Printing on Fixated Powder Layers

The second method of increasing the powder bed cohesive strength was to lock the powder bed surface with an organic fixative. The purpose was to totally prevent the powder bed from deformation due to either binder droplet impacts or capillary forces, since the corrugation caused by the capillary forces contributed to the higher Ra values observed in the previous experiment. In this experiment, each new layer of powder was first moisturized using steam, and then an organic fixative was sprayed as an aerosol on the powder bed surface. The steaming step was to ensure that the powder bed would not be disturbed by the spray of the fixative, which contained some larger droplets. The organic binder was burned out in the firing step of post-processing, and thus was not present in the final part.

This steam-fixative procedure amounted to making a sheet of powder in situ before printing. The sheet was strong enough to withstand the impacts of binder droplets. Figure 2.8 is a photographic recording of the printing in action. The powder bed treated by the above procedures did not deform during and after the printing. In order to make the printing lines visible, phenolphthalein was ground into the alumina powder beforehand. Since the binder liquid was a base solution, which reacts with phenolphthalein, the printed line turned pink after the printing. The dark lines in the photograph are the binder traces developed by this method. The printing shown in Figure 2.8 was for the purpose of demonstrating the reaction of the powder bed to droplet impact, so the line spacing was widened to show individual lines. The photograph shows no signs of powder movement, either ejection or settlement, at the impact sites. Without the aid of the phenolphthalein, no distinctions could be made between the printed and unprinted areas.

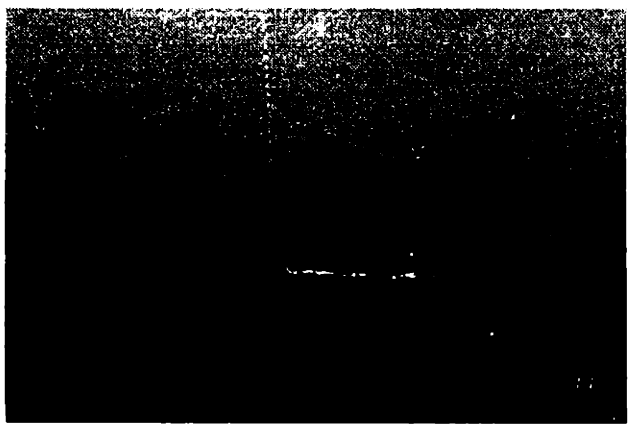

Figure 2.8 Printing on a fixated powder bed.

Figure 2.9 shows a cross-section taken across the printing direction. The surface corrugations, featured in Figures 2.5 and 2.7, are absent here. The overall profile is flat. On these surfaces, the geometry of powder particles and porous structures of the beds are the only factors affecting the surface roughness. The average Ra value of these surfaces was 6.6 μm. Further reduction of surface roughness requires using finer powder and increasing the packing density of the powder bed, so the pristine surface could be smoother.

Figure 2.9 also shows that there are no longer visually obvious demarcations between "primitive lines". In fact, primitive lines may not be the proper geometric concept to characterize these features of the fixated powder printing anymore. The formation of

primitive lines is the result of powder particles being pulled to the droplet under surface tension. In the current case, the particles are locked in place and incapable of moving or re-orienting. Only the binder liquid can percolate through the particle matrix.

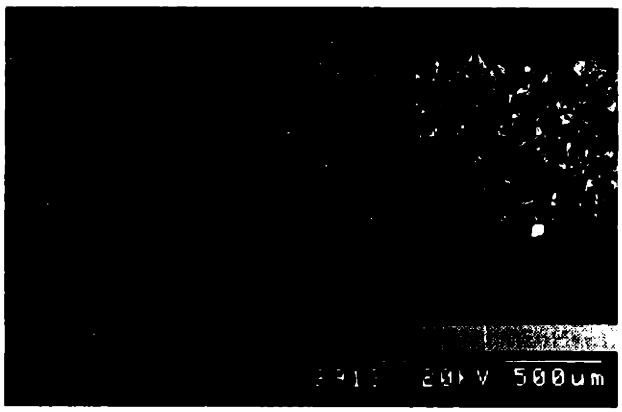

Figure 2.9 Cross section of a layer printed on fixated powder bed.
(Viewed along the printing direction)

The surface roughness resulting from different printing conditions are summarized in Table 2.1. The standard deviations associated with each condition may be interpreted in the light of the consistency of the surface texture, or the level of control over the powder particle movements exercised during the printing.

Table 2.1 Ra Values under Different Powder Bed Conditions

Powder Bed Conditions	Average Ra (μm)	Standard Deviation (μm)
Loose	> 15	
Steamed	11 (across the printed lines)	1.8
Steamed	6.6 (along the printed lines)	1.1
Fixated	6.6	0.59

2.5 Methods for Enhancing the Cohesive Strength of Powder Beds

Section 2.4 discussed different methods for restraining powder particle movements due to droplet impacts during printing. The results indicated that as far as the top surface's smoothness is concern, total fixation of the particles was most effective. However, applying organic fixative was not the only way to achieve this effect. In fact, the organic fixative has the side effect of making the surface slow in absorbing water. This tends to cause uneven width of the printed lines, which results in raggedness on the sides of the line.

If horizontal surface flatness is the only concern, a few other alternative methods can also fixate the powder particles. One method is to prepare the powder material by coating the particles with a thin layer of an inorganic salt of high water solubility. After spreading the powder in the powder bed, water can be introduced into the bed in the form of either hot steam or cold fine mist. The salt layers covering the particles will be dissolved first and then re-crystallize when the water evaporates, thus forming salt bridges at the contact points of the powder particles. Unlike organic fixative, inorganic salts will leave residual impurities in the printed part. If the final product is a metal part either by direct printing or by casting, the salt used for the coating should be carefully selected so that the impurities thus introduced would not have adverse effects on the properties of the metal part.

The cohesive strength of the alumina powder bed can also be increased by using sub-micrometer sized alumina powders. These powders exhibit strong cohesion between particles; powder beds created from them possess inherently high cohesive strength and can withstand droplet impacts without being aided by any after-spreading provisions. However, the incapability of these powders to flow makes the packing density of the powder bed less uniform. Meanwhile, since the particles have an inclination to adhere to the roller in clumps, the counter-rolling action of the leveling roller tends to rip particles off the powder bed in lumps and leaves pits in it. Special provisions need to be developed in order to be able to spread them into smooth and even layers. One way of making the surface of powder bed smooth is to replace the counter-rolling with press-rolling in spreading the powder with roller, as indicated in Figure 2.10. The intimate contacts between powder particles established by the press-rolling hold the particles together and prevent them from being pulled away from the powder bed by the roller as it rotates.

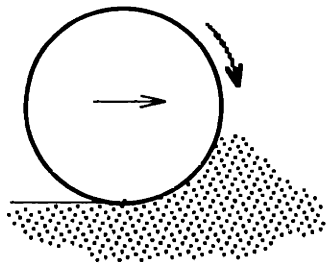

Figure 2.10 Leveling of the powder bed by press rolling

2.6 Other Droplet Impact Related Phenomena: the Illusive Types

Droplet impact interaction with powder is ubiquitous in Three Dimensional Printing. As discussed in the previous sections, the origin of the peculiar surface textures and bulk structures of 3DP parts can be traced to the droplet impacts on the powder bed. There are other manifestations of droplet - powder impact interactions which are more illusive, surprising, and seemingly inexplicable (that is, until an explanation is found). Occurring either frequently or rarely, their existence highlights the complicated nature of droplet - powder impact phenomena in Three - Dimensional Printing.

2.6.1 Low-angle, Long-distance Lopsided Ejection

One of such phenomena is often seen during printing on moisture-treated powder beds. Figure 2.11 illustrates the sequence of events. Moisture is first introduced to the powder bed either in the form of water steam or cold mist, with the intention of increasing the cohesive strength of the powder bed and reducing the powder ejection. After printing starts, nothing special happens during the first four or five passes of the raster scanning. As the binder is printed into the powder bed, the surface of the bed settles somewhat, and there are no signs of powder ejection. The whole powder bed surface appears to be neat and clean (Figure 2.11.a). Abruptly, the scene changes. In the area that has been isolated from the printhead path by the printed swath (Figure 2.11.b), the powder bed surface suddenly become looking like white moss is growing out of the powder bed. These turn out to be tiny clusters of powder particles crowding over the powder bed. In addition, this fuzzy area will now expand in the same direction and in step with the line-to-line movement of the printhead, and is always separated from the current printing line by a clear region.

The flurry of powder particle appearance on top of bed is apparently related to powder impact ejection. The questions are why it does not occur at the beginning of the printing but promptly turns up after a few lines are printed, why the ejected powder particles appear far away from the current printing line, and why this type of ejection is not observed in printing on loose powder bed.

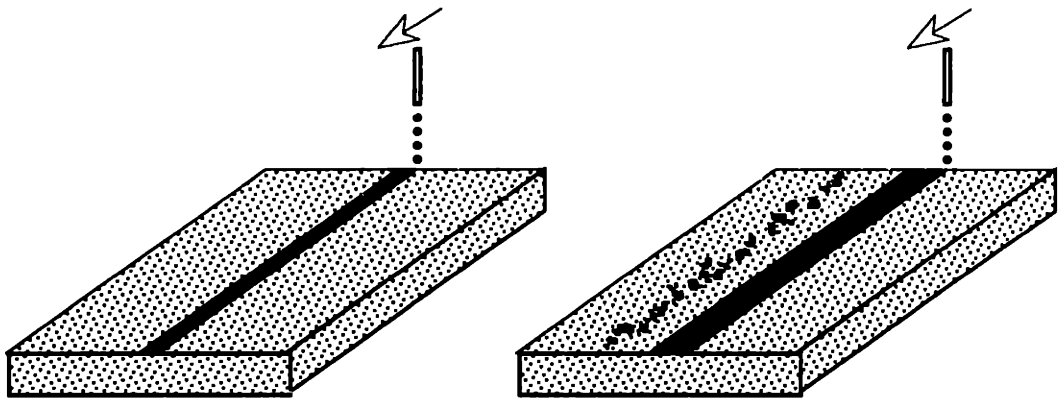

Figure 2.11 An Illusive type of powder ejection.

We need to examine the powder bed very closely in order to answer these questions. Figure 2.12 illustrates what happens to the moisture-treated powder bed while a new layer is being printed. The amount of absorbed moisture in the top layer of the powder bed is enough to prevent powder particles from being ejected when the first line is printed. This retaining powder is partially derived from the symmetric supports from adjacent powder particles on the sides. The deformation of the top layer, as explained before, is a slight settlement due to the capillary forces, as in Figure 2.12.a. The settlement creates more or less well defined edges at the boundary between the printed and unprinted regions. By the time a second line is printed, the binder droplet streams strike on the edge, which is constrained on one side and unsupported on the other. The droplet impact squeezes the powder and ejects some of the particles to the direction of least resistance. As a result, the angle of ejection is much smaller than that associated with the powder ejection when the impact site is surrounded by powder particles in all directions. At small angle of ejection and when the swath is only a few lines wide as illustrated in Figure 2.12.b, the ejected particles can be blocked by the ridge on the other side of printed swath. This causes the ejection not to manifest itself during printing of the first a few lines. However, as more and more lines are printed, the ejected particles will eventually clear the edge, as illustrated in Figure 2.12.c. These particles then fall back on the bed surface at the end of their

trajectories and become detectable. Sometime this amount of "white moss" is massive, which means the scale of ejection of this type can be substantial.

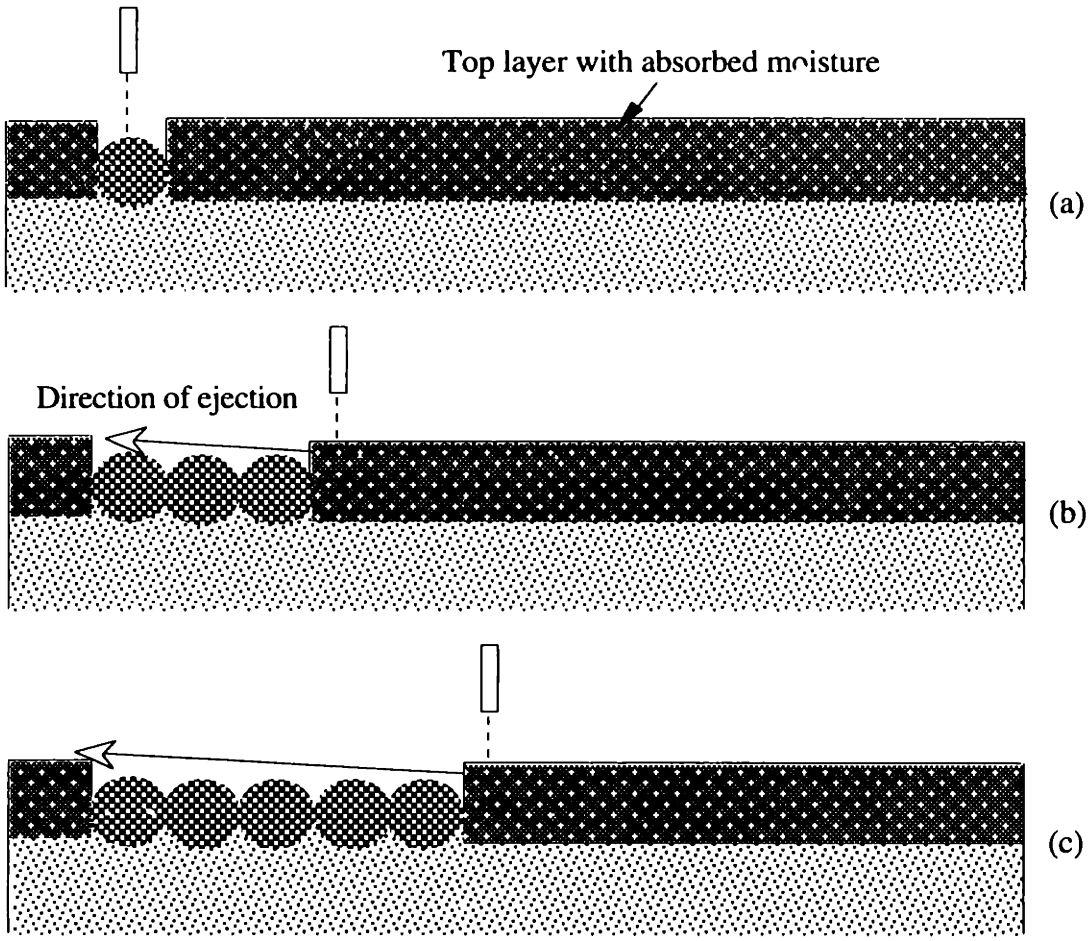

Figure 2.12 Powder ejection at lower angles. Printing is in the direction into the paper.

This interpretation of powder ejection at a low angle was verified with a simple setup. A thin ruler was placed near the path of the printhead in parallel with the direction of raster scanning. At first, when the printhead passed close to the ruler, no particle fallout was seen on top of it. As the printing continued, the path of the printhead moved further and further away from the ruler edge, and powder particles started to be seen on the ruler's top. In this experiment, the edge of the ruler functioned in the same way as the edge in the powder bed naturally formed during the printing.

The tendency for the powder particles to be ejected to the direction of least resistance was verified independently by printing single droplet of binder on a powder edge created using a mask of thin metal shim, as illustrated in Figure 2.13. After printing, a

notch was found at the printing site, and a spherical primitive ball was found lying some distance away from the edge. In this case, the total printed structure could not hold its place and rolled off the edge. Figure 2.14 shows a photograph (top view) taken after the printing of a single droplet onto the powder edge.

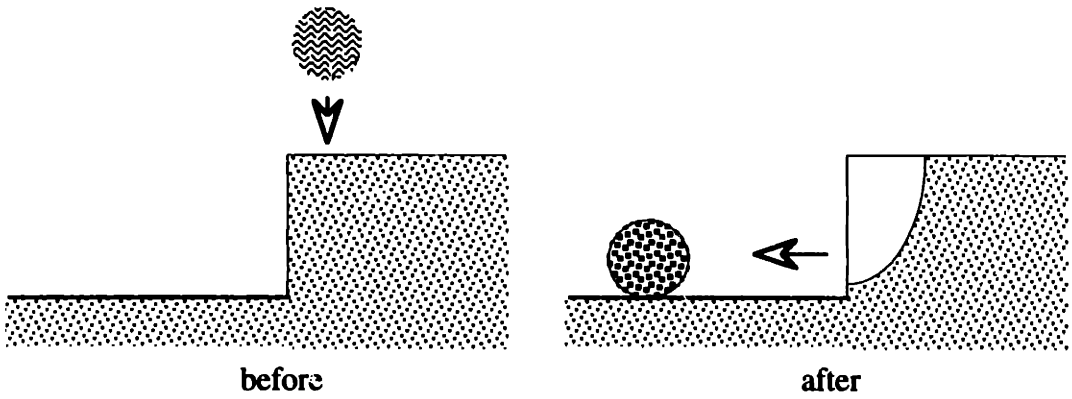

Figure 2.13 Printing a single droplet onto an edge in a powder bed.

Figure 2.14 Single droplets printed at the edge of a single layer (top view). The lower 1/3 of this photograph is the "plateau".

The angle and speed of particle ejection described in this section can be estimated based on the analysis above. In Figure 2.15, it is assumed that the air resistance can be neglected and the trajectory of the particles is parabolic. By knowing the height of the edge, h, and the distances L_1 and L_2, the following relationships can be used

$$\cos \zeta = [\, 1 + h^2(L_1^{-1} + L_2^{-1})^2]^{-1/2} \qquad (2.1)$$

$$U_j = \frac{L_1}{\cos\zeta}\left[\frac{g}{2(\cos^{-2}\zeta - 1)L_1 - h}\right] \qquad (2.2)$$

where (ref. Figure 2.15)

ζ = angle of ejection,

U_j = speed of ejection,

h = height of the edge,

L_1 = the distance at which the ejected particles start to go over the edge,

L_2 = the distance at which the ejected particles return to the powder bed,

g = acceleration of gravity.

With h ≈ 0.04 mm, L1 ≈ 0.7 mm, and L2 ≈ 8 mm, the powder particles are estimated to be ejected at an angle of 4° with a speed of 0.8 m/sec.

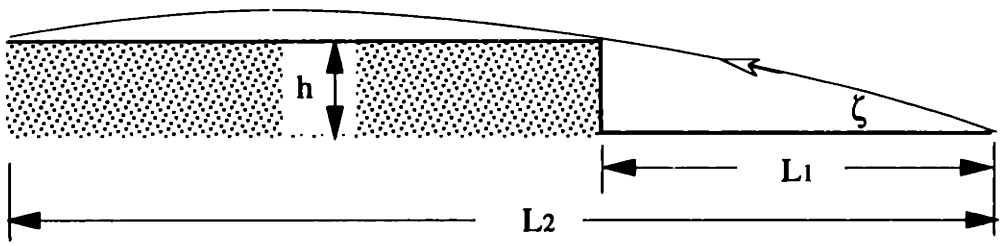

Figure 2.15 Estimation of the angle and speed of ejection during printing on a moisture enhanced powder bed.

The remaining question is why the lopsided long distance ejection is not normally seen during printing on untreated loose powder bed. This also has its answer in the local powder bed geometry. Recall that printing on loose powder bed leaves a sloped bank beside the printed line. Figure 2.16 shows that on a loose powder bed, new lines are printed on the slope where there is no edgy corner to be "cut off" by the binder stream as it happens, e.g. in Figure 2.12. In the case of Figure 2.16, powder particles would be pushed by the droplet impact to the right, not thrown out to the left. A subtle difference in the local topography changes the scene of particle ejection.

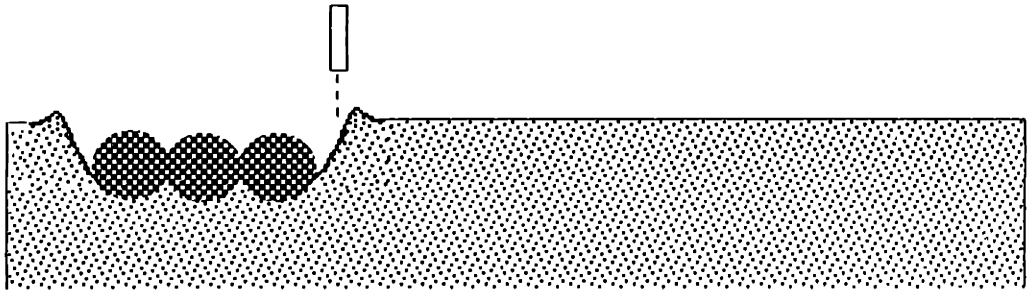

Figure 2.16 Why lopsided long distance particle ejection is not seen during printing on loose powder beds.

2.6.2 Balling, Line Pairing and Line Jumping

"Balling" refers to the phenomenon of a primitive line structure breaking into a string of bulky lumps due to surface tension during printing by raster scanning. This is commonly seen in printing on beds of loose fine spherical stainless steel particles (Figure 2.17). The direct cause of balling is insufficient mixing between the liquid binder and the powder particles. Poor wetting causes the fine stainless steel particles remaining at the drop surface instead of being engulfed by the droplet. Large size particles are heavier and less prone to this problem. This phenomenon is more prominent with particles smaller than 10 μm diameter. The liquid may remain inside of the particle coating for a long time before finally leaking out.

As the printhead passes, a liquid cylinder without enough solid particles in it is left on top of the powder bed. This liquid cylinder is thermodynamically unstable when its length exceeds its circumference, and would break up into separated beads just as a continuous liquid jet spontaneously breaking into droplets. Severe balling makes it impossible to print a consecutive integral structure, so it must be prevented from happening. The current method of preventing balling is to provide enough anchoring to the particles, so that they would not be pulled together by the liquid binder. Coating the particles with a salt and activating the salt with moisture after the powder layer (described in § 2.5) is spread is one way to achieve the particle anchoring.

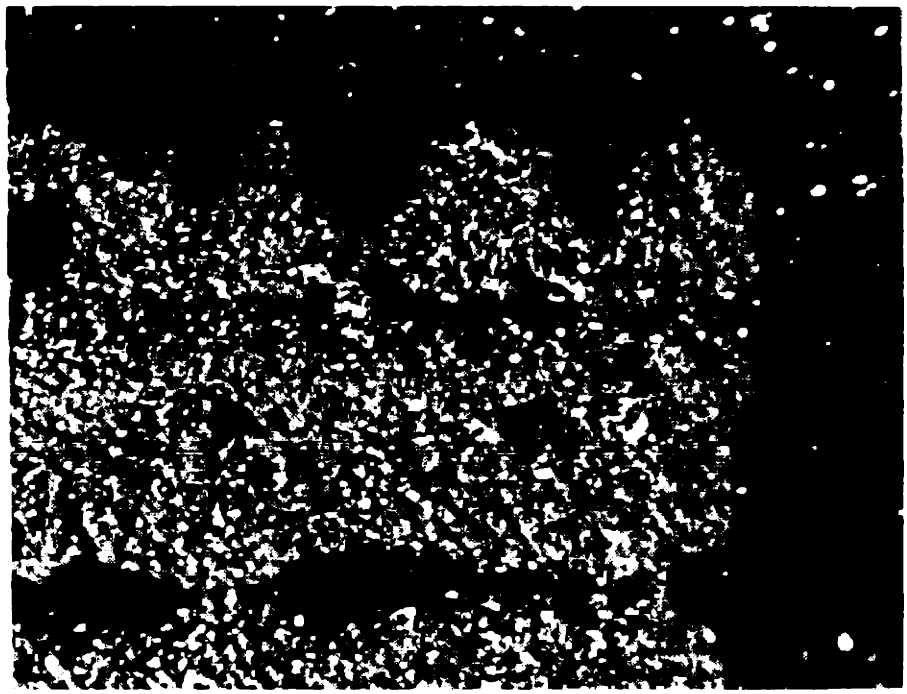

Figure 2.17 Balling (5 μm spherical stainless steel powder).

"Line pairing" refers to a faulty printing result where reduced line spacing is found in a period of every two printed lines, even though all the lines are printed at equal spacing. In Figure 2.18, there are sixteen lines grouped into eight such pairs. This is once again due to insufficient liquid - powder mixing up to the end of the impact stage. The mixture remains very diluted and able to flow. When a second line is printed beside the first one, the fluid second line moves towards the first line and to forms a pair with it. By the time the third line is printed, since the second line has shifted a little bit away from its supposed center position, the distance between the third line and the second is larger than the designed line spacing. Thus the third line does not touch on the second, and stays where it is supposed to be. This hypothesis about the surface tension origin of line pairing has been tested against other hypothesized origins (such as the binder stream being deflected to one side due to asymmetric air currents around the printhead) experimentally and proved to be the true cause by Alan Lauder. It should be noted that the prerequisite for the line pairing to occur is that even in later stage of line formation, the binder - powder mixture remains over saturated with liquid and fluent. It would be interesting to know under what conditions the mixture would contain enough powder particles and become immobilized.

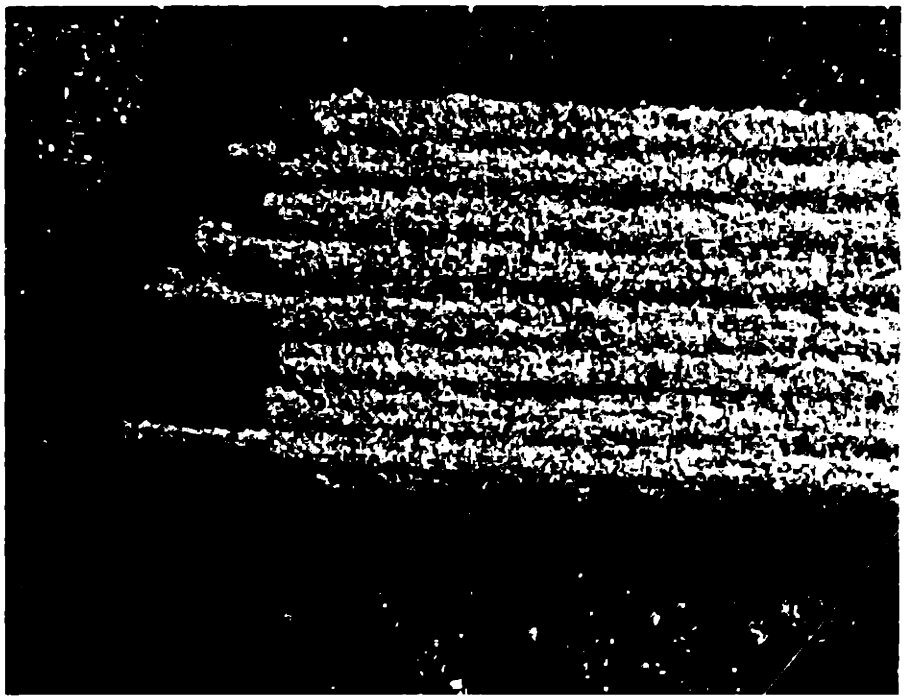

Figure 2.18 Line pairing (15 - 30 μm spherical stainless steel powder), sixteen lines formed eight well separated pairs.

"Line jumping" refers to the phenomenon that as a line is printed, it jumps right out of the powder bed. This is a very rare event and has happened only once through the six years history of Three - Dimensional Printing. As it happened, the printed line structures jumped out of a powder bed of 30 μm flaky alumina powder, which was pre-treated with cold water mist, and lay around like strings of spaghetti, as shown in Figure 2.19.

For such an event to transpire, the binding between particles within the printed line must be strong, so that the line structure would not disintegrate. Such a strong binding was not likely derived from the capillary force alone. The colloidal silica gel might be the main contributor to this strength. The powder in question contained citrus acid. Adding organic acids to alumina powders has been practiced since November 1990 for the purpose of promoting coagulation of the colloidal silica binder on its encounter with the powder so as to prevent the liquid binder from leaking out of the printed region in the powder bed [Fan, 1990]. The principle is that the acid lowers the pH value of the binder liquid and destabilizes the silica colloid, which is stable in a base solution and coagulates quickly at a pH value of 5 [Iler]. The line jumping incidence indicated that these strong bindings were developed in a time frame as the line was formed. The fast chemical reaction

might have been made possible by the moisture introduced into the powder bed before printing started, which should have dissolved the acid into a solution.

It is possible that the "edge cutting" effect discussed in § 2.6.1, which also occurs to powder bed pre-treated with moisture, played a role in this line jumping. The exact conditions of this occurrence were not investigated, and no attempt was made to duplicate this event. In any case, such an occurrence attests to the diversity and intricacy of impact phenomena in Three - Dimensional Printing.

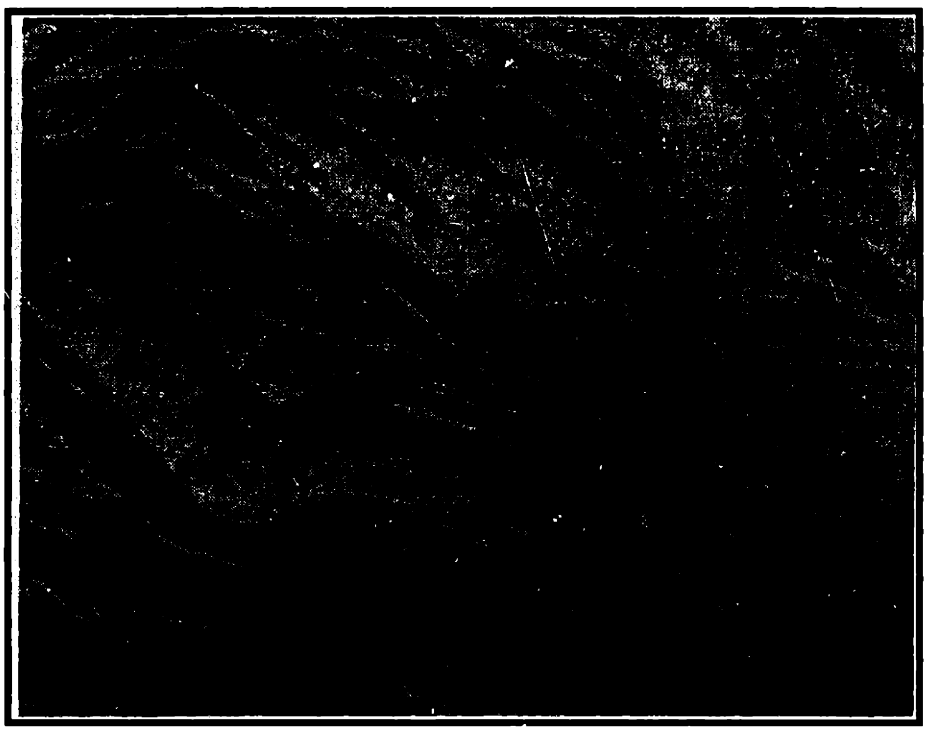

Figure 2.19 Printed lines jumped out of a powder bed and formed bundles. (30 μm flaky alumina powder. Powder bed was pre-treated with cold water mist.)

2.7 Droplet Parameters in Three Dimensional Printing

Throughout this chapter, the discussion on droplet - powder impact interaction has centered around the conditions and reactions of the powder bed. The output of droplet impacts is not only determined by the powder bed conditions. It is apparent that the droplet parameters, such as the impact velocity, the size of the droplet, and the rate at which the droplets are printed into the powder bed, also have important effects on the impact results. Using larger droplets and printing more droplets into an area will increase the sizes of the

primitive structure. Larger droplets, closely placed droplets, as well as higher impact velocity, will aggravate impact cratering, i.e. cause the printed structures to sink more deeply into the powder bed and more powder particles to be ejected. A functional relationship between the droplet parameters and the impact penetration of the powder bed will be developed later in Chapters 5 and 6. A brief summary of how the droplet parameters are related to the production considerations is given in the following.

The size and initial velocity of droplets are determined by two basic parameters, the flow rate of the liquid binder and the size and geometry of the nozzle. As described previously, the continuous liquid jet is broken into discrete droplets by imposed excitation, normally through a piezoelectric element. The maximum instability of the continuous jet is reached, according to [Rayleigh], at a frequency determined by

$$f = \frac{U}{4.508\ d}, \tag{2.3}$$

where

f = frequency of the external excitation,

U = jet velocity ,

d = diameter of the cylindrical section of the jet.

d, the diameter of the cylindrical section of the jet is not the diameter of the nozzle (assuming the nozzle has a circular opening), but is related to it. Jet issued from a circular nozzle may or may not have the same diameter as the nozzle, depending on the structure of the nozzle [Batchelor] as well as the liquid. For water issued from a long, slowly converging nozzle, the jet diameter equals to the nozzle diameter.

U, the jet velocity, is also the initial velocity of the droplets at the moment they break away from the continuous section of the jet. Then the droplet velocity gradually changes under the influence of the gravitational force and the air drag force, with the latter having a much stronger effect on the droplet velocity.

This "Rayleigh frequency" is an important reference point in selecting an excitation frequency for given U and d, and the relationship expressed by Equation 2.3 is used in the following discussion. The external excitation frequency, f, is also the number of droplets generated per second, so that

$$f = \frac{Q}{v}, \tag{2.4}$$

where

Q = the volume of flow per second,

v = the volume of each droplet.

U is a function of Q and d,

$$U = \frac{Q}{\frac{1}{4}\pi d^2} . \tag{2.5}$$

v is a function of d,

$$v = 4.508\ d * 0.25\ \pi d^2 = 1.127\ \pi d^3 . \tag{2.6}$$

Combining Equations 2.3 and 2.4, and multiplying the droplet volume by the liquid density, the momentum of the droplet is

$$m\ U = \rho v U = 4.51\ \rho\ Q\ d, \tag{2.7}$$

where

m = the mass of the droplet,

ρ = the density of the liquid.

By multiplying both sides of Equation 2.7 by U/2 and using Equation 2.5, the kinetic energy of the droplet is obtained as

$$\frac{1}{2}\ m\ U^2 = \frac{9.016}{\pi}\ \frac{\rho\ Q^2}{d} . \tag{2.8}$$

Among the independent variables, the density is a material property, determined by the composition of the binder. The diameter of nozzle, d, is selected based on practical considerations. Not only must the nozzle diameter be larger than any solid particles suspended in the binder liquid, for liquid binder such as colloidal silica, the tendency of the binder to coagulate and clog the nozzle has to be carefully evaluated in determining the size of the nozzle. Using a nozzle of larger diameter will greatly reduce the probability of nozzle clogging. The flow rate is a matter of production rate, depending on how large volume of

powder per second is desired to be bond by the liquid binder dispensed from a single nozzle.

In summary, the initial velocity of the droplet is determined by the flow rate and nozzle diameter. The volume of a droplet is determined by the nozzle size alone, given the condition that the nozzle is operated at the Rayleigh frequency. The momentum and kinetic energy of a droplet is determined by both the flow rate and nozzle size. The momentum is proportional to the product of the flow rate and the nozzle diameter, while the kinetic energy is proportional to the square of the flow rate and inversely proportional to the nozzle diameter.

2.8 Conclusion

Even though inkjet printing is considered as a non-impact printing technology in printing industry, this characterization can be misleading when the receiving media are beds of loose fine particles. Impact pressure and dragging forces of the liquid move the powder particles and alter the pore structure of the top layer of the bed. Surface tension renders the primitive features a curved surface. Deformation of the powder bed structure under liquid action is an essential part of this type of printing process.

Droplet-powder impact interactions play a critical role in the formation of primitive structures. The impacts deform the powder bed. These deformations, after being incorporated into the parts, are major sources of surface and bulk defects. Impact parameters, such as the impact speed, relative size and density of the droplet and powder particles, as well as the wetting properties of the two phases determines how fast and how well the liquid mixes with the particles in the impact stage. Thorough mixing of a droplet with powder particles during the impact stage tends to create finer primitive structures with better boundary definition. On the other hand, printing failures such as balling often occur in powder beds which are composed of particles of higher mobility (e.g. cohesionless spherical particles) and when the liquid-powder mixing is insufficient throughout the impact stage. Insufficient mixing can be due to that the liquid does not wet the solid phase well, or that the droplet has an impact speed which is too low to energetically stir up the powder particles.

Through changing the impact conditions from the impactor side (the droplets) and the receiving side (the powder bed), the outcome of the printing can be drastically changed.

Experiments have shown that the surface quality of parts built by Three Dimensional Printing can be favorably modified through various means of increasing the cohesive strength of the powder bed. On the other hand, printings under these modified conditions have also revealed complicated impact behavior. Finding and evaluating suitable printing conditions for refining the qualities of printing product is an on-going process. The success of the development of this technology depends on a better understanding of the impact process.

CHAPTER 3

HIGH SPEED PHOTOGRAPHIC OBSERVATION OF SINGLE DROPLET IMPACTS ON LOOSE POWDER BEDS

3.1 Introduction

Direct visual and photographic observations found that impact by streams of liquid droplets on a loose powder bed leads to the formation of primitive granular structures and grooves in the powder bed (Chapter 2). It is necessary to observe this process as it occurs in order to understand its development. This was made possible by taking high-speed photographs of a single droplet impact's on a powder bed. The observations help to assess the spatial and temporal scales of the impact dynamics.

The major difference between impact by a single droplet and impact by a stream of droplets released to the powder bed through raster scanning, as it is done in Three Dimensional Printing, is that in the case of the latter, successive droplets may overlap each other after they land on the powder bed. If a droplet has formed a powder particle aggregate by the time a following droplet arrives, the particle aggregate will be struck and may move further into the powder bed. The addition of momentum from the newly arrived droplet will cause the powder bed to deform more. It can be expected then that single droplet impacts will be less energetic in terms of powder ejection than multiple droplet impacts.

If the first droplet has not yet formed a particle aggregate by the time the second droplet arrives, the second droplet will simply add more liquid to the original liquid - powder mixture and make it more dilute. If this type of merging occurs to a succession of droplets released by the raster scanner, then the droplets may form a column of liquid lying on top of the powder bed. Such a liquid column is not stable, and will break up into liquid beads. So it is important to establish a time line of the impact events associated with a single droplet impact.

A high-speed photographic station was developed to observe a single fast moving (a few meters per second) and tiny droplet's (80 μm of diameter) impact on a powder bed. The rapid impact events (lasting from 0.1 to 1 millisecond) were recorded by single-frame open-shutter stroboscopic photography. Each frame of the photograph contained an image of the impact of a different droplet at a different location in the same powder bed after a certain time elapsed since the initial contact between the droplet and powder bed. The amount of time delay was increased from one frame to another uniformly. Impact velocities was measured for each droplet and the velocity variations were monitored carefully. The impact process was considered repeatable, i.e. the droplet size, impact velocity, and conditions at different locations of the powder bed were consistent throughout the photography. Thus, even though each photograph recorded an image of a different droplet at a different location, it also represented a repeatable process at a specific moment. The photographs were then assembled to represent a sequential event.

This chapter discusses the development of the observation equipment, experimental procedures and observed impact phenomena. It was found that a primitive ball appeared inside the crater while the crater was forming, i.e. the formation of the primitive ball and the formation of the crater started almost simultaneously. The evolution of the primitive ball finished first. The crater growth finished later. The duration of crater growth increased with the droplet's impact velocity.

3. 2 Station for Observing Droplet - Powder Impacts

This station facilitates the functions required for observing the fast process of a single droplet's impact using single-frame stroboscopic photography. This section describes the components of the apparatus, including the camera and its accessories, the lighting equipment, the printhead (the droplet generator and the droplet control electrodes) and the binder delivery and collection system, the electronic instruments for generating signals for exciting the stream and for charging and deflecting the droplet, the circuitry for measuring the droplet speed and timing the moment of photography, as well as the positioning structures for the printhead and the powder sample holders. The principle of the system operation is illustrated in Figure 3.1

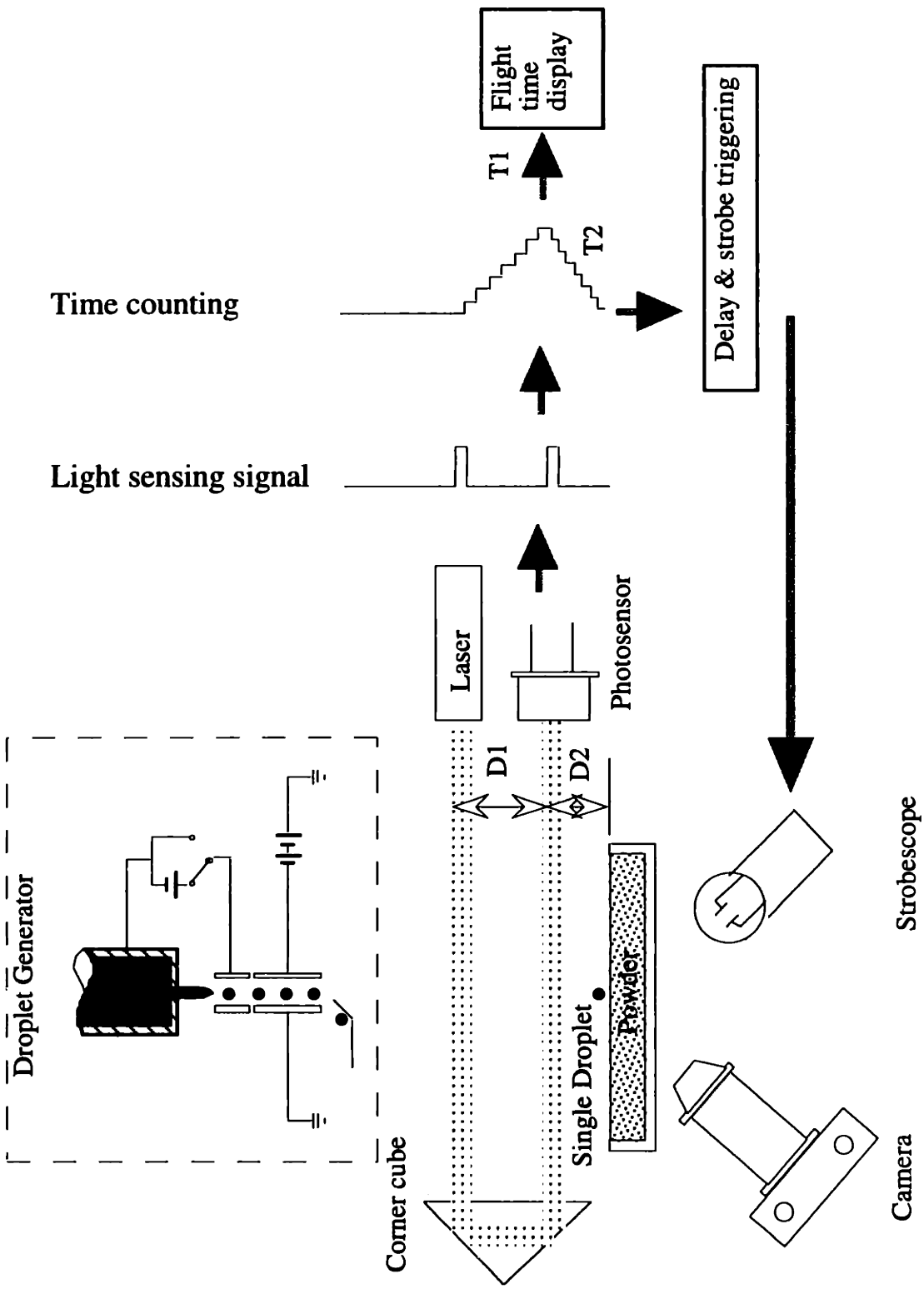

Figure 3.1 Principle of operation of impact photographic station

3.2.1 Printhead

Droplets used in the impact experiment were about 80 μm in diameter. A single droplet was generated by charging all the droplets issued from a continuous droplet generator, except a selected one. All the charged droplets were deflected by a constant electrostatic field towards one side of the path, and terminated at a droplet collector (catcher). The single selectively non-charged droplet moved along straight path until it struck the powder bed.

An Imaje continuous jet generator was used to produce the droplet stream (Imaje Ink Jet Printing Corp., Kennesaw, Georgia). The generator contained a rod piezoelectric element and a "P" type orifice plate fitted with a ruby nozzle of nominal size 40 μm diameter. A continuous liquid stream would break up into discrete, regular sized droplets under the influence of imposed oscillations originated from the piezoelectric element. Though the "P" type resonator was designed by Imaje to work with a 125 kHz excitation frequency, it worked satisfactorily at the reduced frequency of 62.5 kHz.

The entire structure of the printhead is shown in Figure 3.2. It consisted of, besides the droplet generator, the charging electrodes (for inducing electric charges on the droplets), the deflection electrodes (for separating the charged droplets from the uncharged), a catcher (for collecting the deflected droplets), and LED strobe lights (for inspecting the stream.) The gap where the electrostatic actions took place was between two opposing acrylic blocks, each fitted with one piece of charging electrode and one piece of deflection electrode.

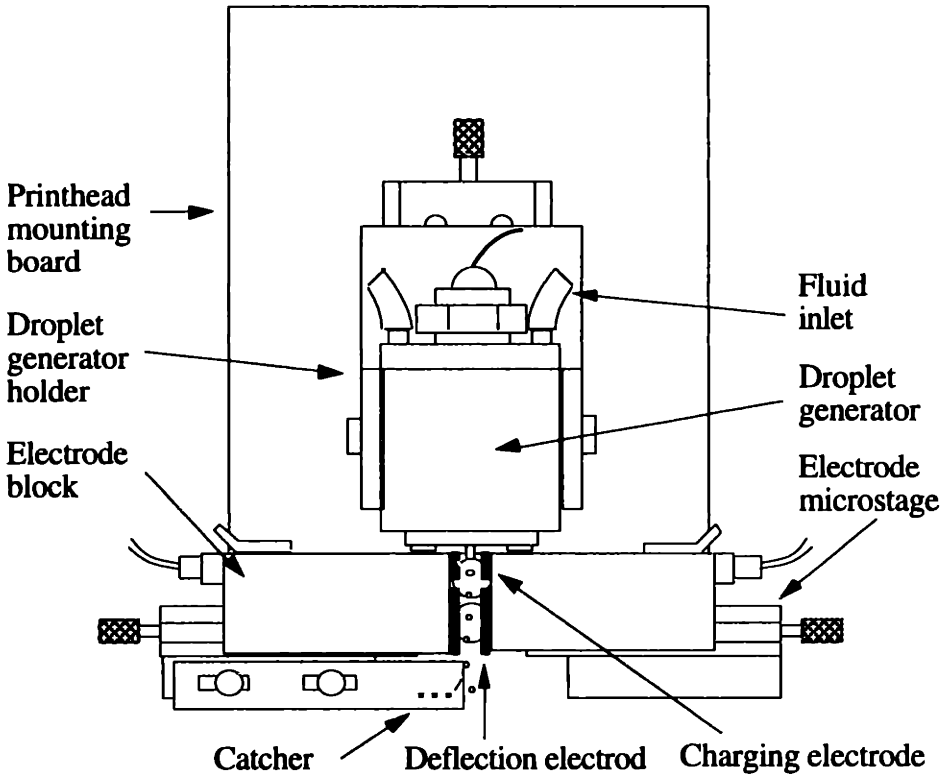

Figure 3.2 Printhead

The droplet generator and the two electrode blocks were mounted individually on the printhead base board via three micro-positioner stages (by the Edmund Scientific Company). The mounting arrangement allowed easy and quick adjustment of the vertical position of the droplet generator (thus the position of the stream break-off point relative to the charging electrodes) and the width of the charge-deflection gap. These mechanical adjustments extended the delicacy of droplet stream adjustments beyond that available through electrical means, such as changing the levels of the charging voltage, the magnitude of the excitation signal and the deflection voltage.

The whole printhead assembly was attached to a positioning stage capable of moving in the z direction. So the height of the printhead relative to the power bed could be adjusted. The maximum extent of travel along the z direction is 12 cm.

The binder liquid was delivered from a stainless steel reservoir (pressurized by compressed helium gas) to the printhead through a Calyx filter capsule (polypropylene, 1.2

μm) and an in-line stainless steel filter. The liquid collected by the catcher was drawn away by a MasterFlex® peristaltic pump.

3.2.2 Printhead Control Circuitry

A signal generator ("DoItAll 2") was built to drive the printhead. The unit generated a 62.5 kHz sinusoidal electric signal to excite the jet. A wave form of 1 μs pulse width was generated at the same frequency (62.5 kHz) to drive the LED strobe for back-lighting of the droplet stream. This circuit also produced a DC voltage, adjustable from zero volts up to +90 volts. This voltage was connected to the charging electrode on the printhead, and induced negative electric charges on the droplets. These charged droplets would be deflected, under the influence of a constant electric field of 1.4×10^6 V/m, between the two deflection electrodes, toward the catcher, which terminated the droplet stream. Interrupting the charging voltage would produce non-charged droplets. This was done by pushing the "fire" button on the instrument., which caused the charging voltage to swing from the pre-set high DC level down to ground for a period of 16 μs. A droplet breaking off from the continuous section of the printing stream during this period would not acquire the negative charges as the other droplets did, so would not be directed by the deflection electric field towards the catcher. This droplet would follow a straight path and end by striking the powder bed. The DC voltage swing was synchronized to the jet excitation signal and the breaking off of the droplets. The phase angle between the two signals could be shifted from zero up to one cycle in sixteen discrete steps (set by four toggle switches on the front panel.) This provision was to compensate for possible phase differences between the driving signal and the actual breaking off of the droplet, so that partial charging of droplets could be avoided.

3.2.3 Measuring Droplet Speed and Triggering the Strobe

The droplet impact speed is a major parameter considered in the impact study. An opto-electronic metering device (SpeedTrap) was developed to measure the impact velocity. The signal for triggering the 1538A Strobotac®(discussed in the next section) was also output by this device. Its principle is described in this section.

Two parallel laser beams, intercepting the droplet path perpendicularly, form a speed trap. The upper beam was emitted from a laser diode of 670 nm wavelength with a cross-section 4 mm by .6 mm, the lower beam was its reflection through a trihedral prism. A photosensor-preamplifier assembly was at the terminal end of the lower laser beam. The photosensor worked in photovoltaic mode. Constant light irradiation produced a DC signal at the output of the amplifier.

When a droplet runs through a laser beam, the reduction of radiance caused a pulse at the output of the amplifier. In the parallel arrangement of the two laser beams, a passing droplet produced two pulses, separated by the time the droplet took to cover the distance between the two laser beams. The velocity of the droplet, U, equals the distance between the two laser beams, D_1 , divided by this time, T_1, (refer to Figure 3.1),

$$U = \frac{D_1}{T_1} \tag{3.1}$$

The pulse generated at the moment the droplet passed the lower laser beam was used to trigger the strobe light. But before doing so, the signal was delayed twice. The first delay was to allow the photograph to be taken only after the droplet reached the powder bed. The second delay was to postpone the photography by a pre-set amount of time after the droplet reached the powder bed. The second delay was done through a performed by a 1 MHz time counter circuit and manually set by rotary BCD switches, in increment of 1 μs.

The first delay needs to be explained further. This delay was necessary because the lower laser beam was a few millimeters above the powder bed level, so it took additional time for a droplet to reach the powder bed after it crossed the lower bean . Since this extra time depends on the droplet velocity, variations of droplet velocity made it difficult to compensate for this time period. Droplet velocity varied for two reasons. Large changes in the velocity were intentionally imposed so that its effects on the impact outcome could be studied. Meanwhile, unintentional small random variations of velocity occurred due to the air resistance on a fast moving droplet as well as other secondary reasons.

Automatically setting the delay time with compensation for the droplet velocity

variation was done by an up-and-down time counter. This counter both tallied the traveling time for the droplet to cover the distance between the two laser beams and kept track of the time needed for the droplet to reach the powder bed after it passed the second laser beam. To accomplish these two tasks, a logic circuit selected one of two clock signals to feed to a counter. At the arrival of the first laser-beam-breaking signal, the counter started counting up at the fixed frequency of 1 MHz and stopped when the droplet ran across the second laser beam. The time tallied was then latched and displayed in units of microseconds by a four-digit LED display. Then, the counter automatically switched operation mode, and started to count down from the number just tallied, at a rate determined by the second clock signal frequency. The important point is that by the time the droplet reached the powder bed surface, the counter should just count to zero.

The count-down clock frequency was generated by a voltage-to-frequency converter with the frequency set by the following relation. T_2 , the time for the droplet goes through the distance D_2 , is

$$T_2 = \frac{D_2}{U} = \frac{D_2}{D_1/T_1} = \frac{D_2}{D_1} T_1 \qquad (3.2)$$

So if the count-down frequency, f_{down} , is set to

$$f_{down} = \frac{D_1}{D_2} f_{up} , \qquad (3.3)$$

where f_{up} is the clock frequencies for counting up (1 MHz), the counter will reach zero by the time the droplet strikes powder bed surface.

By the time the droplet reached powder bed, the multiplexer IC chip stopped the up-down counter and started the second absolute time delay counter. At the end of the second delay time, a TTL signal was generated to trigger the 1538A Strobotac® for taking the photograph.

3.2.4 Camera Set-up

The camera used was an SLR Olympus OM-4T, equipped with a 20 mm Suiko Auto-Macro micro-lens, and a telescopic auto extension tube 65 - 116 mm long. With the tube fully extended, this combination achieved a magnification of nine times. The object distance was 20 mm.

Besides taking photographs of the impact events, the camera was also used for (1) Inspecting the stream conditions such as the position where the continuous jet stream breaks up into droplets, steadiness, straightness, (2) Calibrating the distance between laser beams, D_1, which was a parameter used for calculating the droplet speed, and (3) Verifying the singularity of the droplet throughout the experiment. These functions were secondary but equally important to the success of the experiment. For these purposes, another 38 mm micro-lens of the same made proved more convenient to use due to its longer focal length and larger view field. With the extension tube fully extended, the magnification with this 38 mm lens was four times.

The OM-4T was fitted with a detachable NPC/Polaroid camera back, which could be used with a few models of Polaroid instant films. Before taking photographs with a whole roll of 135 mm films, the regular camera back would be replaced with the Polaroid back and instant films (of a speed similar to the 135 mm film), and test shots were taken to check for the proper film exposure, and the camera setting and lighting could be adjusted accordingly. This procedure helped greatly to ensure the success of the 135 mm film shooting. Two kinds of black-and-white films were used most frequently, the Kodak Tmax P3200 (35 mm) and Polaroid 667 (3000/36°).

The camera was mounted on the stand of a used microscope with the microscope lens tube removed. The microscope stand was clamped to a heavy steel base on which the supporting structures for the printhead and powder bed were mounted. Since loading the Polaroid film incurred substantial force on the camera body, the rigid fixation helped avoid disturbances to the camera's position. The height-adjustable platform of the microscope stand made it convenient to move the camera up and down and fulfill the camera's multiple functions as described earlier. The horizontal hinge of the stand allowed the camera to be quickly swung out of the way and later recovered to its original position.

With this provision the printhead and other essential devices in front of the camera became easily accessible. These conveniences are indispensable in an experiment where frequent manipulations of the powder bed and attendance to the printhead are necessary and all of these operations need to be carried out in a tight space jammed with various devices.

For taking the picture, the camera shutter was set at the B setting and was opened before a single droplet was released. A frame of film was exposed when a droplet reached the powder bed and triggered the strobe light. The triggering mechanism was described in Section 3.2.3. The camera together with the whole photographic station was enclosed in an used IBM line printer enclosure, lined with photographic wrapping paper . With the cover down, the station area became a small dark room, so that the open-shutter stroboscopic photography could be carried out in a lighted room without interrupting other activities in the lab.

A single droplet impact on loose powder produces a steep crater. Most part of the impact process is not visible from the side; top view is the best angle for observing the impact events. A first surface mirror oriented at a 45° angle over the powder bed made it possible to take top-view pictures (Figure 3.3). A 0.4 mm wide slot was cut through half of the mirror width. The droplet passed through this slot to reach the powder bed.

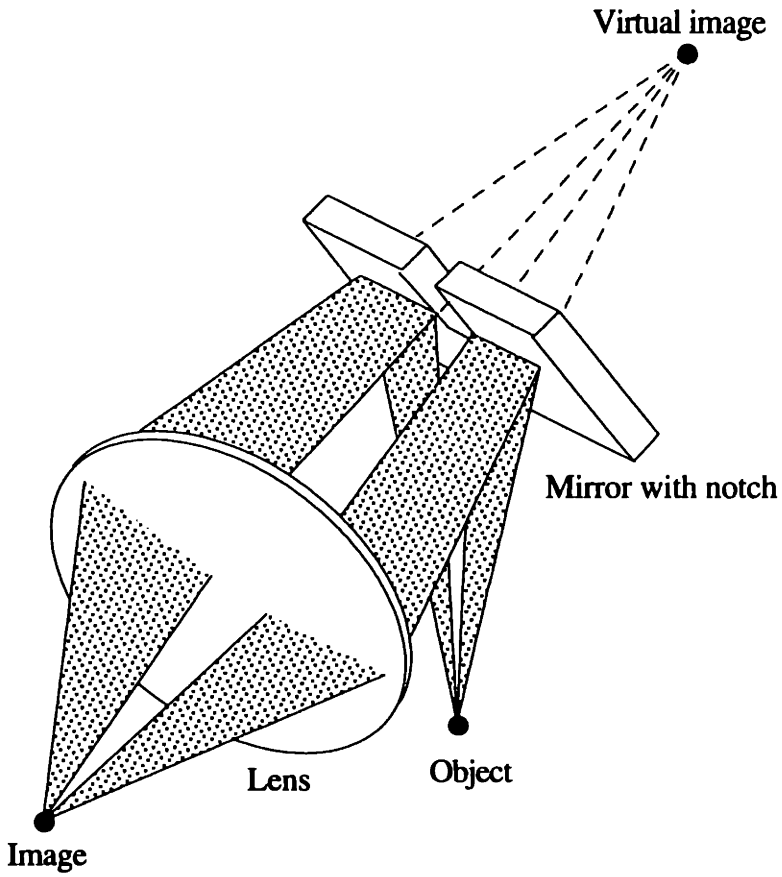

Figure 3.3 Taking top-view photographs through a 45° first surface mirror

This arrangement entailed a few restrictions (Fig. 3.4). Since the camera was aimed at the powder bed via the mirror, the camera needed to be moved forward to keep the object in focus. As mentioned before, the front of the 20 mm micro-lens needs to be 20 mm away from the object. This distance had to be maintained along the new light path when the object was viewed through the mirror. This brought the lens very close to the mirror. In order to keep the lens from touching the mirror and powder bed, the first surface mirror needed to be placed as close to the powder bed as possible. The place closest to the powder bed and still large enough to accommodate the mirror was the space in between the two laser beams. Around the powder bed being photographed, every small space had to be fully utilized in order to take the top view picture at a high magnification. The mirror was mounted on a microstage, so that it could be moved out of the way of the liquid jet when the jet was started or shut down. The jet was likely to have large lateral movements at these

times; leaving the mirror in its working position during these occurrences would have the first surface mirror contaminated and damaged by stray corrosive liquid.

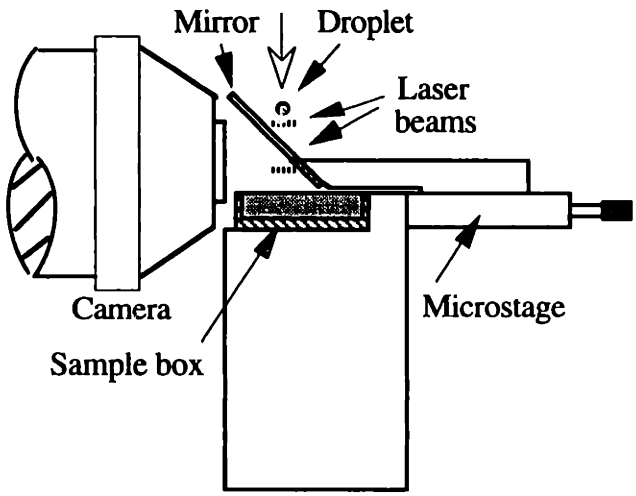

Figure 3.4 Spatial constrains within the working volume.

3.2.5 Lighting

When being photographed, the powder bed was encircled by various devices: a camera in the front, a printhead and a mirror on the top, a laser and a trihedral prisms on the two lateral sides, and the carriage of the mirror (at 45° to the powder surface and to the camera view line) at the back. This left a small space at the side of the camera lens to place the light source (Figures 3.4 and 3.5).

A General Radio 1538A Strobotac® was used with a 1538-P2 extension lamp to illuminate the object being photographed. The bulky reflector was taken off the extension lamp so that the lamp could be accommodated in the restricted space around the powder bed being photographed. A bulb was vacuum-evaporation-coated with a layer of aluminum, making the bulb wall a reflector to enhance the light intensity. The unit has a 0.7 μs flash duration, short enough to 'freeze' the image of a droplet moving at 10 meter per second. During the flash, the displacement of the droplet was 7 μm, about 8% of the size of a 85-μm diameter droplet.

The strobe was externally triggered to produce a single flash when a droplet reached its pre-specified photo position. The triggering signal was from the time delay circuitry described earlier.

3.2.6 The Powder Sample Carrier

The power sample box was placed on a platform, on which were also attached the laser, the electro-optical sensor circuit, the trihedral prisms, and the first surface mirror. The platform was attached to a positioning stage, so that the mirror's gap could be aligned with the path of the droplet (Fig. 3.5).

During the experiment, the powder sample was moved stepwise laterally to change the impact site after each frame of photograph was taken. This was done manually with a micrometer head, as shown in Figure 3.3.

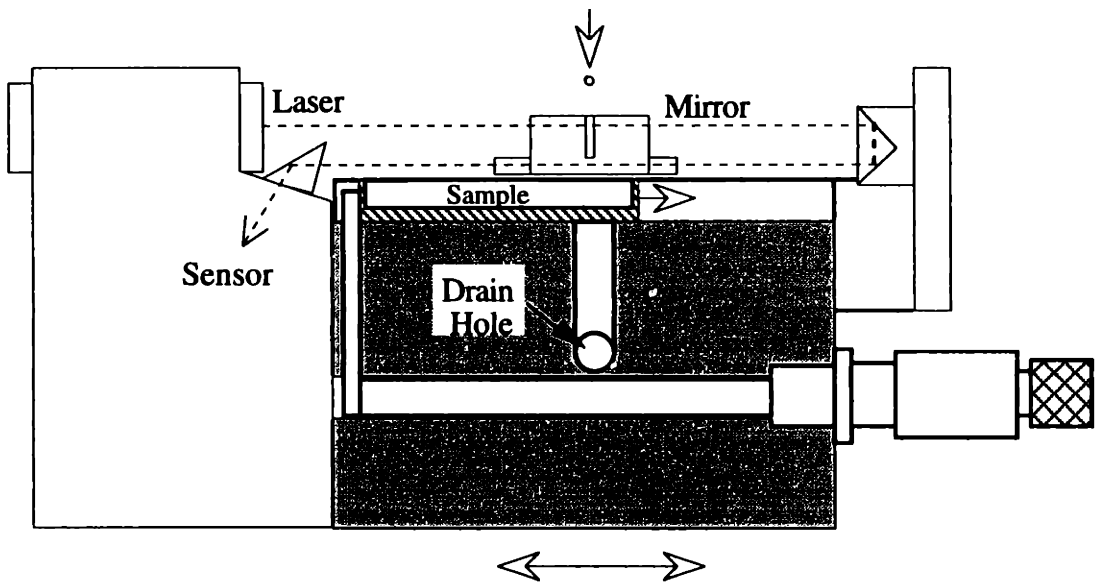

Figure 3.5 Powder sample platform.

3.3 Materials and Experimental Procedures

3.3.1 Powers and Powder Sample Preparation

The powders used in the experiments are listed in Table 3.1. The size distribution of these powders are given in Appendix I. The two alumina powders flow relatively well, so the sample top surface can be roller-leveled after the powder has been deposited in the sample box.

Table 3.1

Powder	Shape	Size	Manufacturer
Electronic grade alumina	Flakes	25 μm	Norton, MA
Alunabeads®	Sphere	10 μm	ICD

Powder samples were contained in boxes made of aluminum. The depth of the powder space was twenty times larger than the crater depth. This ensured the experimental results free of any potential boundary effects. For the same reason, the impact sites were always selected far away from the side walls of the powder sample box.

Samples of these two powders were prepared with the same procedure. The goal of the procedure was to promote powder mixing in order to improve the packing uniformity. The sample box was deposited with powder of an amount 25% in excess to the box's volume, and then covered with another box. The two boxes were held together and shaken and turned for a fixed number of times. The sample was then moved onto the leveling platform and the cover box was removed. The platform consisted of two parallel guides and a lowered section between the guides, with a depth the same as the thickness of the box. The box was placed in this section. A 3/4" roller was counter rolled over the box against the guides to create a evenly leveled powder sample surface. The set-up is shown in Figure 3.6.

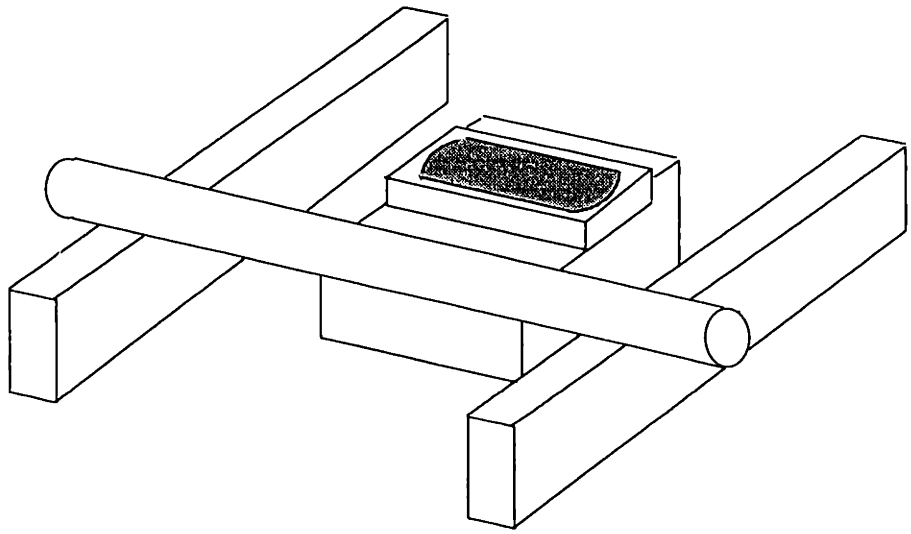

Figure 3.6 Sample leveling.

3.3.2 Measuring the Apparent Density of Powder Sample

The sample boxes were also used as measuring devices to obtain the volume of the powder in each sample. The mass of the sample was obtained by weighting the whole sample and then subtracting the mass of the box from the total mass. The powder space in the box was made as large as possible to increase the accuracy of density measurement.

The planar dimensions of the sample boxes were measured with a toolmaker's microscope. The depth of the powder space of each box was measured with a depth micrometer. Each of the boxes was weighted with a balance of precision equal to 1 milligram.

3.3.3 Flow Condition Quantification

The liquid used throughout the tests was distilled water. The electrical conductivity of the water was adjusted by adding sodium chloride. The density of the solution was measured with a hydrometer. The room temperature and humidity were recorded.

The flow rate was measured by accumulating flow for four minutes and then weighing the collection. The volume flow rate was obtained by dividing the mass of flow by the density of the solution. The droplet size was obtained by dividing the volume of flow per second by the jet excitation frequency (62.5 kHz.) The typical droplet diameter was between 80 μm to 90 μm.

The flow rate was measured before, during and after each experiment to check on variations. Because the droplet speed was measured with the SpeedTrap for each individual droplet, the purpose of flow rate checking was solely to assess the droplet size. The flow rate variation was small. Translated into droplet size variation, the change was less than 0.3 %, corresponding to diameter variation of 0.24 μm for a droplet of 84 μm diameter.

3.3.4 Adjustment of Stream Angle and Beam-Bed Delay Time

Before starting the impact tests, the angle of the stream was checked in the x-z plane and y-z plane by moving the camera between the highest and the lowest levels while looking at the stream through the view finder of the camera. A vertical stream would always be at the same lateral position in the view finder and always in focus.

The singleness of the droplet and the strobe delay time were inspected and fine tuned with the aid of the camera. First the count-down frequency of the delay circuit, to compensate for the droplet's velocity, was adjusted according to the ratio of the distance between the two laser beams and the distance from the lower laser beam to the powder bed. This would bring the droplet into the view-field of the camera. Then a fine adjustment of the count-down frequency followed so that the droplet nadir would start to touch the powder bed when the strobe light was triggered. The fine adjustment was aided by placing a U-shaped calibration block with a cross hair on the powder bed platform in place of the actual powder bed (Figure 3.7). The top edge of the cross hair was designed to be at the same height as the powder bed top surface would be. Then a single droplet was repeatedly released by pushing the firing button. When the strobe light was triggered by the droplet, the droplet became visible around the position of the cross hair on the calibration block. The count-down frequency, $\frac{d_{bs}}{d_{bp}} f_{up}$, was slightly increased or decreased until the droplet

nadir was seen at the same level as the top edge of the cross hair. This completed the fine tuning of the count-down frequency.

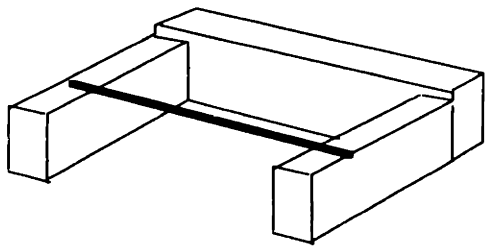

Figure 3.7 The calibration block for finding the proper delay time for triggering the strobe light at the moment a droplet starts to touch the powder bed.

3.3.5 Impact Test

The impact photography was done using the 20 mm micro-lens to obtain higher magnification. As was described in the chapter on experimental apparatus, the top-view allows looking into the crater, so the whole cratering process can be observed. As discussed before, this was made possible by introducing a first surface mirror placed at 45° angle on the optical axis of the camera over the powder bed. The droplet was allowed to pass through a narrow gap cut into the mirror. Because of the gap, the aperture of the lens needed to be increased to f4, otherwise the central area being photographed would appear as a dark stripe on the film. The enlargement of aperture reduced the depth of view.

To assemble single frame photographs to represent a sequence of impact events, it is important to assure that each droplet photographed has the same initial impact velocity. A photographic session normally lasted a few hours long. Flow rate drift over the period was the main cause of droplet velocity variation over each session. In the impact tests carried out in this investigation, the speed of each droplet was measured individually, so the droplet velocity was monitored very closely. Whenever a change of droplet velocity was detected, the source causing the change was corrected.

3.4 Results of High-Speed Photographic Observation of Droplet Impacts

3.4.1 Droplet Impact at Higher Initial Velocity

Figure 3.8 shows a sequence of 36 impact photographs of droplet impact on a loose powder bed, at an impact speed of 11.71 m/sec., with a standard deviation of 0.06 m/sec. The powder used in taking these photographs was the electronic grade alumina flakes, nominal size 25 μm, from Norton. The packing density was 33.6%. The diameter of the drop was 87.6 μm (flow rate 1.32 ml/min., excitation frequency 62.5 kHz). Each image represents the impact process at a time 25 μs after the previous image. In taking the photographs of this sequence, the water was clear, and a clear droplet seen with frontal lighting and a white background did not show up well. So in taking the photographs shown in the next section, the water was dyed to increase its visibility.

These photographs show that the diameter of the crater opening grew with time, and kept increasing up to 900 μs after the impact started. After 900 μs no obvious change to the crater diameter is discernible from the photographs.

At the center of the crater, a powder particle aggregate gradually appeared. Its image in the photographs goes through a transition, changing from a blob without distinctive surface features to a powder aggregate with clear granular texture. The image of the powder particle aggregate finalized at about 175 μs after the impact started.

Photographs were also taken every 2 μs for the first 60 μs after the impact started. Six photographs, from 46 μs to 54 μs, are shown in Figure 3.9. At such small time increments, the development of the crater and the powder aggregate is still discernible, but much more subtle. On the original photographic prints it can be seen that the powder aggregate started taking shape during this period.

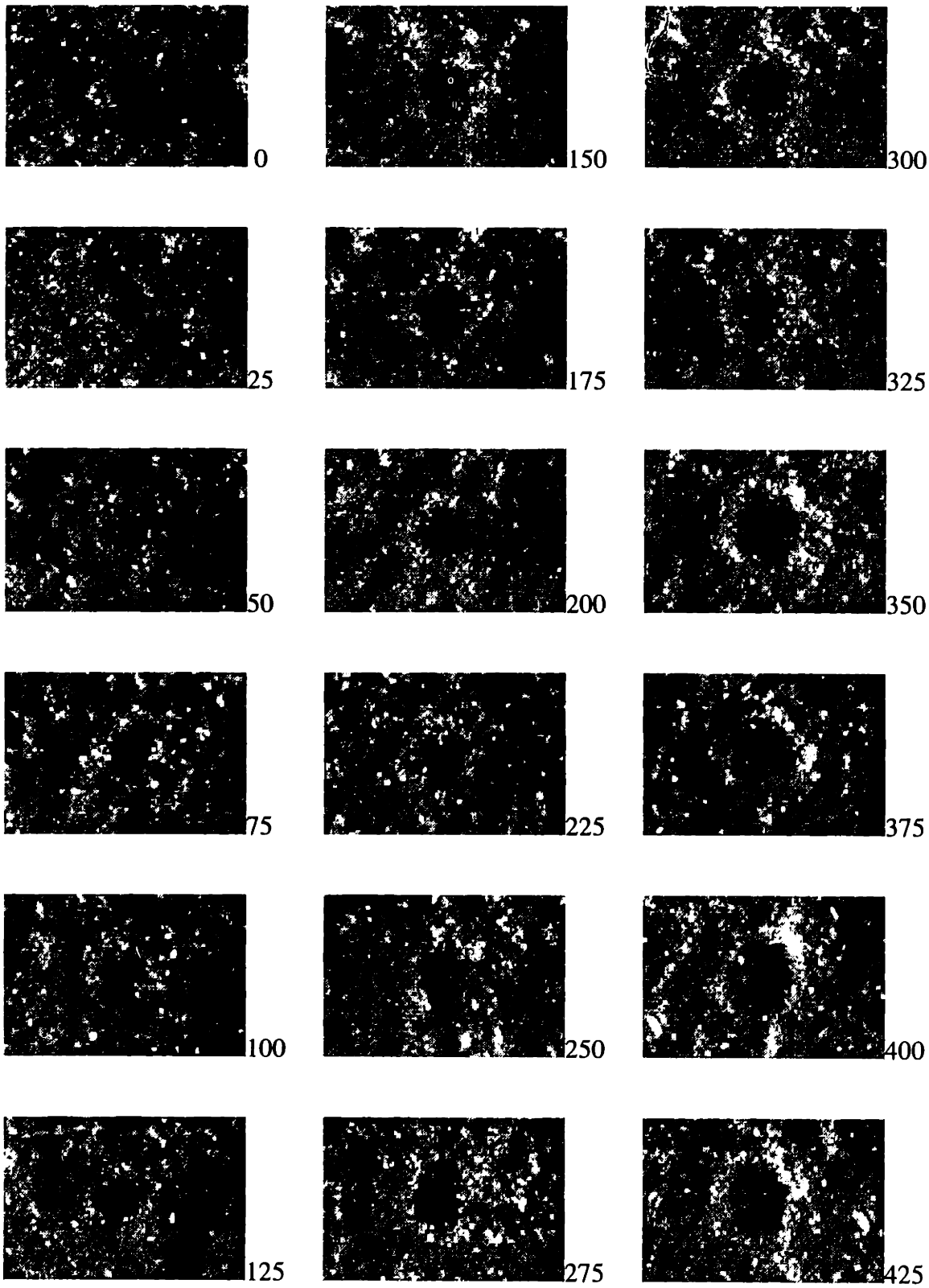

Figure 3.8.1 Impact cratering process on 25 μm flaky Al_2O_3 powder bed.
(unit: μs)

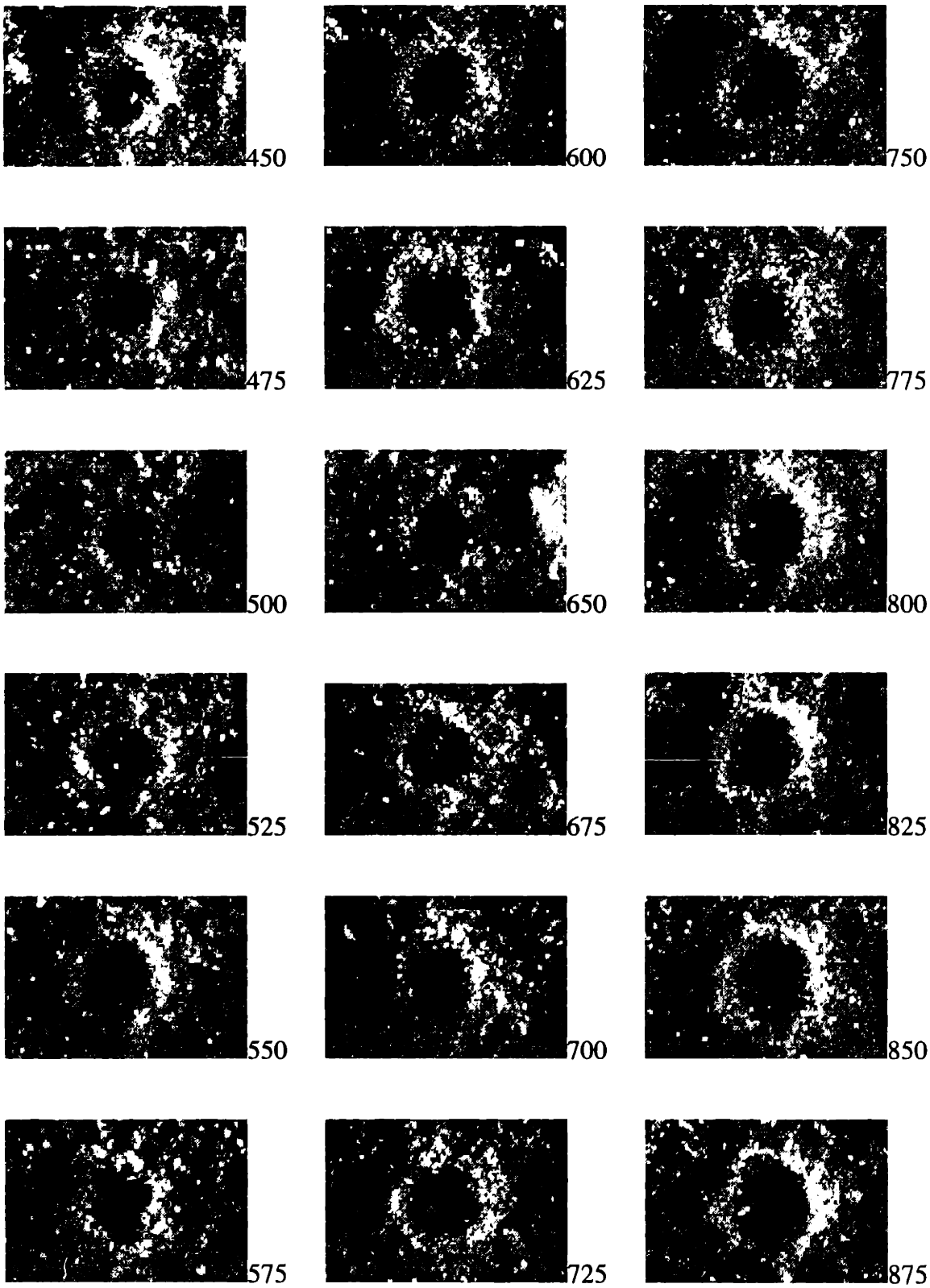

Figure 3.8.2 Impact cratering process on 25 μm flaky Al_2O_3 powder bed.
(unit: μs)

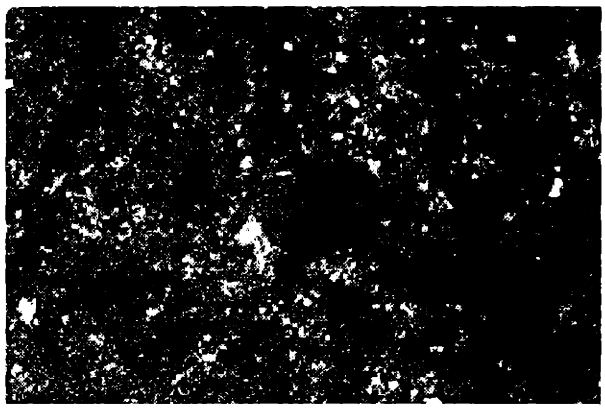

t = 44 μs

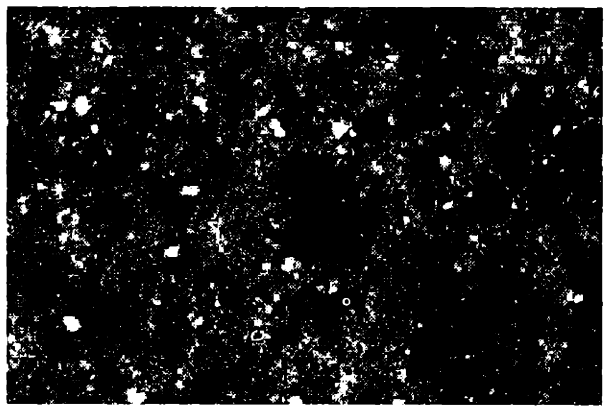

t = 50 μs

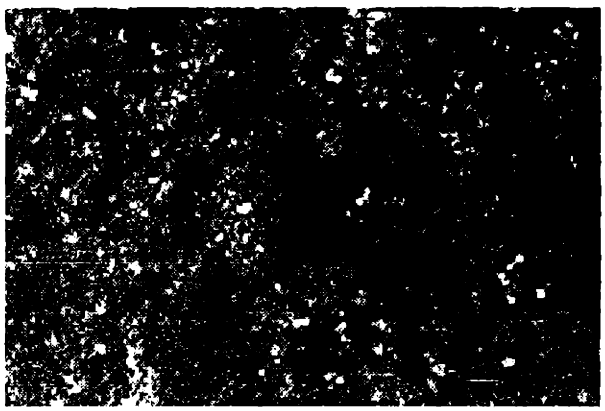

t = 46 μs

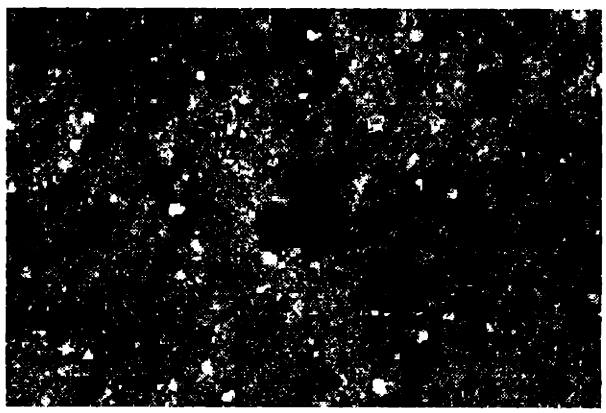

t = 52 μs

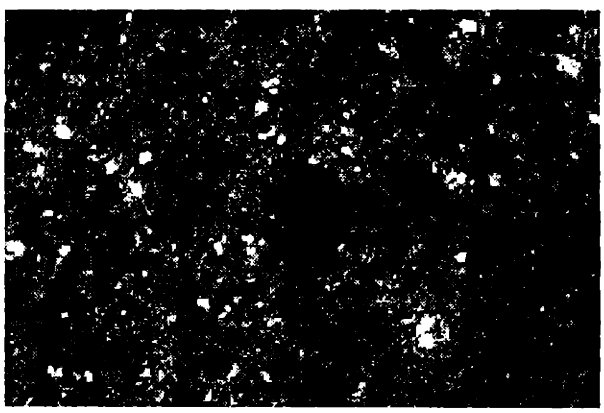

t = 48 μs

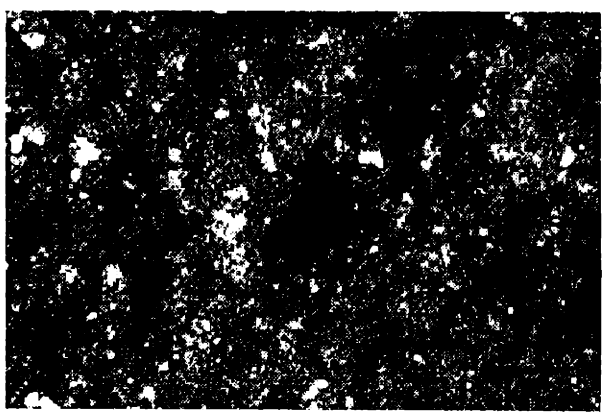

t = 54 μs

Figure 3.9 Initial stage of the impact cratering process on 25 μm flaky Al_2O_3 powder.

These observations indicate that the crater growth and development of the powder aggregate proceeded at the same time, and that the powder aggregate took shape before the crater opening stopped growing. While it cannot be determined from top view photographs when the vertical movement of the powder aggregate stopped, it is noted that in literature on high speed cratering and explosion cratering, it is commonly observed that crater depth stops development before the crater opening stops to grow.

3.4.2 Droplet Impact at Moderate Initial Velocity

Figure 3.10 shows a sequence of photographed events of a droplet - powder impact with an initial impact velocity of 8.01 m/sec on a powder bed of 10 μm spherical alumina powder, packed to 52.4% density. The diameter of the droplet was 84.9 μm. The event recorded in each frame was separated from the previous frame by 25 μs, except the last photograph, which shows the final result of the impact, 175 μs after it started.

Blue dye was added to the water to increase visibility of the droplet. A blue-dyed droplet is clearly seen in the first photograph in the series. Judging from these photographs, the primitive ball took on its final geometry about 100 μs after the impact started. The development of the crater finished at about 25 - 50 μs later.

It is also seen from these photographs that the aggregate was basically spherical. Their geometry shows fully in Figure 3.11, where the photograph was taken after the aggregates were taken out of their crater. This suggests that the liquid of the droplet mixed very well with the powder particles. This mixing is important in the creation of integrated features in Three Dimensional Printing, where insufficient or slow mixing of the liquid and powder is always a source of printing defects.

The photographs show that the formation of the aggregate progressed at the same time as the crater opened up. This is consistent with the aggregate - crater development observations made in the last section. In both cases, as a droplet struck a powder bed, the droplet did not spread over the powder bed first and then seep into the powder bed. Instead, the droplet formed a mixture with the powder, and it was this mixture which moved further into the powder bed and pushed dry powder away.

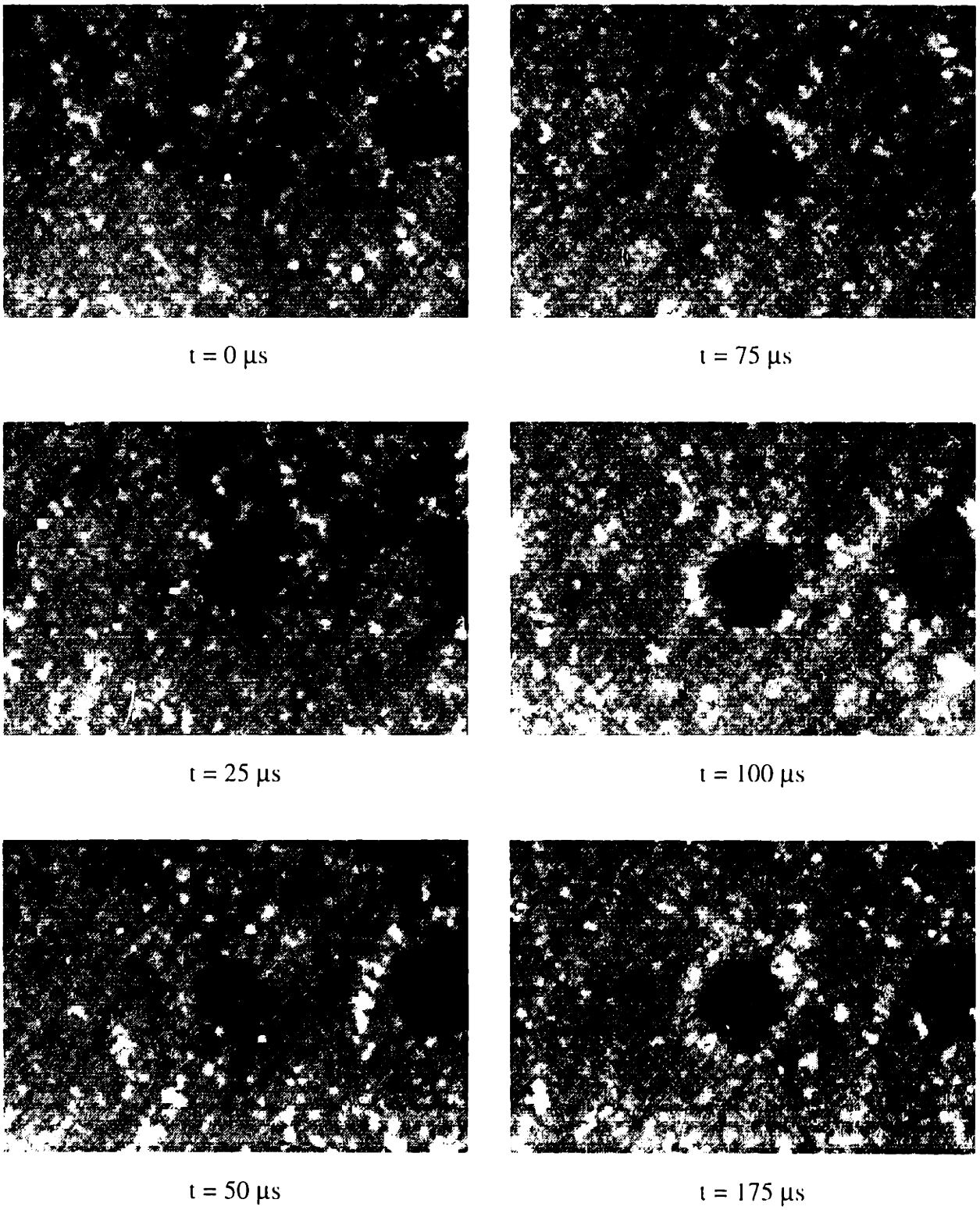

Figure 3.10 Impact cratering process on CB-A10 powder bed.

Figure 3.11 Primitive balls printed on CB-A10 powder bed.
(Two balls were outside their craters after the powder bed was slightly taped. Their spherical shape was clearly seen. One ball on the right was still in the crater. The shadowed circular areas were the craters. The light was from upper left.)

In other words, there was not two separated stages associated with the impact process, but one process involving two simultaneous events.

On the other hand, these photographs do suggest that at lower impact velocity, the development of the powder aggregate would finish sooner, and the powder bed reaction would be less energetic, so that the crater growth would stop earlier. In these samples, the elevation of crater rim was diminutive, suggesting that the movement of the powder induced by the impact was mainly downward into the powder bed.

3.5 Conclusion

Direct observation of impact events involving a single microscopic droplet and a deformable loose powder bed offers valuable information for assessing the spatial and temporal scales of the dynamic process. Single frame stroboscopic photography allows observing those transient and minute events in details without resorting to extravagant equipment. This approach does require meticulous instrumentation and execution of the experiments, so that the events can be accurately timed and consistent data can be collected under experimental conditions well maintained and documented.

An observation station based on single frame stroboscopic photography was developed and operated successfully. Droplet speed measuring circuitry monitors the single droplet movement and uses this information automatically to compensate for the speed variations in timing the right moment for film exposure. Various adjustment mechanisms were implemented to make it possible and convenient to manipulate the liquid jet and handle the powder sample. Photographing through a 45 degree-mounted FS mirror exposes the scene of impact inside the growing crater.

The series of photographs compiled from the single frame impact pictures indicates that the formation of a primitive ball structure and the growth of a crater proceed simultaneously at the beginning, and the latter takes longer time to finish. For initial impact speed around 10 meters per second, the crater development in a loose alumina powder bed of nominal particle size 10 to 30 microns takes approximately 1 millisecond. This duration becomes shorter when the initial impact speed is reduced. This is also true when the powder bed is made stiffer.

It is also found that during impact in the investigated material system and parameter ranges, the mixing of liquid with the powder and the penetration of their mixture into the powder bed happens at the same time. It is conceivable that on stiff powder beds, especially the beds which do not deform under impact to an extent comparable with the size of the constituent particles, there would be clear demarcation in stages of the deceleration of the droplet and penetration of the liquid into the pores of the bed. However, for microscopic sized, invisid, wetting fluid droplet, the two stages, as suggested by the photographic observation, are not distinguishable.

CHAPTER 4

RESEARCH ON IMPACT PHENOMENA

4.1 Introduction

The formation of particle aggregates through an impact process between a microscopic droplet and loose powder bed is a phenomenon on which no references have been found in literature. This is presumably because of its lack of application. The closest research that can be found is in the area of soil erosion studies [Stringer; Al-Durrah and Bradford]. When rain drops fall onto soil, the soil particles become detached and are washed away by the ground rain flow. The focus of studies in soil erosion has always been to describe the cumulative effects of repeated impacts by millimeter-sized rain drops on soil detachment.

On the other hand, impact by a single projectile, of either liquid or solid, on targets of liquid or solid are widely studied in different fields. It is important to understand the differences and connections between impact phenomena of difference material systems. In our study of droplet - loose powder impact, understanding its connections and differences to other impact phenomena is one way to take advantage of existing knowledge from other fields and to identify the characteristic mechanisms relevant to the droplet-powder impact. This chapter will review some of these connections and differences.

The review will concentrate on impact systems in one way or another close to our subject of study. First we will look at the situation when the projectile is a liquid drop. The targets involved in this type of impact reported in the literature are mostly solid surfaces, most often unyielding flat solid surfaces, except in the soil erosion problem. We will also review studies of impacts on granular mediums. The projectiles studied in these studies are of solid form. The third type of impacts to be reviewed is between solid

particles and a liquid drop. Solid particle - water drop collision has been studied by researchers interested in cloud formation and industrial dust cleansing.

4.2 Droplet Impacts on Solid Targets

Liquid droplet impacts on solid objects raise concern in many circumstances, such as erosions caused by liquid drop impacts on airplane windshields or steam turbine blades, or the efficiency of heat transfer when water spray is used for cooling purposes. The examples are numerous. Except for a few cases, most studies dealt with non-deformable smooth solid surfaces. The possible physical damages to a solid target by impact of one droplet is negligible, and the only immediate physical outcome of the impact is drop deformation and radial outflow. The impacting drop will invariably spread, and, depending on the material properties and impact parameters, the spreading drop may splash, or even rebound. Generally recognized variables which affect the impact outcome are the impact velocity and impact angle, the diameter of the droplet, the density, viscosity and surface tension of the liquid, as well as whether the liquid can wet the solid surface. However, it has also been found that the properties of the solid surface, such as the compliance, the surface roughness and temperature have strong effects on the impact results. It can be expected that when the impact target is a loosely packed granular media, the responses of both the projectile and the target will be quite different from the situation where the target is a solid.

4.2.1 The Initial Stage

Since a solid surface hardly deforms under the impact from a single drop of liquid, the liquid has to conform to the geometry of the surface. On a flat surface, the liquid will flow radially outward from the initial contact point. Researchers agree that the impact velocity has a strong influence on the initial spreading of the liquid. By the principle of volume conservation, it is easy to show that at the initial contact stage the radius of the contact area will grow by the speed u_c,

$$u_c = u_i / \tan\Psi, \qquad (4.1)$$

where u_i is the impact speed and Ψ is the angle between the tangent line to the spherical drop at the boundary of contact area and the surface (Figure 4.1). Because the angle Ψ is small at the beginning, the contact area grows very rapidly [Field, et. al.].

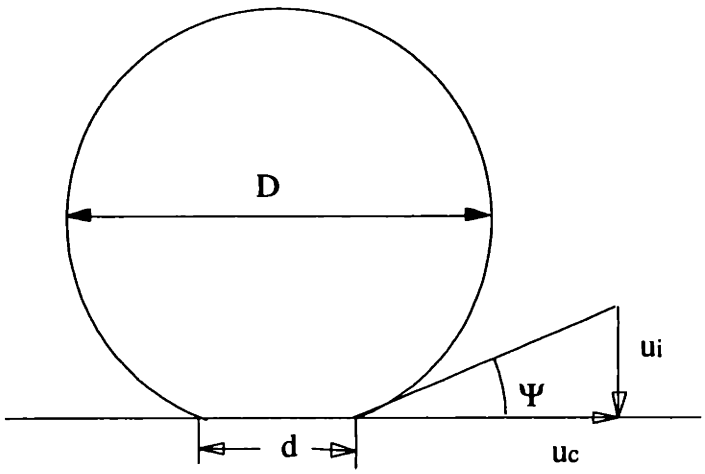

Figure 4.1 Initial stage of droplet impact on a solid surface.

Meanwhile, not all the initial spreading speed can be accounted for by the impact speed alone. [Stebnovskii] studied the initial stage of the contact between liquid drops (water and alcohol) and flat solid surface (glass and fluorite) using high-speed cinematography at a rate of 40,000 frames per second. The impact speed of a 3.0 mm diameter water drop was just 0.01 m/sec. His data showed that 80 μs after the initial contact, the radius of the contact area was 0.5 mm. So at that point

$$\tan^{-1}\Psi = \frac{1.5 - 10 \cdot 80e\text{-}6}{0.5} = 2.9984.$$

By Equation 4.1, the spreading speed u_c should be 0.01 m/sec • 2.998 ≈ 0.03 m/sec. However, 45 μs later the radius became 0.6 mm, so the average speed during this period was 2.22 m/sec. His data indicated that the initial spreading speed was dominated by the wetting forces when the impact speed is very low.

In Stebnovskii's experiment, the liquid films in the initial stage of spreading were very thin so the spreading front could not be seen from a lateral direction. A mirror put at an angle underneath the glass substrate enabled him to view the bottom of the spreading

liquid sheet well. By filming from this position, he determined the spreading speed at 25 μs after the initial contact was 15 m/sec, then dropped down to 10 m/sec in another 25 μs. From these observations he concluded that the spreading speed at the moment of first contact would be greater than 15 m/sec. In fact the speed can be extrapolated to 20 m/sec at time zero.

Stebnovskii also observed that the spreading speed increases with the impact speed. At an impact speed of 2 m/sec, he found the spreading speed was 27 m/sec at the instant of contact. At all impact speed, "the angle of wetting at the start is equal to zero, after which it increases slowly, remaining less than 90° for at least $13 \cdot 10^{-3}$ sec."

The initial stage of drop-solid surface contact discussed in this chapter is different from "early stages of spreading" discussed in some literature (e.g. by Cazabat) on wetting in large-time scale. In those latter studies, "early" is by comparison with seconds, minutes, hours, even days. The spreading in those studies is not in any way driven by the impact energy. The volume of the drop has already fully situated on the surface, and the advancing macroscopic edge of the drop assumes the macroscopic contact angle. Under this situation, the radius of the contact area, R, can be expressed by (de Gennes, 1985)

$$R(t) \sim \Omega^{0.3}(\sigma t/\nu)^{0.1}, \qquad (4.2)$$

where σ is the surface tension of liquid and ν is the kinematic viscosity, t is time, Ω is the volume of the drop, geometrically approximated by a spherical cap,

$$\Omega = 0.25\,(\pi R^3\ \theta) = \text{constant},$$

so

$$\theta(t) \sim t^{-0.3}. \qquad (4.3)$$

4.2.2 Spreading

Most researcher agrees that in the early stage of spreading the dominating factor is the inertial effect. In many numerical simulation work the surface tension and viscosity were neglected [Savic & Boult, Harlow & Shannon, and Huang et al., Reviewed by

Chandra], though without these factors the spreading will never not stop. Experimental observations and numerical simulations both have shown that the shape of the not-yet-spreading part on a drop remains spherical until that part also comes close to the surface [Loehr]. In time the whole drop becomes flattened and approaches its maximum radius of spreading. Spreading of a drop can be described by spreading factor β, the ratio of the diameter of the lamella, d, and the original drop diameter, D, as a function of time. (See Figure 4.1).

$$\beta(t) = \frac{d(t)}{D} \tag{4.4}$$

The deformation of the drop depletes the drop's kinetic energy. Since Engel (1955), several authors have estimated the spreading factor β by using energy balance.

$$(E_k + E_p + E_s)_{drop} = (E_k + E_p + E_s + E_d)_{lamella} \tag{4.5}$$

where E is for energy, the subscripts k, p, s and d stand for kinetic, potential, surface and dissipated. On any moment, the sum of lamella's kinetic, potential, surface energy, and the dissipated energy has to be the same as the total energy of the drop before the impact.

[Chandra and Avedisian], in their often-referenced study on drop impact on solid substrate, calculated β_m, the maximum spreading factor by energy method. They neglected the potential energy before and after the impact. Before the impact, the kinetic and surface energy for a spherical drop are

$$E_{kl} = (\tfrac{1}{2}\rho U^2)(\tfrac{1}{6}\pi D^3) \tag{4.6}$$

$$E_{sl} = \pi D^2 \sigma. \tag{4.7}$$

where U is the initial impact velocity, D is the diameter of the drop, ρ is the density of the liquid, and σ is the surface tension of the liquid.

When the lamella reaches the maximum radius, the kinetic energy of the lamella is zero. The surface energy was calculated by following [Ford & Furmidge], approximating

the lamella with a cylinder and neglecting the surface energy contribution from the side surface,

$$E_{s2} = (\tfrac{1}{4}\ \pi d_{max}^2)\ \sigma\ (1 - \cos\theta) \qquad (4.8)$$

where θ is the contact angle, d_{max} is the maximum diameter.

The dissipated energy was estimated by

$$E_{d2} = \tfrac{1}{4}\ \pi\ \mu\ (U/h)\ D\ d_{max}^2 \qquad (4.9)$$

where h is the thickness of the lamella, and μ is the viscosity.

From energy conservation, they got an equation in terms of the Weber number and Reynolds number,

$$\tfrac{3}{2}\frac{We}{Re}\ \beta_{max}^4 + (1 - \cos\theta)\ \beta_{max}^2 - (\tfrac{1}{3}\ We + 4) \approx 0 \qquad (4.10)$$

where

$$We = \frac{\rho U^2 D}{\sigma} \qquad (4.11)$$

and

$$Re = \frac{\rho U D}{\mu} \qquad (4.12)$$

They let Re to approach infinity, then got

$$\beta_{max} = \sqrt{\frac{We/3 + 4}{1 - \cos\theta}} \qquad (4.13)$$

Equation 4.13 gives the maximum spreading factor higher than what they observed in their experiments. For observed $\beta_{max} = 4$, the equation gives a value of 4.8, an overestimate of 20%.

For a water droplet of 85 μm diameter, if it strikes on a solid surface with an impact velocity of 8 m/sec and assuming a contact angle of 90°, σ = 0.072 N/m, the Weber number would be 75.6 and the Reynolds number is 680. By Equation 4.13, the maximum spreading factor would be 5.4, so the drop would, by the prediction of this equation, spread to 460 μm diameter and a thickness of 2 μm. By Equation 4.10, the maximum spreading factor would be 3.25. In the cylindrical approximation the drop of 85 diameter would become a cylinder of 276 μm diameter and 5 μm in height.

[Asai et al.] studied ink drop impact on different kinds of paper. The drop diameter and the impact velocity varied in the ranges of 44 - 81 μm and 2.5 - 20 m/sec, respectively. The viscosity and surface tension were in the ranges 2.0 - 7.5 cP and 0.050 - 0.054 N/m, respectively. They also used the energy conservation principle, and fitted their data into an empirical equation

$$\beta_{max} = 1 + 0.48\ We^{0.5}\ \exp(-\ 1.48\ We^{0.22}\ Re^{-0.21}) \qquad (4.14)$$

For a water drop of 84 μm diameter with We = 75.6 and Re = 680 (the same as the case tested using Equations 4.10 and 4.13), the maximum spreading factor would be

$$\beta_{max} = 2.58$$

and the maximum diameter of the lamella would be 220 μm and a thickness of 8 μm.

The time a drop takes to spread on a solid surface has been investigated in several studies. [Asai et al.] reported that under their experimental conditions, it took 10 ~ 20 μs for the droplets to reach their maximum radius.

[Loehr] studied drop impact spreading over glass substrates in the ranges of Weber number from 200 to 1500 and Reynolds number from 4200 to 19700. The viscosity of water used in the experiments was adjusted by varying the amount of glycerol added. All of his results fit well with an empirical formula

$$\beta(t) = \beta_{max}\ (1 - \exp(-\tfrac{t}{T})), \qquad (4.15)$$

where t is the time and $T \approx D/U$.

Estimated by Equation 4.15, a 85 μm diameter water droplet at the speed of 8 m/sec, assuming the maximum spreading factor $\beta_{max} = 4$, the time for the spreading contact area to reach a radius of 180 μm would be

$$t = -T \ln(1 - \frac{\beta(t)}{\beta_{max}}) \approx -\frac{D}{U} \ln(1 - \frac{180}{85 \bullet 4}) = 8\ \mu s.$$

The time for this drop to spread to diameter of 300 μm (90% of the maximum contact diameter) is

$$t \approx -\frac{D}{U} \ln(1 - 0.9) = 24\ \mu s.$$

[Stow and Hadfield] measured the time for drops (We = 100 and Re = 3500) to reach the maximum spreading diameter over a buffed aluminum surface (Ra = 0.05 μm), at maximum spreading factor of 5, as

$$t_m = 6 * \frac{D}{2U} \qquad (4.16)$$

They did not observed splashing of the drop due to impact under this condition.

Using Stow and Hadfield data as an reference, for a 85 μm diameter water drop at 8 m/sec impact speed, the spreading diameter 25 μs after the initial contact would be, $\beta_{25\mu s} = 4.7$, D = 400 μm.

Calculations in this section indicate that, if the impact target behaves like a solid surface, a water droplet of 85 μm and initial impact speed of 8 m/sec would spread to from 2.6 to 5 times of its diameter in approximately 20 μs. This will be compared with the impact behavior of the drop on a loose powder bed.

4.2.3 Splashing

Splashing refers to the phenomena of smaller droplets separating from an impacting drop towards the end of the spreading or rebounding. Though the break-up usually happens at the end of spreading, Loehr observed that the perturbations which lead to the break-up already occur at the very beginning of contact ($t << D/U$). The number of perturbations does not change during the spreading, only that the magnitude becomes larger.

The Weber number is often used to represent the critical conditions where splashing occurs. The Weber number alone does not describe all impact conditions, such as the properties of the surface under impact. According to [Rein], this explains the large differences between critical Weber numbers reported in the literature.

[Wachters and Westerling] observed liquid drop splashing in their study of heat transfer. The solid surfaces used were a gold cylinder and a polished gold plate, heated from 178° to 400° C. Under these conditions the surface is non-wetting due to the present of the water vapor. The critical Weber number was defined using the diameter of the drops. They reported that "for several liquids (water, methanol, ethanol, butanol, 2-methylpropanol and carbon tetrachloride), this critical value appeared to be 80." "At lower Weber number ($30 < We < 80$) the drop never disintegrates until after it begins to rise up from the hot surface. The fluid stem may then become unstable; this results in the ejection of one or two smaller droplets from the top of the retracted drop. For smaller Weber numbers ($We < 30$), no drop disintegration was observed."

The lifting (rebounding) of drop from the solid target is typical for drop impact on a non-wetting surface. The same phenomena was reported by Chandra. By Wachter and Westerling, "the residence time of the drop on the surface appeared to be about equal to the first-order vibration period of a freely oscillating drop" when $We < 80$. This characteristic time was first derived by Rayleigh for small amplitude free vibration of water drops in air,

$$\tau = \pi \sqrt{\frac{\rho_l D^3}{16\sigma}} \qquad (4.17)$$

where ρ_l and σ are the density and surface tension of the liquid.

Surface roughness is another important parameter affecting the results of impact. The surface effects was investigated by Stow & Stainer (1977) and Stow & Hadfield (1981). The latter is also a systematic study of the influence of impact velocity and the radius of the incident drop on the dynamics of drop impact on unyielding dry metal surfaces (aluminum and steel). They found that spreading drops would not splash if the relation

$$R\, V_T^{1.69} < S_T \qquad (4.\ 18)$$

was satisfied. In Equation 4.18 R and V_T are the radius and critical impact velocity of the impacting drop. S_T , splashing threshold constant, is a dimensional quantity which is constant for a given liquid and solid surface. The unit of R is millimeter, and the unit of V_T is meters per second. This constant, by Stow and Hadfield, "is invariant with V_T and R for the surface under examination." They computed S_T based on their data for surfaces of various materials and surface roughness. The general pattern is that S_T is larger for smoother surface. On a rough surface (R_a = 12 μm) made from mild steel, S_T = 4.2.

Equation 4.18 indicates that for a water droplet of smaller diameter, the threshold impact velocity (beyond which splashing would occur) would be higher compared with a water drop of larger diameter. It is interesting to note that the R_a value of the mild steel surface is in the same order of powder beds in Three Dimensional Printing. On the rough steel surface, if the droplet diameter is 84 μm, then the critical impact speed would be

$$V_T = \left(\frac{S_T}{R}\right)^{1/1.69} = 15.1 \text{ m/sec.}$$

The drops studied in Stow and Hadfield were of a few millimeter in diameter. There is no direct proof whether the same rule (small droplets have higher threshold velocity in breaking up) can be extrapolated into the range of droplet diameter of micrometers. On the other hand, there is no proof that the trend would reverse for droplets in micrometer range.

4.3 Solid Object Impact on Granular Media

Impact of a solid object on a granular medium, or the problem of penetration, has the longest history of research in impact phenomena. It started as a military interest in developing more effective penetrators and, on the opposite, for improving bunker design or spacing of earth-covered shelters against impacts from bombs or artillery shells [Melosh]. Non-military applications of projecting solid objects into earth include soil explorations, geological surveys and some novel designs such as direct-embedding of ship anchors. An interesting application in this area is the lunar rock drop test, which was conducted during the Surveyor VII landing on the moon. A robot arm picked up a rock from the moon surface and then dropped it. By studying the depth of the impression formed by the impact, researchers estimated the bearing capacity of the moon soil [Wu].

The lunar rock drop test was a low speed impact test. More often solid impact studies involve impact speed of at least tens of meters per second, and in most cases the speed is much higher. The results of high speed impact on granular semi-infinite space are deep penetration. The scale of droplet - loose powder impact is by no means comparable with those penetrations. However, studies on impacts in different systems and different ranges may face similar issues and can share the same approaches. The common target material, granular medium, makes this connection even closer.

4.3.1 Approaches to Penetration Problems

Studies on the penetration of projectiles into granular medium are usually concerned with the depth of penetration. From a mechanics point of view, this is "an extremely difficult problem" [Wright and Frank]. It involves large plastic deformations, higher stresses, large stress gradients, high strain rates, etc. The behavior of materials under these conditions are not well understood, and studying them are difficult [Zukas, 1]. "Relatively a small theoretical effort has been put to enhance understanding of the phenomena and acquire reliable calculation tools. Most of the research effort to study this problem is empirical, and as a result, empirical and semi-empirical formulae have been developed with aid of which the maximum penetration depth may be calculated" [Yankelevsky]. Such an assessment is shared by many researchers in the field.

It is generally agreed that there are three levels of methodologies in dealing with the penetration problems [Wright and Frank; Nicholas and Recht]. These approaches are: (1) simple data correlation, (2) engineering models of intermediate complexity, and (3) full scale numerical simulation. Each approach has its strength and weakness. Data correlation draws empirical knowledge from extensive testing. They can be extremely useful if good correlation can be found. Its weakness is that, despite tremendous efforts and huge amount of accumulated data, the empirical relationships developed in penetration problems were found to be not accurate or dependable when extrapolations were made for domains outside of the original investigations.

Engineering models are developed by applying conservation laws for mass, momentum and energy, combined with simplified assumptions regarding the deformation of failure process, kinematics and internal forces. The simplifying insights are based on prior observations. "This approach can range anywhere in sophistication from a simple one-dimensional penetration model based on a single mechanism to more complex two- and three-dimensional models combination of mechanisms and assumed deformation fields" [Nicholas and Recht]. As stated by these two authors, "It is sometimes difficult to distinguish the first and second approaches in the literature because there can be overlap in the methods used." The distinction between the first two methods is further blurred due to the fact that "many observations and curve-fitting schemes are referred to as models."

The third approach to penetration problems is theoretical investigation, which is closely associated with full scale numerical simulations. This approach starts with fundamental laws to find detailed stress-strain field and large deformations due to the penetration by using advanced numerical simulation programs, based on either finite elements methods, finite difference methods or discrete elements methods. Computer codes for impact simulation have been reviewed by many authors, such as [Anderson], and [Zukas,2]. Because penetration problems are extremely complicated, simplifications to the description of the physical phenomena are still necessary to make theoretical modeling possible. Besides, the accuracy of numerical results of a well designed simulation program depends on how realistic the input parameters are. The material properties or constitutive relations employed in these theoretical methods are often not available and hard to measure, if possible at all. A valid numerical solution can only be obtained through comparing their

results with experimentally collected data and adjusting the parameters accordingly. So theoretical approach to penetration problems cannot do without experimental data.

4.3.2 Modeling the Impact Penetration of Solid Objects into Granular Media

Because of the intensive attentions paid to penetration problems, numerous models have been proposed. This section is not a comprehensive review of all the work available in the literature. Rather, a few representative modeling efforts are given to exemplify the state of affairs in penetration research.

4.3.2.1 Young's Empirical Penetration Equation

As mentioned in the previous section, penetration research has relied heavily on the experimental approach. Experimental efforts intensified since the end of WWII. Young's equation is the most widely used empirical relationship for predicting penetration depth. This equation is the result of Young's analysis of 500 large-scale penetration tests conducted through 1967 to 1978. It relates penetration depth to the mass and geometry of the projectile, impact velocity and the property of the target soil, which is represented by a dimensionless constant S, called the soil constant. For speed less than 61 m/sec.,

$$P = 2\,K\,S\,N\,(W/A)^{0.5}\,\ln(1 + 2\,V^2 \bullet 10^{-4}) \qquad (4.19)$$

where

P = penetration depth (cm)
K = dimensionless mass scaling factor
S = dimensionless soil constant
N = dimensionless nose shape factor
W = projectile mass (kg)
A = projectile cross-sectional area (m^2)
V = impact velocity ($m\ s^{-1}$)

As reviewed by [Yankelevsky], there is no known relationship between the S number and the physical properties of the target soil. The value of S varies within a wide range of two order of magnitude. The selection of S number depends on the user's past

experience with the particular soil type the equation is applying to. [Young] proposed an estimate for the S number from dynamics cone penetrometer readings. With accurate selection of the S value, the equation predicted penetration depth within ±20% of the actual depths in full scaled penetration tests.

4.3.2.2 Cavity Expansion Models

In early 70's, a theory of "spherical cavity expansion", originally developed for calculation of static indentations of rigid indentators on elasto-plastic incompressible media [Bishop, Hill and Mott], was adapted to solve deep penetration problems [Hanagud & Ross]. Since then, cavity expansion models have been developed in various forms to solve deep penetration problems.

The basic idea of these models is to treat a penetration problem as a cavity, either spherical or cylindrical, which expands at a specified rate in a semi infinite homogeneous and isotropic medium. This expansion produces plastic and elastic response regions. The elastic region is considered as an incompressible elastic material. In the plastic region the compressibility is approximated as "locked strain", which does not vary with the hydrostatic pressure. The resistance forces consists of both static and inertial components. In calculating the forces the nose shape is taken into account by a sinusoidal function.

[Forrestal and Luk] presented one of such models for a slender projectile with an ogive nose. The final depth of penetration is given by

$$P = \frac{m}{2\beta_s} \ln\left(1 + \frac{\beta_s V_o^2}{\alpha_s}\right), \qquad (4.20)$$

where

P = final penetration depth

m = mass of the projectile

V_o = impact velocity

$\alpha_s = \pi a^2 \tau_o A[1 + 4\mu\psi^2(0.5\pi - \theta_o) - \mu(2\psi - 1)(4\psi - 1)^{1/2}$

$\beta_s = \pi a^2 \rho_o B C$

$$C = \left[\frac{(8\psi - 1)}{24\psi^2} + \mu\psi^2(0.5\pi - \theta_o) - \frac{\mu(2\psi - 1)(6\psi^2 + 4\psi - 1)(4\psi - 1)^{1/2}}{4\psi^2}\right]$$

a = radius of the nose

s = the curvature of the ogive nose

ψ = 0.5 s/a ("caliber-radius-head")

μ = sliding friction coefficient for the soil on the projectile nose

$\theta_o = \sin^{-1}(1 - 2\psi)$

$$A = \frac{1}{\alpha}\left(\frac{1 + 0.5\,\tau_o/E}{\gamma}\right)^{2\alpha} - \frac{1}{\lambda}$$

τ_o = shear stress at zero hydrostatic pressure

λ = the proportionality between shear stress and the hydrostatic pressure

E = Young's modulus of the soil

$$\alpha = \frac{3\lambda}{3 + 2\lambda}$$

$$\gamma = \left[(1 + \frac{\tau_o}{2E})^3 - (1 - \eta^*)\right]^{1/3}$$

η^* = locked volumetric strain

$$B = \frac{3}{(1 - \eta^*)(1 - 2\alpha)(1 - \alpha)} + \frac{1}{\gamma^2}\left(\frac{1 + 0.5\,\tau_o/E}{\gamma}\right)^{2\alpha}\left\{\frac{3\tau_o}{E} + \eta^*(1 - \frac{3\tau_o}{2E})\right)^2 - \frac{\gamma^3[2(1 - \eta^*)(2 - \alpha) + 3\gamma^3]}{(1 - \eta^*)(1 - 2\alpha)(2 - \alpha)(1 + \frac{\tau_o}{2E})^4}\right\}$$

The simple form of final solution and cumbersome definitions of input parameters are common to these cavity expansion models. While no empirical parameters are involved, the soil properties do require assessment through unconfined compression tests on undisturbed soil samples. These models assume the soils are incompressible. This assumption is acceptable for saturated clay soils, but not generally applicable for other granular materials.

4.3.2.3 Classical Models

"Classical" is not the name of this type of models known in literature. These models are called classical here because they are of the similar form as first suggested by Robins and Euler. They had suggested the deceleration of a projectile penetrating into a homogeneous media such as sand was a constant, γ,

$$-\frac{dv}{dt} = \gamma.$$

Another form, first proposed by Poncelet and tested in 1957 by [Allen, Mayfield and Morrison] has the form of a quadratic function of the velocity,

$$-\frac{dv}{dt} = \beta v^2 + \gamma. \tag{4.21}$$

The usual interpretations of these terms are that the term αv^2 represents the deceleration due to the reaction from the comminuted target material, and that the term γ represents deceleration due to breaking up of the structural network of the impact target. The final penetration depth, by integrating Equation 4.21, is

$$P = \frac{1}{2\beta} \ln\left(1 + \frac{\beta v_o^2}{\gamma}\right) \tag{4.22}$$

where P is the maximum penetration, and v_o is the impact velocity.

[Allen et al.] (1957) conducted penetration tests using slender hardened steel projectiles on dry quartz sand of about 1 mm size. The nose angle of the projectiles and the striking speed were varied in the tests. They concluded from their test data that there was a critical penetration speed v_c = 96.5 m/sec. Below this speed the maximum penetration depth could be expressed by Equation 4.20. In their equation, the parameters β and γ were regressed from the experimental data. The standard deviation of the β values was 13 %, while for the γ values was 57 %. No analysis had been done to correlate γ and β to the initial impact parameters such as the striking speed and the nose angle of the projectile. The variations appeared random.

The method adopted by Allen et al. is a variation of the empirical approach. Here a functional form of the process is proposed based on essential arguments of mechanics, then the parameters involved in these functions are evaluated experimentally from measured quantities which are also the variables in the function.

4.4 Solid Particle Collision With a Liquid Drop

Entry of a solid object into a liquid body much larger than it has been studied in contexts separated by tremendous scale differences, and the concerns are accordingly different. The impact between the bow of a ship with the water waves exerts tremendous dynamic load on the ship structure. This is an example of large objects impact on liquid body. In this area the subjects of study are on the stresses and strains induced in the impactor and the flow pattern of the liquid due to the impact.

An example of smaller solid objects impact with a larger liquid body is the collisions between air-borne solid particles, or aerosol, with liquid drops. These collisions are of importance in industrial dust cleansing by liquid scrubbers and the formation of clouds and rains. Research interests in this area are not on the stresses, strains or the flow pattern in the liquid. Researchers in this area are concerned about "collection efficiency", namely how much solid particles will be collected by the liquid body, and how much of them will skip the drop and be carried away by the air flowing around the drop. If the solid particles do strike on the drop, the question is whether the particles will readily enter the liquid. Studies in aerosol science have supplied experimental evidence on this kind of impact before observations were made in this study on Three Dimensional Printing.

We look into research in this area to answer the question whether solid particles can enter the liquid when they meet each other in an impact situation. Stebnovskii's observation of interaction between a liquid drop and a solid surface, reviewed in §4.2.1, has shown that if the liquid can wet the solid, the initial spreading of the liquid over the solid surface progresses fast, and is promoted by the kinetic energy of the liquid body. If the solid body happens to be a small particle, spreading of the liquid all over the particle surface will lead to engulfing of the particle by the drop. Experimental evidences have shown that, in situations where a liquid drop collides with solid particles individually, even if the liquid is non-wetting for the solid, the solid particles will not bounce off the drop surface. As put by Hinds, bouncing "is not a problem for liquids" in fine solid particles - liquid drop collisions.

[Stulov, Murashkevich and Fuchs] studied collisions between hydrophobic and hydrophilic solid particles and water drops. (Fuchs' book, The Mechanics of Aerosols, still

remains the most authoritative literature in the field of aerosol science forty years after its first publication.) In their experiment, the particles were carried by a air jet upward to impinge on suspended water drops of 1 - 2 mm diameter. Microphotographs were taken under flash illumination (20 kc/s) with a pulse length of 2 - 3 μs. The collision velocity was determined by the length of the imaged dashes.

In the first experiment the jet speed was 1 - 6 m/sec. Particles used were fractionated quartz, corundum and coal with particles size from 5 - 80 μm. No bouncing was observed visually. A small number of rebounding particles were found by examining micrographs. They interpreted these as particles accidentally impinging on other particles which just reached the surface of the drops. To verify this supposition, they carried out a second round experiments.

In the new round of experiments, they used lycopodium spores of 30 μm diameter, anthracite particles (5 - 100 μm) and spherical polystyrene beads (5 - 50 μm), and collision speed ranging from 0.5 - 12 m/sec. None of these particles wetted well, and the polystyrene beads were highly hydrophobic. Particles of these materials tended to stay on the drop surface. A jet of air was directed towards the drop surface to keep the captured particles from staying in the impact area, so the liquid surface was constantly renewed. They found that all colliding particles in this series, in spite of their hydrophobic nature, were captured by the water drops.

4.5 Conclusion

Impact phenomena between various materials happen naturally or as part of human activities. They are identified and studied wherever their scientific or engineering significance warrants attention. Microscopic aqueous droplet impact with loose bed of find solid particles is an area not explored in past and current literature. It becomes the topic of this thesis because it is an essential part of Three Dimensional Printing and because of lack of research in this area.

It is important to recognize the similarities and differences between impact behavior of the droplet - powder system and those of other systems. Droplet running into obstacles

of any forms will deform. The extent and process of deformation of the droplet depends on the structure and compliance of the target. A droplet of size and speed in the range relevant to Three Dimensional Printing does not cause appreciable deformation to solid or fibrous materials; the droplet will spread out to form a liquid lamella about four times of the droplet diameter in tens of microseconds on these targets. In contrast, droplet - powder interface in a loose, deformable bed remains curved over a much longer period. Research referenced in this chapter has shown that, when the target is a rigid rough surface, the droplet of the size in concern would be unlikely to break up upon impact until its initial impact speed reaches 15 meters per second. The highly compliant nature of the soft powder bed would extend this speed to a higher value.

Because the deformation of powder bed, the deceleration of the droplet would not be as sudden as it occurs on a solid target. Before the droplet comes to rest the particles in contact with the drop would be able to enter the droplet due to wetting and inertia effect. The research by referenced Russian scientists support such a conclusion. It should be noted that the fact that the particles at the liquid - powder bed interface are engulfed by the advancing droplet does not exclude the existence of contact pressure between the liquid and these particles and the existence of contact pressure between the particles at the interface and particles behind them.

Engulfing of solid particles is one of the feature distinguishing droplet - powder impact from solid projectile - powder impact. The deformation of solid projectiles is generally minimum when they are shot into soil materials at ordnance speeds. Deceleration of the projectile stems from deformation of the soil as well as the acceleration of the soil particles in front of the intruding object. In analyzing droplet - powder impact interaction, the gradual integration of the liquid with the powder particles loads the liquid with solid mass, its decelerating effect on the liquid body should not be overlooked.

Impact processes in any material systems are complicated phenomenon. All of them involve large deformation within a very short period. Observing these processes, regardless their geometric scales, has always been a technical challenge. Mathematical descriptions of these processes are inevitably built on either highly simplified physical models or data correlation. Computer simulations are not exceptions. Modeling droplet - powder impact process is one of such challenging tasks.

CHAPTER 5

A PENETRATION MODEL FOR IMPACT OF A SINGLE DROPLET ON A LOOSE FINE POWDER BED IN THE CONTEXT OF THREE DIMENSIONAL PRINTING

5.1 Introduction

Previous chapters have described experimental findings on the impact interaction of a single aqueous droplet and an alumina powder bed of 3DP characteristics. A particulate agglomerate is formed and penetrates into the powder bed during the impact. At the end a crater is formed and a primitive ball sits at the bottom of the crater. This chapter develops an engineering model to describe the penetration process and predicts the penetration depth of the primitive ball. The penetration depth refers to the distance between the top surface of the undeformed powder bed and the bottom of the crater. Impact penetration depth as modeled in this chapter is a function of the size and impact velocity of the droplet, and the packing density, material density and resistance to penetration of the powder bed, with the last property depending on the chemical and physical compositions and preparation of the powder bed.

The depth and diameter of a crater are two parameters commonly used to characterize the results of impact cratering in most impact studies in all fields. Most modeling efforts concentrate on predicting the depth of the penetration. The ratio between the depth and diameter of crater, observed experimentally or in a natural impact event, is often used to classify the type of impact. This ratio is correlated to the relative strength of the projectile and the target materials, as well as the kinetic energy of the projectile.

The depth of penetration is an important consideration in Three Dimensional Printing. With a given thickness of powder layers, shallow penetration may mean insufficient inter-layer stitching, which often results in delamination of the layers. Too deep a penetration may cause excessive amount of powder being pushed away from area around the droplet landing site. The presence of a stiffer substrate (for example, a printed previous layer) usually limits the maximal penetration depth. However, since the first layer of each part is printed on a virgin powder bed, the vertical position of this layer depends solely on the natural course of the impact and penetration of printed binder droplets. Among all the layers printed, printing in the first layer tends to have the largest penetration depth. Uneven penetration and lack of lateral development of primitive structures in the first layer degrades the surface quality and structural integrity at the bottom of a part. These adverse effects in the first layer may take a few more layers built on top of it to diminish.

It is important to understand what mechanisms affect the penetration depth and how. In this regard an engineering model can be used a tool probing for the truth. As discussed in Chapter 3, a droplet impact on the powder bed is an extremely rapid process. Direct observation of droplet - particle interaction in real time at a microscopic scale is a difficult task. On the other hand, a penetration model predicts the depth of penetration, and penetration depth is measurable after the impact process. So by comparing observed penetration depths with the predicted values, we will be able to determine whether the assumptions of the model bears truth. Thus the value of an impact penetration model is more than predicting penetration depth, it is a means to develop and improve our understanding the printing process. Such insight gives guidance to proper selection of printing parameters, such as the size of droplet and droplet velocity for the printing, as well as the properties of powder beds, all to achieve the desired printing quality.

The penetration model developed in this chapter draws on experimental observations discussed in Chapter 3. The characteristics of the material system studied in the observations was described in Chapter 1. So this model applies to conditions discussed in those two chapters. The assumptions used in the model are firstly based on the experimental observations, i.e., that the formation of the primitive ball progresses simultaneously with the development of the crater, and the primitive ball's shape can be approximated by a sphere. The first seven sections of this chapter interpret the observed

phenomena based on information reviewed in Chapter 4 and this chapter. These lay down the ground work for formulation of the equation of motion in section 8 of this chapter.

5.2 Physical Characteristics of Loose Powder Beds in 3DP

In order to model the droplet penetration on a loose powder bed in Three Dimensional Printing, it is important to recognize the differences between the loose powder bed and impact targets studied in other fields. Neglecting these differences and thinking of the loose powder bed as something it is not, for example, as a rigid solid target, or as a non-yielding porous material, will not lead us to the proper way to model the impact process studied in this thesis.

The following distinctions are made for target surfaces involved in impacts:
(1) By deformations: yielding and non-yielding,
(2) By structures: porous and non-porous,
(3) By pore size: large pores and small pores,
(4) By whether the porous structure disintegrates under the action of permeating liquid.

This list is not meant exhaustive; it serves to emphasize the essential aspects of a bed formed from loosely packed solid particles and its reactions when it is subjected to an impact from a liquid drop. Under droplet impacts, a rigid solid surface will neither deform nor absorb the liquid; a rubber film may deform elastically due to the impact but will not absorb the liquid nor maintain the deformation afterwards; a porous sintered block of powder will absorb the liquid but does not deform; on a sponge-like porous surface, the object may deform under impact but the skeletal structure will stay intact. However, a loose powder bed under droplet impact is none of the above. It deforms permanently; the liquid will mix with the powder particles to form a primitive ball; the ball has a boundary separating it from surrounding dry powder bed; in all areas affected by the impact, powder particles are dislocated and rearranged during the impact and the pore structures are changed. These essential aspects have to be considered collectively. Seeing one and losing sight of the others will not help fully appreciate the droplet impact behavior on a loose powder bed.

A loosely packed powder bed, the subject of this study, is yielding and porous. The powder particles stay together due to gravity and friction and contact constraints between the particles. Thus, contact between particles can withstand small compression forces, very little shearing forces, and no tension. Under the impact of a droplet, the particles will move relative to each other. Under the influence of a flowing liquid, the particles may disperse. Within the impact region the particles undergo large movements. The pores in the structures are not fixed, instead they are transient and able to disintegrate. If for convenience we draw an analogy between capillary tubes and powder bed's pore structures, that analogy needs to be understood with strong reservation, and should not be carried too far.

The average pore size in the powder bed is a few micrometers. For example, the average radius of pores in alumina powder beds made of 30 μm flaky particles is about 4 μm [Bredt]. Image analysis of cross-sectional micrographs of powder piles [Michaels] has shown a lower packing density in regions at the powder bed surface. Correspondingly, the average local pore size in these regions is lower than that inside the powder bed.

The top surface of the powder bed used in Three-Dimensional Printing is created by shearing. Powder is poured into a pile at the edge of the powder bed, then a counter-rolling rod pushes and levels the pile into a layer by shearing off the top part of the pile. The top surface is in fact a shear failure surface. Since dilation happens at the shear interface in granular media, the packing density at the top surface is lowered in the shearing process. The local packing density of the top surface of the powder bed is further reduced by the adhesion between the leveling rod and the powder particles. In counter-rolling, the rod surface moves away from the powder pile. Through adhesion, the rod pulls particles away with it. This is evident by the existence of a thin layer, maybe only one particle thick, of powder particles over the rod surface. These factors combine together to make the local pore size larger at the very top of a powder bed than the average pore size of the whole powder bed. The low packing density region is about a few particle diameter deep in a powder bed of spherical particles.

5.3 The Difference Between Droplet Impact on Loose Powder Beds and on Solid Surfaces: Spreading

On different surfaces, the consequences of droplet impact are different. On a non-yielding non-porous solid surface, the drop has to spread by following the surface contour. The spatial and temporal scale of spreading over such surfaces has been discussed in Chapter 5. Even on these surfaces, the compliance and geometry make a difference in the spreading of an impacting drop. On a compliant solid target, such as PMMA, tensioned metal strip, neoprene coated metal, and phosphor bronze, the initial spreading of impacting liquid drops were found delayed [Field, Dear and Orger]. On shaped surfaces, the spreading follows the local geometry; when the drop hit depressions on a ductile surface, the pressure was found to concentrate on the base of the depression and the initiation of high speed jetting was delayed [Dear and Field]. According to these authors, repeated high speed impacts on the depression caused the target material to be removed from the base area.

A loose powder bed behaves differently from a rigid surface in its ability to deform. As will be shown in the later section, the powder bed resistance to compression, namely its bearing capacity, can be approximated by a linear function of the depth of the powder layer, measured from the top surface. In a powder bed packed to around 40 % of maximum density, this linear depth range is about a few hundred micrometers. At the very top level, where the depth is zero, the resistance to deformation is almost zero. Under the impact pressure from the droplet, the powder bed surface in contact with the drop will be pushed to deform. Since the droplet has a convex surface, the contact is not simultaneous, the first point on the powder bed surface coming into contact with the droplet will cave in first, the surrounding areas will follow when contact is established there. This indentation effect clearly exists even when a drop is placed with negligible speed on to a loose powder bed. Later we will show that the liquid will start to mingle with the particles progressively during an impact, but that will not be obliterated, and does not contradict with the fact that the powder bed surface will cave in under the pressure.

So one of the major difference between a non-deformable surface and a loose powder bed in the situation of drop impact is that, where in the former case the drop has to spread since it is the only deformable body, on a loose powder bed both the powder bed

and the drop deform during the impact. The depression thus formed on the surface of the loose powder bed would function similarly as a depression on the solid surface as found by Field, i.e. the depression impedes the radial spreading of the droplet.

Figure 3.8 offers such evidences. It is seen from these photographs that 25 μs after the initial contact, the spreading is no larger than 100 μm. Fifty microseconds after the initial contact, a crater has formed; the diameter of this crater is around 180 μm. The crater reaches 200 μm diameter at seventy five microseconds; the top of the primitive becomes distinguishable. One hundred microsecond after the initial contact, the cratering process reaches the end, the final crater diameter is about 220 μm. The whole primitive has already become visible at that time. It is noted that if a drop spreads, the diameter of its spreading area is necessarily going to be smaller than the crater diameter seen on the micrographs at any moment.

The impedance of lateral spreading of droplet by a loose powder bed become more evident when compared with what would happen over surfaces other than loose powder beds. The diameter of the contact area of spreading drop on various surfaces can be estimated by using equations reviewed in Chapter 4. Table 5.1 compares these results with the observed from the loose powder bed.

Table 5.1
Spreading of a Water Drop During Impacts over Various Surfaces
(Impact condition: water drop of 85 μm diameter, V_o = 8 m/sec.)

Source	Surface	Time	Contact Area Diameter
(Figure 3.10)	Loose powder	25 μs	< 100 μm
Ch.4, Eq.(4.14)	Paper	20 μs	218 μm
Ch.4, Eq.(4.15)	Glass	24 μs	300 μm
Stow & Hadfield	Al (Ra = 0.05 μm)	25 μs	400 μm

The cratering and primitive formation process shown in Figure 3.10 makes clear that there is not a separate spreading process prior to the cratering penetration. This can also

be deduced from the energy point of view. As argued by many authors (Chapter 4), spreading of a drop upon impact consumes kinetic energy (Equation 4.5). If a drop were to spread over a powder bed to the full extent as it would on a solid surface, there would be no kinetic energy left for the drop to make a crater. Even though a still drop would be able to move into the pores due to capillary forces, a crater would not be created by that action.

5.4 Spreading of Liquid Over the Surface of a Small Solid Particle: Engulfing

At the end of the liquid drop impact on a solid surface, the drop will retract and form a sessile drop, i.e. a drop sitting on a solid surface, contacting with the solid surface in an angle at the liquid-vapor-solid three-phase boundary line. Usually, wetting means the contact angle is zero or close to zero, and non-wetting means that the angle is greater than 90°; in the latter case the drop may form a ball and run off the surface easily [Adamson].

Distinction should be made between static contact angle and dynamic contact angle [de Gennes]. Static contact angle θ_o is a thermodynamic quantity, reached when the drop is in equilibrium state. The sessile drop has the smallest surface energy in this configuration. θ_o is determined by Young's equation.

$$\gamma_{sl} + \gamma_{lv} \cos \theta_o = \gamma_{sv} \qquad (5.1)$$

where

γ_{sl} = the interfacial energy between the solid and the liquid,

γ_{lv} = the interfacial energy between the liquid and the vapor,

γ_{sv} = the interfacial energy between the solid and the vapor.

The vertical component of tension, $\gamma_{lv} \sin \theta_o$, is balanced by forces which cause the solid to be strained. If the modulus of elasticity of the solid substrate is low, the solid will deform so that a ridge will be created along the three-phase contact line.

Static contact angle is independent of the surface geometry of a rigid substrate [Adamson, Chapter VII]. "θ_o is the same on a curved surface, inside a capillary or at any point on an irregularly shaped surface." [Israelachvili, Chapter 15] The contact angle of distilled water on alumina is about 8.6°.

Dynamic contact angle is different. By Israelachvili, "when an interface advances along a surface the 'advancing' contact angle, θ_A , is larger than the 'receding' angle θ_R . This is known as contact angle hysteresis and there has been an ongoing debates to its origins" (Figure 5.1). "Since the interface is not retracing its original path when it recedes, so that the process is not thermodynamically reversible. it is not immediately obvious which, if any, of the two contact angles represent the truly equilibrium value."

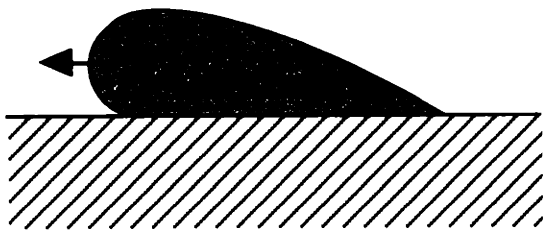

Figure 5.1 Advancing and receding contact angles
(Illustration modified after Israelachvili).

If we consider what happens when a solid particle meets with a wetting liquid drop much larger than it, the contact angle concepts lead to an interesting result. Figure 5.2 shows that it is necessary for the solid sphere to substantially immerse itself in the liquid in order to satisfy the contact angle condition.

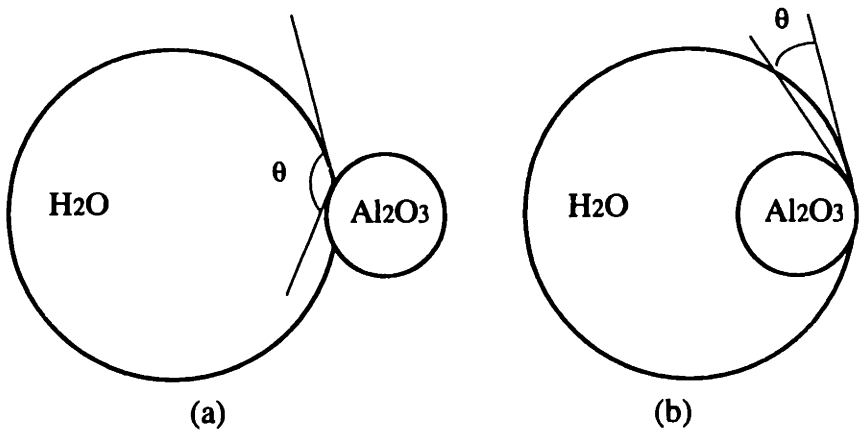

Figure 5.2 At small contact angles, a solid spherical particle is unlikely to stay outside a large wetting drop

The extent to which a solid sphere is drawn into the liquid drop can be expressed in terms of how much of the sphere remaining outside of the drop, as e in Figure 5.3. Scaling e by the radius of the drop, and by,

$$e = \overline{OO'} + r - R$$

we get

$$\frac{e}{R} = \sqrt{1 + f^2 - 2 f \cos \theta_o} + f - 1 \qquad (5.2)$$

where

r = radius of the solid sphere,

R = radius of the drop,

f = r / R.

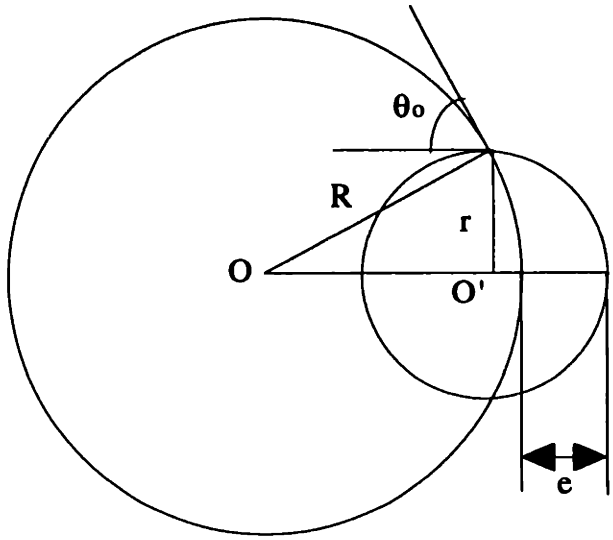

Figure 5.3 Calculating the portion of a solid sphere remaining outside a large wetting drop.

For a water drop of 85 μm diameter and an alumina spherical particle of 10 μm diameter, without considering any effects due to gravity or inertia, the solid particle needs to be almost totally immersed in the water drop (e/R = 0.15%) in order to satisfy the static contact angle condition . The actual result is of course that the particle is totally engulfed by the drop.

The spreading of the liquid over the surface of the solid sphere should be very quick. In Chapter 4, it has been shown that, by wetting alone, the spreading speed would be in the range of 20 m/sec. [Stebnovskii]. At that speed it takes 0.8 μs for a film of liquid to sweep over the surface of a solid sphere of 10 μm diameter.

During the impact between a droplet and a solid particle, if the particle is not supported, the particle will be accelerated in the direction the droplet is moving. An analysis of such a situation is given in Appendix II. It shows that , even if the promoting effect of wetting on engulfing is not considered, as long as the surface energy is such that it does not impede the engulfing, an initially stationary solid particle will be quickly overtaken by the advancing liquid drop due to the inertia of the particle. Particles in powder bed surface areas are not free to move; their movements caused by droplet impact are restricted by particles underneath and beside them. Engulfing these particles takes less time than the situation analyzed in Appendix II.

5.5 The Difference Between Droplet Impact on Loose Powder Beds and on Rigid Porous Surfaces: Absorption

Unlike loose powder beds, many porous surfaces are strong and will not yield to the impact from a small droplet. Whether an impacting drop spreads over a non-yielding porous surface depends on how fast the drop enters the pores through capillary actions. Most studies in this area involve placing a liquid drop at negligible speed onto a surface of small pores; their interest is in studying the capillary penetration rate.

If a liquid does not wet a solid material, capillary penetration will not occur even if the solid is porous. This is how water-repellent fibers work [Adamson, Chapter 10]. By the Laplace equation, pressure difference exists between inside and outside of a curved liquid surface according to

$$\Delta P = \gamma \cos \theta_o \left(\frac{1}{R_1} + \frac{1}{R_2}\right) \qquad (5.3)$$

where

ΔP = the pressure difference between inside and outside the liquid,
γ = surface tension of the liquid,
R_1 , R_2 = the principle radii of curvature of the liquid surface, and
θ_o = the contact angle.

As shown in Figure 5.4, the water head forces the non-wetting liquid to form a convex surface between the fibers. As long as the hydrostatic pressure does not exceed ΔP, the water will be supported by the meniscus.

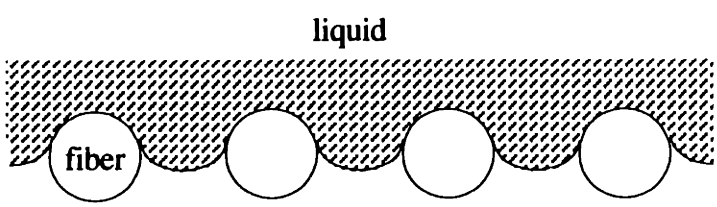

Figure 5.4 Water repellency of fabrics
(Illustration modified from Adamson).

Three Dimensional Printing needs to get the liquid binder into the particle material, so the materials are selected such that the liquid wets the powder. Wetting liquid will get into porous substrate through capillary penetration. Since most literature on capillary penetration into porous materials assumes the porous media have fixed structures, we examine what the penetration rate would be if the powder bed pores stay intact in spite of the invading liquid.

Pores in a powder bed are inter-connected and their sizes are not uniform. Capillary penetration into this network is a complicated process. In order to make this problem tractable, a simplified model of capillary tubes is often used. The most widely used equation of kinetics of penetration into a cylindrical capillary tube is the Washburn's equation [Marmur].

The basic assumptions behind Washburn's equation is that the liquid flow in a uniform capillary tube is subjected to viscous effects, not inertial ones, so that it is a Hagen-Poiseuille flow. The flow is driven by capillary force as well as pressure gradient, and is assumed not limited by the liquid supply [Wahsburn]. Under these conditions, for a straight vertical tube, the flow speed is:

$$\frac{dl}{dt} = \frac{[P_o + \rho g l + \frac{2\gamma}{r}\cos\theta]\, r^2}{8 \eta l} \qquad (5.4)$$

where

l = the length of capillary penetration,

t = time for the flow reaches length l,

$\frac{dl}{dt}$ = the speed of capillary penetration,

P_o = the liquid pressure at the starting end of the tube,

r = the radius of the capillary tube,

g = gravitational acceleration,

ρ = the density of the liquid,

γ = the surface tension of the liquid,

θ = the contact angle,

η = the viscosity of the liquid.

For capillary tubes with radius of a few micrometers, the capillary length, h, where

$$h = \frac{2\gamma \cos\theta}{\rho\, g\, r}, \tag{5.5}$$

is a few meters, so for shallow penetration of a few hundred micrometers into a thin capillary, the gravity term can be neglected . Thus Equation 5.4 becomes

$$\frac{dl}{dt} = \frac{[P_o + \frac{2\gamma}{r}\cos\theta]\, r^2}{8\,\eta\, l} \tag{5.6}$$

which integrates to

$$l = \frac{r}{2}\sqrt{\frac{[P_o + \frac{2\gamma}{r}\cos\theta]\, t}{\eta\, l}}. \tag{5.7}$$

Substituting Equation 5.7 into Equation 5.6 for l, Equation 5.6 becomes

$$\frac{dl}{dt} = \frac{r}{4}\sqrt{\frac{P_o + \frac{2\gamma}{r}\cos\theta}{\eta\, t}}. \tag{5.8}$$

Note that Equation 5.8 does not cover the time zero, where this equation becomes singular. In fact, Washburn's equation only applies after the Hagen-Poiseuille flow has been established. For a length l_o at the entrance of the capillary, the penetration is governed by another relationship, first found by Osburne Reynolds,

$$\frac{2r\rho}{\eta}\frac{dl}{dt} = k. \tag{5.9}$$

k is a dimensionless constant, which was found by experiment to have the value of 2000. According to Equation 5.9, the capillary penetration speed at the entrance of a tube of a few

micrometer diameter would be extremely fast. For example, the speed would be 200 m/sec. for a tube of 5 μm radius.

Washburn estimated the length of this fast-penetration region, l_o , by substituting laminar flow velocity into Equation 5.9. Following Washburn and substituting Equation 5.6 into Equation 5.9, the length of the initial fast penetration is

$$l_o = \frac{[P_o + \frac{2\gamma}{r}\cos\theta]\, r^3\, \rho}{8000\, \eta^2}, \qquad (5.10)$$

which is usually very small for small capillaries. For water entering a capillary of 5 μm diameter, l_o is about half of a micrometer. l_o is "entirely negligible for very small capillaries" [Washburn].

In situations where the liquid comes from a drop of small size, the limited liquid supply and Laplace pressure due to the curvature of the droplet surface should also be taken into consideration [Marmur, 1988 (1) ; Marmur, 1988 (2) ; Marmur, 1992; Denesuk, et al. 1992]. The pressure term in Equation 5.8, P_o , is replaced by Laplace pressure inside the droplet,

$$\Delta P = \frac{2\gamma}{R}, \qquad (5.11)$$

where R is the radius of the droplet, as in Figure 5.5. As the liquid moves from the droplet into the capillary, the curvature of the droplet will increase, and ΔP will gradually decrease. If the capillary radius is much smaller than the droplet radius, the original droplet radius R_o can be used as an approximation to the ever-changing droplet's radius of curvature at the initial stage of penetration. In Figure 5.5 the diameter of the capillary tube is exaggerated for the clarity of labeling details.

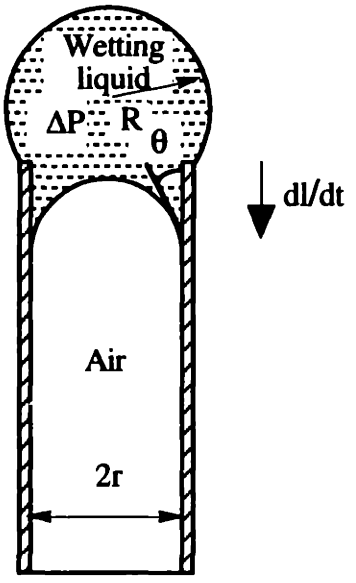

Figure 5.5 Capillary penetration of a small droplet into a fine tube.

Figure 5.6 shows the flow velocity in a capillary tube with a radius of 5 μm. The liquid is distilled water, the tube material is alumina. The values used in the calculation are:

ρ = 1000 kg/m, γ = 0.072 N-m, η = 0.001 Poise,

θ = 8.6°, r = 5 • 10e-6 m, R = D/2 = 42.5 μm.

These are the typical values for the materials and powder beds used in Three Dimensional Printing.

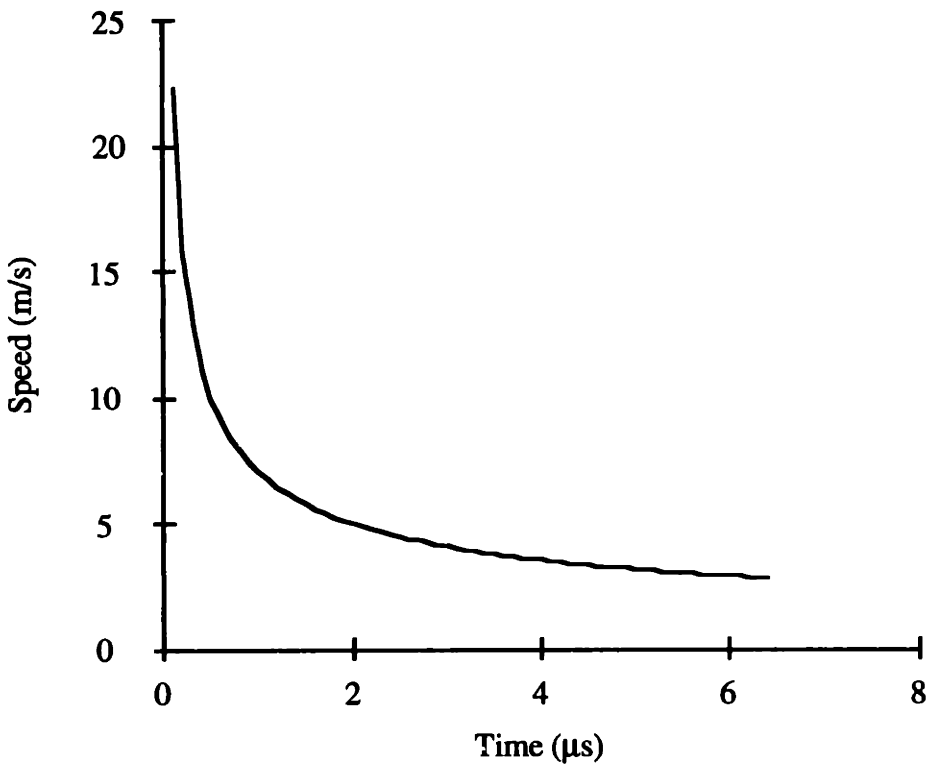

Figure 5.6 Flow velocity in a capillary tube of 5 μm diameter.

5.6 Deceleration of Water Drop in Loose Alumina Powder Bed

The capillary tube analogy helps to estimate how fast the liquid in a water drop would penetrate into the interstices of the powder particles through wetting. In the mean time we need to recognize that, unlike a tube, which is a continuous solid body, powder particles can be separated from each other by the invading liquid. Once water penetrates and saturates a alumina particle layer, it weakens any bonds that may exist between the particles, so that the particles can be dispersed due to the liquid's flow [Nelson]. Partially wetted particles floating on the surface of a drop is a different situation. The meniscuses between partially-submerged particles tend to pull these particles together [Kralchevsky et. al.; Paunov et. al.].

As soon as the particulate nature of the powder bed surface region is recognized, it becomes clear that the process of liquid (water) drop entering the interstices of the powder bed can be interpreted as a process of particles (alumina powder) entering the liquid drop as well. The second interpretation allows us to turn around to examine what happens to the velocity of the water drop when solid particles get inside of it. In order to do so we treat the particles as individual bodies.

Inside the water drop there will be relative movements between the solid particles and between the particles and the liquid. Given the dynamic and transient nature of the interactions, these motions are complicated and by themselves an intricate research topic. However, since the question we are tackling here is how the whole system – the mixture of the liquid and particles having entered the drop – behaves, we do not have to solve this internal multiphase flow problem with complicated boundary conditions before we can answer the question of current concern.

Any relative movements and interactions between the liquid and the particles inside a drop are internal to the system they constitute. A system's momentum is not affected by the interactions between bodies inside the system [Crandall, et al.]. Any change of the system's momentum is due to the external forces acting on the system at its boundary.

Figure 5.7 illustrates a water droplet at its early stage of impact on a loose alumina powder bed. In this figure, we note that (1) some solid particles are already inside the droplet[=]; (2) some solid particles are on the interface of the drop and the powder bed (underneath of the drop, not shown); (3) on those particles which are moving across the interface, the powder bed exerts distributed forces to resist the movement of the drop - powder mixture; these forces are external to the body of drop - powder mixture, and causes a loss of momentum to that body.

[=] FIGURE 5.7 is not an illustration intended to depict the real flow patterns inside the drop, so particle distribution and motion are randomly drawn. The forces associated with these motions do not affect the total momentum of the whole system.

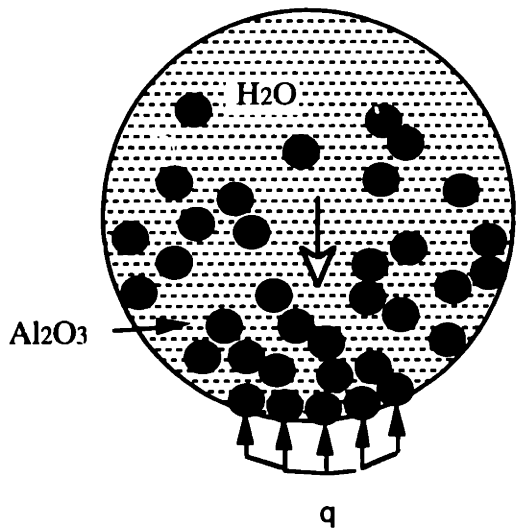

Figure 5.7 Illustrating conservation of momentum as Al_2O_3 particles enter a water drop. The exact pattern of the motion of the particles inside the droplet is not concerned here. The distributed pressure q represents the efforts of the powder bed resisting the drop - particle mixture's motion into the powder bed.

In the next section it will be shown that the powder bed exerts a resistive pressure on an intruding body, which is proportional to the penetration depth. While this pressure is external to the drop - powder mixture and will cause the drop - powder mixture to lose momentum, the resistance is small at the early stage of impact penetration since the penetration is still shallow. Meanwhile it can be shown that the major factor causing the deceleration of the drop - powder mixture at early penetration is the mass increase of this mixture due to the entering solid particles.

A droplet loses speed due to gaining of weight. In the parameter regime being concerned about in this study , each particles engulfed by the droplet during its early penetration into the powder bed has non-trivial contribution to the drop's deceleration, as shown in the following assessment. To simplify the assessment, we assume that the powder particles are spheres of uniform size, and quantify the mass increase of the mixture in terms of number of such spheres and the mass of each solid sphere. Let ΔM be the total solid mass entrained, m be the mass of each individual solid sphere, and n the number of spheres entrained, then $\Delta M = n\ m$. Let the mass and velocity of the droplet before

touching the powder bed be M_o and U_o , and for the moment neglect the momentum loss due to powder bed resistance force at early penetration since it is still small, then, by momentum conservation, the velocity of the drop - powder mixture after ΔM enters the drop is

$$u = U_o \frac{M_o}{M_o + \Delta M}$$

$$= U_o \frac{1}{1 + \Delta M/M_o} \cdot \qquad (5.12)$$

Substitute ΔM with n m,

$$u = U_o \frac{1}{1 + n\ m/M_o} , \qquad (5.13)$$

and let

$$s = \frac{1}{1 + \Delta M/M_o} , \qquad (5.14)$$

it is shown in Figure 5.8 how s changes with the increasing number of solid particles entered the droplet, n. In the calculation, the spherical particles are alumina (density = 3990 kg/m^3), 10 μm in diameter. The drop is distilled water (density = 1000 kg/m^3), 85 μm in diameter.

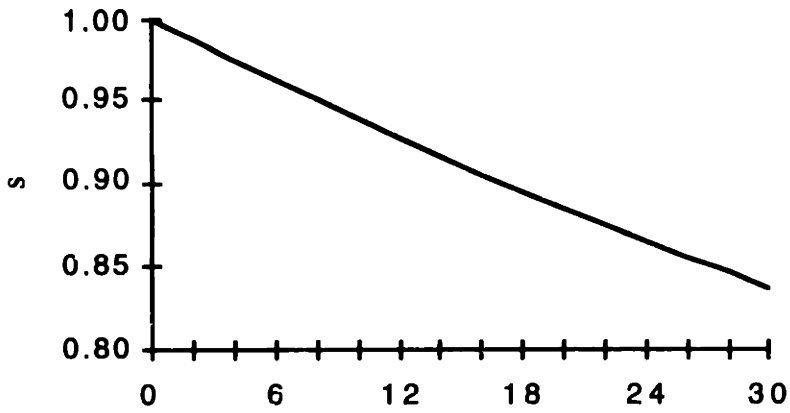

Figure 5.8 Velocity decreases rapidly with increasing number of solid spheres entering the droplet. Velocity = U_o * s

An powder bed of 10 μm diameter alumina spheres normally has a packing density about 40%. Simple cubic packing of spheres has a packing density of 52.3%, which is the closest to that existing in the powder bed among other stable simple packing patterns. The neck in this packing has an area-equivalent radius about 5 μm (4.6 μm) for 10 μm diameter spheres (see Figure 5.9.a). If we use simple cubic packing as a packing model for the powder bed, fifty 10 μm diameter spheres spread as one layer over an area which equals to the presentation area (cross-section at the equator) of a 85 μm diameter droplet, (see Figure 5.9.b). By Equation 5.13, gaining 50 alumina spheres of 10 μm diameter would reduce the velocity of a water droplet to 75% of its original velocity.

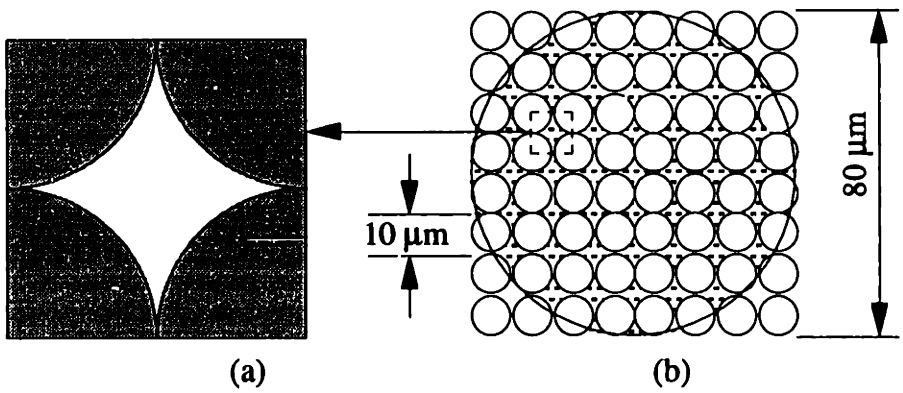

Figure 5.9 Simple cubic packing of 10 μm diameter spheres (top view).

The total number of solid spheres contained in a primitive ball at its completion of formation by a single droplet can be estimated by the following equation:

$$N = \frac{\phi'}{1 - \phi'}\left(\frac{D_d}{D_p}\right)^3 \qquad (5.15)$$

where

N = the total number of solid particles inside a primitive after its complete formation,

ϕ' = the packing density of particles inside the primitive,

D_d = the diameter of liquid drop,

D_p = the diameter of spherical solid particles.

Assuming a completely formed primitive ball contains 40% in volume of 10 μm diameter Al_2O_3 spheres, with the remaining 60% are pores filled with the liquid from a 85 μm diameter H_2O drop, then the total number of the solid spheres inside the ball would be approximately 410. By addition of solid particles alone, the speed of a drop - powder mixture would have a final speed 27% of the original speed of the water drop.

In general, it is preferable to use quantities that are easier to measure, such as packing density of the powder bed and the depth of the region having been permeated by the liquid, to keep track of the amount of powder that has entered the liquid rather than counting number of the spheres. As these quantities are adopted to describe the powder bed, the powder bed is idealized as a finely divided medium which is capable of entering the droplet continuously in infinitesimal increments. A mass of dM of this material occupies a volume of

$$dV_b = \frac{dM}{\rho_b} = \frac{dM}{\rho_p * \phi} \quad , \qquad (5.16)$$

where

dV_b = the volume occupied by dM inside the powder bed,

ρ_b = average density of the powder bed,

ρ_p = the density of the solid particle,

ϕ = the packing density of the powder bed, $\frac{\text{volume of the solids}}{\text{total volume}}$.

After a mass dM has entered the liquid, because the liquid fills all the interstitial spaces, the volume dM occupies in the liquid is

$$dV_l = \frac{dM}{\rho_p} = \phi \, dV_b \, . \qquad (5.17)$$

Thus, after the addition of ΔM, the volume of the drop - powder mixture is increased by the amount of dV_l .

This idealization makes it possible for us to keep track of the solid mass entering the liquid by integration, instead of by counting the number of solid particles. The latter method would inevitably require one to hypothesize about the packing configuration inside the powder bed, which is difficult to verify and its conclusion cannot be generalized to other packing configurations.

The rate that a liquid front advances inside powder interstices was discussed in the last section. In this section the emphasis is on how the engulfed solid particles affect the velocity of the drop - powder mixture. We now fit these two view points together by examining the movement of the center of mass of the drop - powder mixture. If the center of mass moves in step with the liquid front, or approximately so, we may assume that after the liquid drop strikes on the powder bed, the liquid mixes with more and more particles as their mixture moves along, until reaching a packing limit. The deceleration of the mixture is the combined effects of the increasing of mass, and the powder bed resistance to the penetration.

On the other hand, if the liquid front moves vastly faster than the mixture, the liquid invasion can be better approximated by purely capillary infiltration. If the liquid body moves vastly faster than the capillary front, some kind of solid-impact-on-powder approach may be more suitable; even though, as was discussed in the chapter on research in impact phenomena, research in solid-impact-on-powder problems have limited success for certain type of soil, and has not found ready solutions for granular media in general.

In estimating how many solid particles have entered the drop - powder mixture, Figure 5.10 can be used. The region where the liquid has mixed with powder is approximated by a segment of sphere, with a height of h, equal to the furthermost liquid

front, obtained from the section on capillary analogy. The volume of the segment of sphere is

$$V_b = \frac{1}{3} \pi h^2 (3R - h) ,$$

where R is the radius of the droplet.

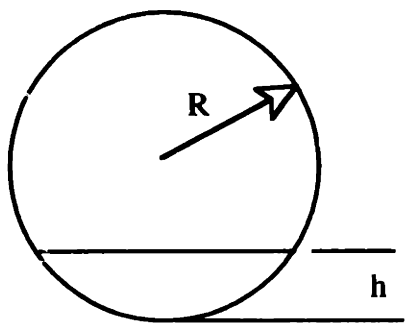

Figure 5.10 Estimating the mass increase due to engulfing of powder particles

Velocity of the center of mass of the drop - liquid mixture is estimated by using Equations 5.13, 5.17 and 5.18. The packing density is assumed to be 40%, typical to alumina powder beds in Three-Dimensional Printing. Initial velocity of the droplet is assumed to be 8 meters, the material densities are 1000 kg/m^3 for water and 3990 kg/m^3 for alumina. Droplet diameter is 85 μm. This calculation is an order-of-magnitude estimation; factors such as the volume change due to the engulfing of powder particles is not included here. A full consideration of all the factors is given in the following section where the model is described. The estimating results are shown in Figure 5.11, compared with the velocity of the water front estimated using capillary analogy, for the first six μs after the droplet contact with the powder bed starts.

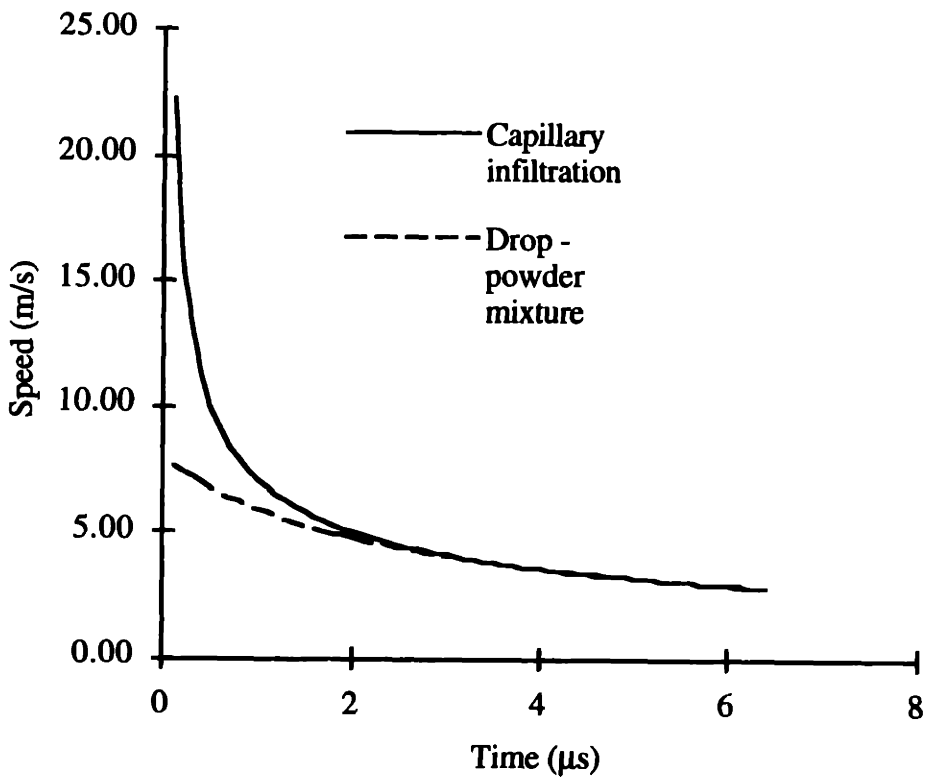

Figure 5.11 Comparing velocity of water front with the velocity of the drop - powder mixture.

Figure 5.11 indicates that in the initial stage (within 2 μs after the initial contact), the capillary velocity is higher than the velocity of the center of mass of the drop - powder mixture. The two velocities become almost identical after that. This suggests that the body of drop - powder mixture moves in step with the capillary front; so the mixing occurs along the way as the body of mixture pushes its way into the powder bed.

5.7 Powder Bed Resistance to an Intruding Body

Droplet impact on a loosely packed powder bed is not the same as a stationary liquid drop being absorbed by a powder bed. If the latter were the case, the observed deep cratering would not have happened, and the powder bed surface would have at most settled in somewhat under the capillary forces. In reality, the end product of a droplet impact on a loose powder bed is a granular pellet well separated from the surrounding walls of a crater,

and the crater bears every sign resulted from an impact. Before the pellet reaches the bottom of the crater, the powder bed must have resisted its advance, as it would resist anything which forces the powder bed to deform.

Granular material's resistance to a penetrating body is a function of the depth of penetration. [Goriatchkin et al.] (1936) found that, during pushing a rigid plate into soil, the penetration resistance q is an exponential function of the penetration depth, z,

$$q = k\, z^n \tag{5.18}$$

where k is a dimensional parameter. [Terzaghi and Peck] (1948) associated this relationship with soil failure through plastic flow. [Bekker] found that the parameter k can be modified to include the effect of plate size on cohesive soil,

$$k = (k_c / b + k_\phi) \tag{5.19}$$

where k_c is stiffness modulus for cohesive strength, and k_ϕ accounts for the soil strength due to friction. This suggests that for non-cohesive soils such as sand, the effect of plate size is negligible.

Penetration tests are employed to evaluate the bearing capacity of soils (Bekker) as well as of railroad ballast [Panuccio et. al.]. These tests are normally conducted under quasi-static conditions, by using a dead weight, or by mechanically pushing the plate into the soil at slow speeds.

Figure 5.12 shows a curve of penetration resistive pressure vs. penetration depth on a powder bed of alumina particles, obtained with a penetrometer described later in Chapter 6. The diameter of penetration pin is 1.067 mm (42 mils); the penetration speed is 21 μm per second. The maximum penetration depth is 0.5 mm, and the total sample thickness is 4 mm. The curve can be approximated by a power function in the form of Equation 5.18,

$$q = 2.54 \bullet 10^4 \bullet z^{0.629} \text{ Pa},$$

where the unit of z is meter.

The curve can also be approximated by two intercepting straight lines. For penetration depth smaller than $z_1 = 80\ \mu m$, the resistive pressure can be approximated by

$$q = k_1\ z \tag{5.20}$$

and for depth larger than z_1 where load is larger than $q_1 = k_1\ z_1$,

$$q = q_1 + k_2\ (z - z_1)\ . \tag{5.21}$$

Linearization of the pressure - depth relationship is often adopted by physicists in studying material behavior in the granular state [H.M Jaeger, et al.; Chu-heng Liu].

The origin of the penetration resistance is related to shear stresses acting on the failure surfaces in the granular medium, the friction forces between particles, and the friction forces at the frontal surface of the penetrating body. The friction forces on the side surfaces of a penetration probe are generally minimized by design and can be neglected. In any case the quasi-static penetrating body has to overcome the shear stresses in its course of penetration.

In civil engineering literature, two types of failure are identified in connection with ultimate bearing capacity of soils. One type is "general shear failure", where the failure surface in the soil extends to the ground surface. Another type, "punch failure", happens when the packing density is low (< 70%) or the loading is fast, and where the shear failure is local without extension to the ground surface.

The curve in Figure 5.12 features many small ripples, which indicates that during the slow penetration, particles in the pressed region constantly adjust their relative positions and orientations to reduce the stress. If at a certain point the penetration pin stops moving, the stress will gradually relax. At higher penetration speeds, the particles will have less time to adjust to follow a least-stress path. It can be expected that the stress will increase with the penetration speed. In droplet - powder impact situation, the strain is large and the

strain rate is very high. Strain rate effect is a factor that needs to be considered in this type of penetration.

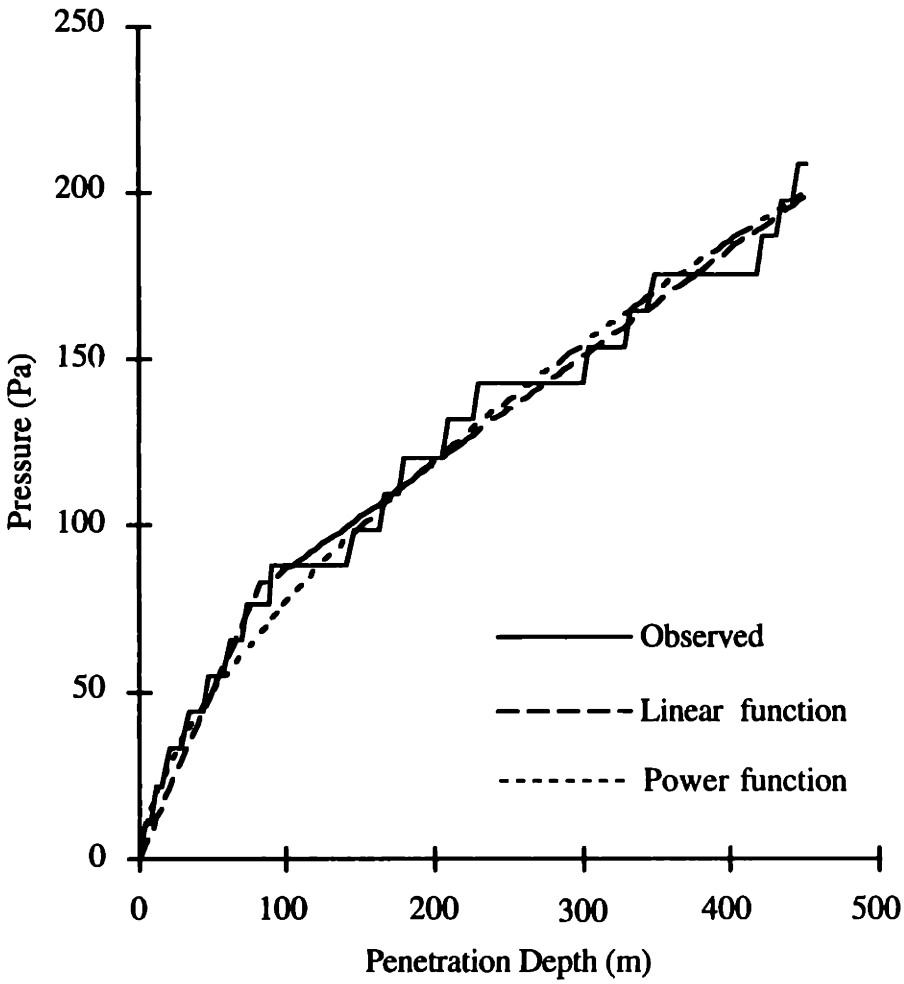

Figure 5.12 The relationship between penetration resistance and penetration depth.

In soils, the shearing resistance increases linearly with the logarithm of the rate of strain [Mitchell]. Assuming that under strain rate $\dot{\varepsilon}_o$ the bearing capacity is q_{bo} , then the bearing capacity under strain rate $\dot{\varepsilon}$ becomes

$$q_b = q_{bo}\,(1 + \alpha \log_{10} \frac{\dot{\varepsilon}}{\dot{\varepsilon}_o}) \,. \qquad (5.22)$$

Strain rate effects are also seen in metal powders. Figure 5.13 shows the dynamic stress - strain curve for a copper powder, where $\log_{10} \frac{\dot{\varepsilon}}{\dot{\varepsilon}_o} = 6.4$, and the stress increases by 6 to 7 times [Clyens & Johnson]. This strain rate effect is characteristic of the phenomenon of thixotropy [Billing & Tate].

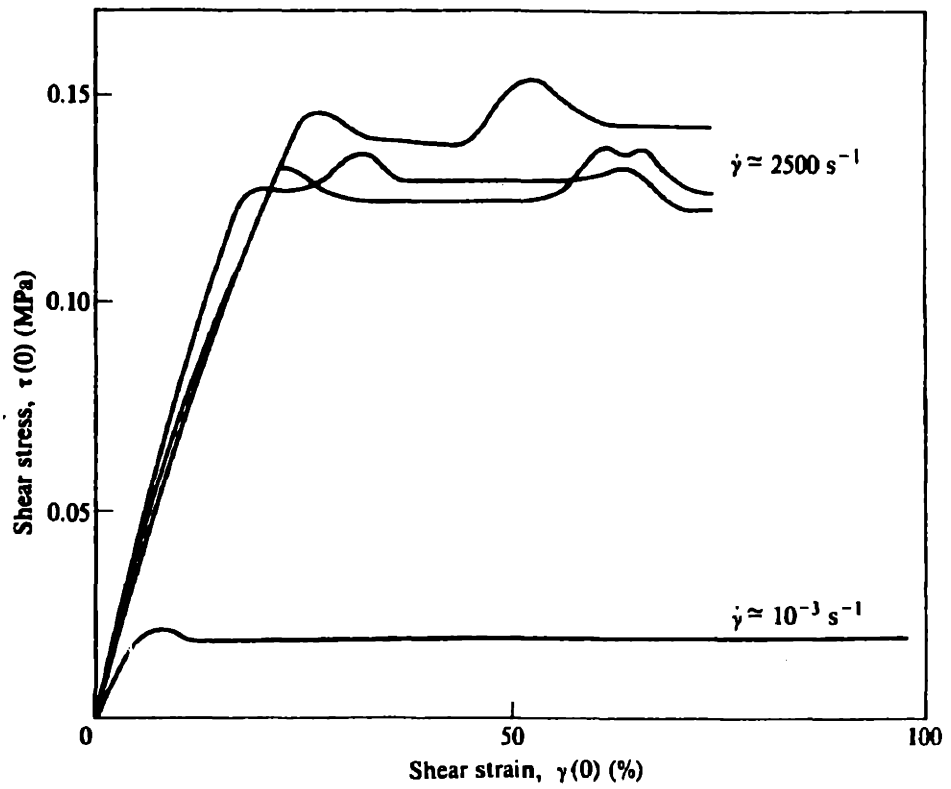

Figure 5.13 Dynamic stress-strain curve for a copper powder tested in simple torsion. (Clyens and Johnson, 1977).

It is widely accepted that most materials exhibit a dynamic strength greater than static strength [Goldsmith]. In metals, the dynamic strength of metals is taken as 3 ~ 4 times of the static strength [Hohler & Stilp]. For low speed indentation and liquid-solid impact erosion problems, a dynamic deformation resistance 3 times of static yield strength has been suggested for metals [Johnson; Bargmann].

In the droplet - loose powder bed impact studied in this thesis, impact speed ranges from 3 to 8 m/sec, in log scale this is five order-of-magnitudes higher than the rate used in the penetration test. The actual stress under the real impact condition is expected to be higher than that obtained from quasi-static test. This strain rate effect can be represented in a way similar to the references cited above, multiplying the stress under static conditions by a factor k',

$$q_d = k'q \tag{5.23}$$

where the subscript d identifies that q_d is dynamic stress.

5.8 A Model for Penetration Depth of a Droplet of Wetting-Liquid Impinging on a Loose Powder Bed

The previous sections in this chapter lay down the foundation for understanding how a droplet decelerates during its impact on a loose powder bed. Based on this information, a penetration model tailored to the droplet - loose powder bed impact problem relevant to the conditions presented in the current process of Three-Dimensional Printing is given in this section. These conditions are assumed because that the goal of study has been set as understanding droplet - powder impact phenomena under these circumstances.

This model assumes that the liquid has been selected in such a way that it wets the powder thoroughly. This is a necessary condition for Three-Dimensional Printing to be possible. The droplet size considered is around 100 μm or less, but no less than a few hundred times the size of the powder particles. The impact speed is about 10 m/sec or less. The particles are spherical or flaky in shape, with a nominal size about 10 - 30 μm. The powder beds are packed to about 40 % dense, with a pore size about 5 μm or larger. The powder bed is not pre-fixed. The model is developed to predict the penetration depth of the primitive pellet structure formed by a droplet with particles from the bed. In addition, by understanding the process of a single droplet mixing with the powder particles, the model benefits understanding phenomena associated with multiple droplet printing with or without overlapping.

Through observations in Chapter 3 and preliminary estimations described in previous sections, the droplet and the powder particles are capable of interpenetrating as their mixture impact into the powder bed under above conditions. The powder bed resists deformation and the movement of the drop - powder mixture by a depth related force. The primitive formation and the crater formation are two aspects of one process.

Because of engulfing of solid particles, the mass and the volume of the evolving primitive pellet is a function of time, hence a function of the penetration depth. At any moment in time, t, the momentum of the moving pellet, p (t), is found from the mass, m(t) and velocity, v(t)

$$p(t) = m(t)\, v(t) \tag{5.24}$$

Defining the cross-sectional area of the pellet orthogonal to its line of motion as its presentation area, $A_p(t)$, then after a short period of Δt the mass of the pellet will increase by $\rho_b\ v(t)\ A\ \Delta t$, where ρ_b is the average density of the powder bed, and the velocity changes by Δv, hence the momentum becomes

$$p(t+\Delta t) = [m(t) + \rho_b\ v(t)\ A_p\ \Delta t]\ (v(t) + \Delta v) \tag{5.25}$$

The momentum change is caused by the action of external force on the system, F, over the time period Δt. The force F, as discussed in Section 5.6, Figure 5.7, acts on the solid spheres at the boundary of drop - powder mixture and dry powder bed.

In its general form the external force, F, is also a function of time, hence of the depth, z.

$$\lim_{\Delta t \to 0} \frac{p(t+\Delta t) - p(t)}{\Delta t} = m(t)\frac{dv}{dt} + \rho_b\ v^2(t)\ A_p(t) = F(t) \tag{5.26}$$

In writing Equation 5.26, the powder bed is idealized as an infinitely finely divided medium with a density equal to the average density of the powder bed, so that integration can be used, as has been discussed in the previous section.

Equation 5.26 can be rewritten as

$$\frac{d^2z}{dt^2} = \frac{dv}{dt} = -\frac{A_p(z)}{m(z)}\left(\rho_b \left(\frac{dz}{dt}\right)^2 - F(z)\right) \qquad (5.27)$$

In the last equation, the fact that the mass of the drop - powder mixture, m(z), presentation area of the primitive, $A_p(z)$, and the resisting force, F(z), all change with the penetration depth z is emphasized. The depth z is measured from the original surface of the powder bed to the lowest point at the body of the drop - powder mixture. If the functional forms of these terms are known, the motion of the evolving pellet can be calculated from Equation 5.27 by integration.

$A_p(z)$ depends on the geometry of the drop - powder mixture. Before the droplet touches on the powder bed, the oscillations due to its breaking off from the continuous stream have long since dampened out, and its shape is approximately spherical. Starting from its contact with the powder bed, the drop will deform. However, as discussed in Section 5.2, the drop's deformation, by experimental evidence, is much subdued compared with the spreading of a drop over a solid surface. According to studies in droplet impacts on solid surfaces, the upper dome of a drop remains spherical until the region starts to spread, so we will assume that the dome also remains spherical in our current case. As discussed in previous sections, the lower part of the drop will not be totally flattened after touching the powder bed, because (1) the powder bed also deforms; the part first touched by the droplet deforms first, so in the affected region the powder bed should become a concave shape; (2) the liquid front moves into the powder at a speed more or less compatible with the main body of the droplet; and since the liquid front starts to develop where the drop's lower surface touches the powder bed locally, so that the liquid front would preserve, to a certain extent, the spherical shape of the drop's lower surface. By combining all these considerations, we may approximate the shape of the drop as a sphere.

Without this approximation, we may opt for methods adopted in current research in droplet impact on solid surfaces to track the evolving drop geometry through (1) experimental observation, or (2) numerical simulation, and develop methods and simulation tools suitable for loose powder bed. The results from these approaches are likely also approximations. This thesis does not take these approaches.

Along with approximating the geometry of the drop - powder mixture as a sphere, we consider the volume of the sphere expansion as the solid particles enter the body of the mixture, by an amount dV. So the radius of the drop - powder mixture is also a function of z, R(z).

$$A_p(z) = \sqrt{2\ R(z)\ z - z^2}\ . \tag{5.28}$$

$$dV = \phi\ A_p(z)\ dz \tag{5.29}$$

$$R(z) = \left[\frac{3}{4\pi}\right]^{1/3} \left[V_d + \int_0^z dV \right]^{1/3} \tag{5.30}$$

where ϕ is the packing density in the powder bed, and V_d is the volume of the original droplet.

The resistive force is obtained by integrating the resistive pressure q(z) over the spherical surface where the drop - powder mixture is in contact with the dry powder. Because the penetration depth is often within the linear region of the q-z curve, a linear approximation can be used to represent the depth related resistive stress as following:

$$q_d = k'\ k\ z = K\ z \tag{5.31}$$

where k is the slope of q-z curve obtained through quasi-static penetration test. k', as explained earlier, is a parameter which relates the stress under quasi-static condition to the dynamic condition. These two combines into K,

$$K = k'\ k. \tag{5.32}$$

Referring to Figure 5.14, two stages are considered in integrating the total resistance force: before half of the body of drop - powder mixture enters the powder bed,

the presentation area is smaller than the cross-section at the equator and increases with the penetration depth; after half of the spherical body enters the powder bed, the presentation area equals the cross-section at the equator. Accordingly,

$$F(z) = -\pi K z^2 (R(z) - \frac{z}{3}), \qquad \text{for } z < R(z) \qquad (5.33)$$

and

$$F(z) = -\pi K R^2(z) (z - \frac{R(z)}{3}), \qquad \text{for } z \geq R(z) \qquad (5.34)$$

The derivations of Equations 5.33 and 5.34 are given in Appendix III.

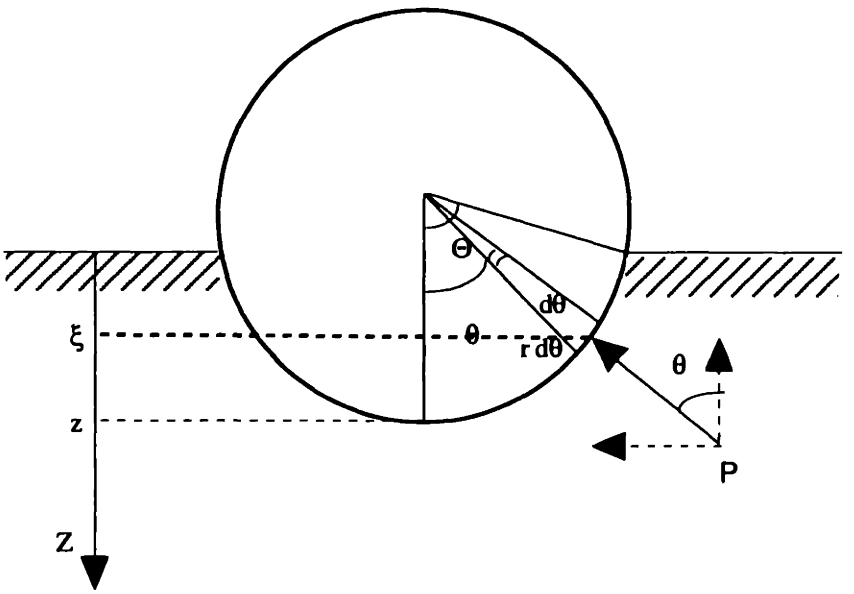

Figure 5.14 Integration of resistive pressure over the contact area between the drop - powder mixture and the dry powder bed.

Using Equations 5.28 to 5.34, Equation 5.27 can be solved numerically for the motion of the evolving drop - powder mixture. In executing this procedure, the incorporation of solid particles into the body of the mixture is stopped when packing density inside the mixture has reached a specified value, e.g. 40%. The computation stops

when the velocity reaches zero, i.e. when the drop - powder mixture has stopped at the bottom of the crater.

5.9 Conclusion

In this chapter, a one-dimensional model is developed for the impact penetration of a droplet into a loosely packed powder bed of the type found in Three Dimensional Printing. This model is based on the experimentally observed fact that the penetration lasts hundreds of microseconds and a primitive ball forms during the process as the liquid-powder particle mixture moves into the powder bed and deforms it to form a crater. By comparing these findings with droplet impact behaviors on rigid surfaces, it becomes clear that the distinctive features of droplet-loose powder bed impact interaction are that the powder bed deforms substantially and the powder particles readily enter the droplet as they encounter. The finding on engulfing of solid particles by a wetting liquid drop is in agreement with experimental results found in other fields such as aerosol science. The quick spreading of a film of wetting liquid on a solid surface as found in drop-solid surface impact studies corroborates the finding in this study. In the course of interpreting these observations, it is found that the surface energy condition is such that the system's energy is minimized when a small alumina particle is engulfed by a larger water droplet; by the inertial effect alone such a solid particle would be quickly overtaken by an advancing droplet. The solid particles are dispersible when immersed in the liquid, so the porous structure of the bed is destructible upon impact. Even if the porous structure stays intact, the calculation based on Washburn equation indicates that the size of the capillaries in the powder bed is such that the capillary flow speed is comparable with the droplet's speed.

Based on these findings and their interpretations, equation of motion of the droplet-particle mixture are developed. The mass and presentation area of the mixture increases as solid particles enter the system. The increase of mass is a major factor causing the deceleration of the mixture. The mixture's momentum decrease due to the external force acting on the solid particles at the boundary of the system. This force is a function of the depth of penetration; the empirical form of the function is obtained through quasi-static penetration test and corrected to take into account the high strain rate of impact deformation. The geometry of the droplet-particle mixture is simplified so that the resistance force can be

integrated over the system's boundary. The simplification is supported by observations on the porous and deformable nature of the powder bed.

CHAPTER 6

IMPACT PENETRATION EXPERIMENT AND SIMULATION

6.1 Introduction

Typically, the impact of a water droplet on a loose alumina powder bed ends up with a ball-shaped particle aggregate sitting on the bottom of a bowl-shaped crater. The depth of penetration, measured from the surface of the powder bed to the bottom of the crater, depends on a series of parameters such as the density, size and initial velocity of the droplet, the density of the powder material, the packing densities inside the powder bed and inside the primitive ball. Also included in the model developed in Chapter 5 is the resistance - penetration characteristics of the powder bed. In the linearized version, this relationship is represented by the ratio of the resistance and the penetration depth. Though in a very simple form, this ratio takes into account many factors which underlie the bed's resistance to deformation but their relationships are very hard to quantify otherwise. For example, the shape of the particles, the spatial relationship between these shaped particles, and the friction and adhesion between individual particles are among such factors.

Impact penetration tests were conducted to experimentally evaluate the influence of these parameters on the impact penetration depth. The focus was to study how the change of droplet impact velocity affects the penetration depth, so impact velocity was chosen to be the main controlled variable. Instruments were developed to assess the powder bed properties. Powder bed conditions such as packing density were allowed to vary naturally and no efforts were rendered to control them to any specific values. Impact penetration depths and crater profiles were measured by optical means.

A numerical simulation program was developed based on the model described in Chapter 5. Experimental conditions recorded in the impact penetration tests were used as input parameters in the simulation. The validity of the model was examined by comparing the penetration depths predicted by the simulation with experimental data.

The validity of the model was further examined by modifying certain aspects of the model and running the simulation under these scenarios. Penetration depth predictions produced from these scenarios were compared with experimental data. The agreement or disagreement between the predictions and experimental data were used to judge the adequacy of the model.

The insight gained through the simulation of single droplet impact is useful to understanding of multiple droplet - powder interaction phenomena observed in Three Dimensional Printing, such as "balling" and "line pairing." Study of single droplet impacts on loose powder beds has helped build a framework for understanding the function and relative importance of many major process parameters in Three Dimensional Printing.

6.2 Experimental Equipment for Studying Impact Penetration Depth

6.2.1 Usage of the Impact Cratering Observation Station

The impact cratering observation station described in Chapter 3 was used in this part of the study, except that, as the focus was shifted to studying the end result of the impact, taking photographs of the impact process itself was no longer the essential part of the study. Taking sequential impact photographs also became less feasible due to the fact that the impact speed was changed several times for each powder sample in order to investigate the effect of impact velocity on penetration depth; the limited size of powder bed would not allow taking many photographs at each impact speed. The main functions needed now from the impact observation station were droplet generation, impact speed measurement, stream adjustment and inspection, and manipulation and monitoring of the powder bed throughout the experiment. The camera and strobe light were important visual inspection tools in these operations, as explained in Chapter 3; so these two devices still found usage is this experiment.

6.2.2 Station for Powder Bed Characterization

The powder samples are distinguished by
(1) the material species,
(2) the powder particles' shape, size and size distribution,
(3) the packing density of the powder bed, and
(4) the penetration - resistive pressure curves.

The last two properties of the powder bed were measured at the Station for Powder Bed Characterization. The packing density was obtained by weighting the powder sample contained in a powder box of known volume and weight, calculating the apparent density of the powder bed and dividing it by the material density of the powder. The weighing of the powder sample was done on an electronic balance which was also the force sensing component of the penetrometer described below.

The principle of the quasi-static penetration test and its usage in the model of penetration depth were described in Chapter 5. The penetration - resistive curves were produced by pushing a flat-ended pin of known diameter into the powder sample and measuring the displacement and resistance force simultaneously. The apparatus used here accomplished three functions: (1) driving the penetrating pin and measuring its displacement, (2) sensing the resistive force, and (3) logging the data. Components performing these functions are described separately in the following sections. The whole set-up is illustrated in Figure 6.1.

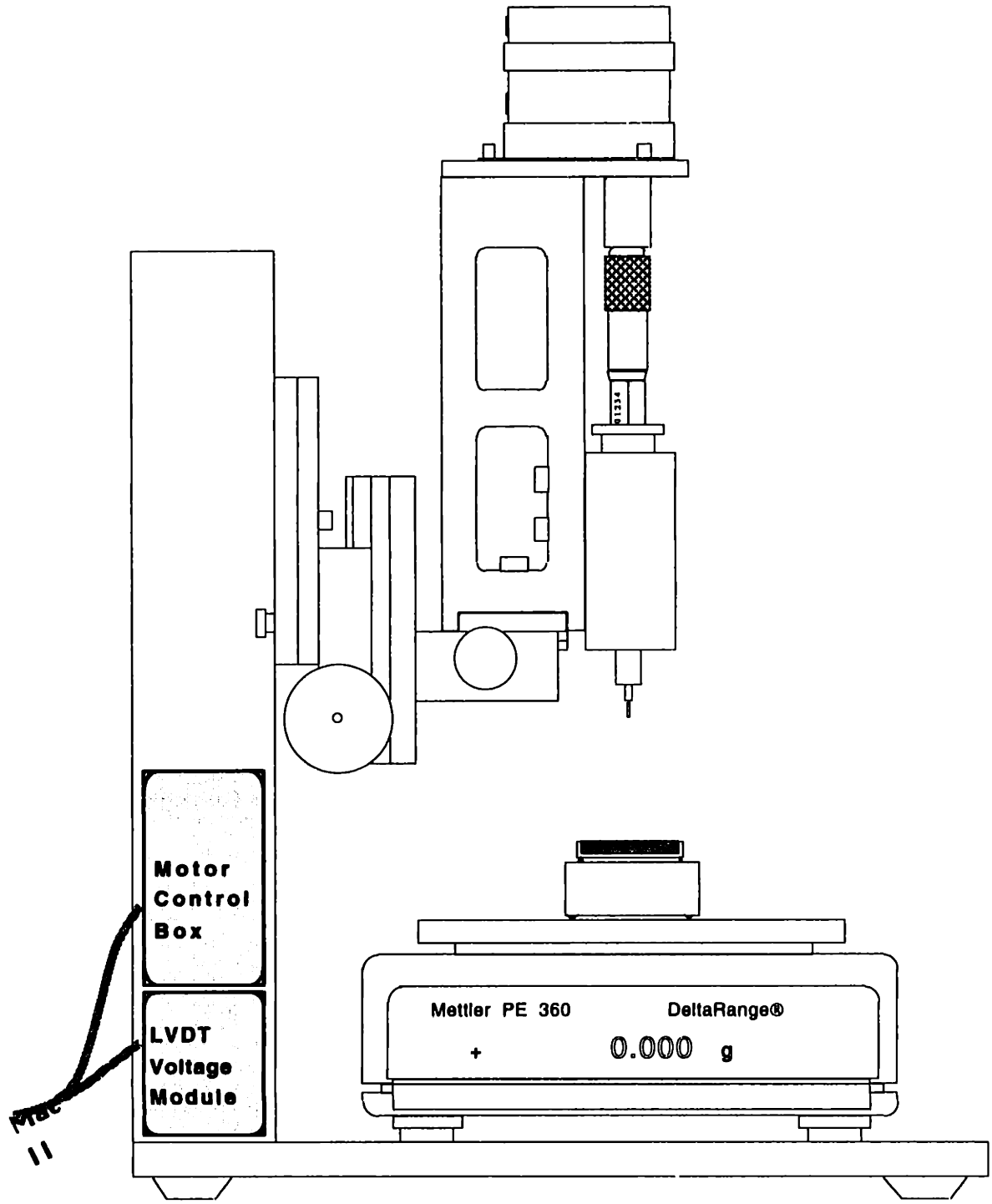

Figure 6.1 Station for Powder Bed Characterization

6.2.2.1 Penetrometer

The penetrating pin was driven by a reversible hysteresis synchronous motor, Model CA 990275, made by Hurst, with a rotational speed of 2 rpm. Two Crydom CX240D5R solid state relays were used to switch the direction of the motor rotation. The rotational motion was converted to translation by a micrometer head with non-rotating spindle, Model 262L by the L.S. Starrett Company, coupled to the motor axle through a slideable coupler. This arrangement assured uniform, smooth and non-rotational movement of the penetrating pin.

The micrometer spindle moves 635 microns per revolution and motor speed is 2 rpm. So the pin penetrates at a speed of 21.1 μm/sec. At this speed, 50 force-depth data point can be produced over a penetration range of 200 μm with a force sensing element described in the next section. This slow penetration is considered quasi-static. The micrometer head also served as an calibration tool for the LVDT.

An LVDT, model Schaevitz™ 025-MHR, made by Lucas Control Systems Products, was used for measuring the displacement of the penetrating pin. The core of the LVDT was attached to the lower end of the micrometer's non-rotational spindle through the core's upper extension rod, and the lower extension rod of the core had a pin of 1.0668 mm (42 mils) diameter fixed to the rod's other end. A LVM-110 LVDT Voltage Module, also made by Lucas, was used as the LVDT signal conditioner board. The LVDT unit was calibrated to produce a 5 mv DC voltage output for every micrometer of displacement.

The penetrometer was mounted on two linear translation stages to allow adjustment of the penetrometer position in the z (height) and x (lateral) directions relative to the powder sample. The powder sample box sat on top of the force sensing element, which is described in the next section.

6.2.2.2 Force Sensing Element

In order to assess the resistance force from the powder bed to the penetrating particle aggregate produced from a single droplet, the probing pin is desired to be of a size similar to the aggregate. On the other hand, the resistance force in a loose powder bed on a

thin pin of such a size is extremely small. A powder bed's resistance to quasi-static penetration can be estimated from its capacity of bearing a dead weight. Typically, at a pressure of 3000 Pa a dead weight would sink to a depth of about 1 mm in the loose powder beds of alumina powder. The force is about 2.4 microgram on an area of 100 μm diameter. At shallower depth the force would be proportionally smaller. So a practical lower limit of the pin size is set by the sensitivity of the force sensing component. Since the force sensing component available to this study has a sensitivity of milligram, a pin of larger diameter is used.

As the powder bed exerts a resistive force on a slowly penetrating pin, a force of the same amount in the opposite direction is applied on the powder bed by the pin. This force can be measured by a balance placed underneath the powder bed. This arrangement made it possible to use an available Mettler PE 360 DeltaRange®, which has a resolution of one milligram, and simplified the instrumentation of force sensing. Re-zeroing the balance with the powder sample on it would allow a direct reading of the penetration resistance.

Through preliminary testing, the pin size of 1.0668 mm (42 mils) diameter was determined adequate to produce large enough force signals on most of the tested powder beds using this balance. The possibility of pin size affecting the penetration characteristics of the powder bed was also investigated and will be discussed in a later section.

A RS232C data interfacing board, Mettler 016 Data Output Option, output the force readings to a computer for data logging. In continuous sending mode, this board has a maximum data updating rate of 5 times per second. This limited data sampling rate of the balance was the main reason the slow penetration speed, as discussed previously, was chosen.

6.2.2.3 Apparatus Control and Data Logging

The motor control, the data conversion and logging are executed by a LabView program on a MacII computer through a LB-NB board made by National Instrument. After the program starts, it turns on the motor, which moves the pin downward into the powder bed while the penetration data is read five times per second, or every four micrometer increment of penetration. The penetration curve is displayed on the computer screen for

monitoring as the penetration progresses, and the data is stored onto the hard disk as an Excel spreadsheet file after the specified penetration depth is reached. At this point the program reverses the motor's direction of rotation and raises the pin until the pin reaches its upper parking position.

Each penetration test began with manually re-zeroing the balance and aligning the pin's penetration surface with the powder bed surface. The alignment was done with monitoring through a microscope trained horizontally on the contact point. Before the penetration pin was put into use, precaution was taken to ensure the cleanliness of the pin.

6.3 Experimental Procedures

6.3.1 Droplet Impact Tests

The powder samples were prepared following the procedures described in Chapter 3. Powders used in the penetration depth experiments are listed in Table 6.1. The alumina powders are the same as in the cratering impact observation tests described in Chapter 3.

Table 6.1 Powders used in impact penetration depth experiments

Name	Shape	Size	Manufacturer
Electronic Grade Alumina	Flakes	25 μm	Norton, MA
Alunabeads®	Sphere	10 μm	ICD
316L Stainless Steel	Sphere	5 μm	UltraFine

Besides packing density measurement, each powder sample was subjected to quasi-static penetration tests using the penetrometer described in the last section. In recognition of the possible variation of local packing density, three penetrometer tests were conducted on three sites distributed along the central line of the powder box, one for each site (Figure 6.2). The sites were separated from each other by a distance of 10 mm. The penetration resistance - depth curves were fitted to linear or power functions to obtain the stiffness modulus of the powder bed.

The impact cratering observation station was prepared and operated according to the procedures described in Chapter 3. The focus of the experiment was to observe, with given powder bed conditions as well as droplet size, how droplet impact velocity affects the penetration depth of the primitive ball formed by a single droplet. The impact velocity of the droplet was changed by moving the printhead up and down relative to the powder sample. At flow rates around one milliliter per minute, the available range of height adjustment made it possible to vary the impact velocity from 3.5 m/sec to 9 m/sec. Flow rate needs to be increased to obtain impact speeds at a higher range. Four impact speed levels were used on each powder sample.

Each powder sample was divided into three regions, centered around the three penetrometer testing sites, as illustrated by Figure 6.2. The powder bed strength of resisting penetration in each region was represented by the penetrometer test curve obtained at the test site in that region. Each region is further divided into two subdivisions, separated along the center line of the sample box. In each of the six subdivisions four drops at four different initial impact speeds were released. Thus at each impact speed level two impact cratering samples were obtained in each of the three regions. Impact velocity was measured individually for each droplet using the SpeedTrap described in Chapter 3.

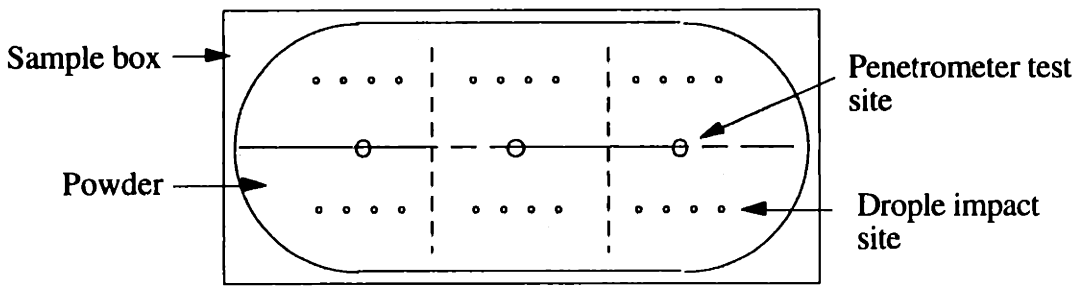

Figure 6.2 Four levels of impact speeds were repeated at each of the six subdivisions demarcated by the three penetrometer testing sites (denoted by o) and box center line.

6.3.2 Measuring the Crater Geometry

The crater geometry was measured after the impact test using the "depth of field" method with an Olympus OHM microscope. The objective used was 20x, N.A. = 0.4. The stage of the microscope has a dial indicator for the vertical height, representing of 2 μm

change per division. Each division on the eyepiece reticle, when the 20x objective is in use, corresponds to 5 μm.

Each crater was profiled by measuring the diameter of the crater wall at different depths. The first step was to establish the position of the original powder bed's surface. Since the crater rim might have been elevated due to the impact, the z = 0 position was determined at surface areas away from the impact site. Then the microscope stage was raised in 10 - 20 μm steps, and the crater wall dimension at each cross section was measured with the eyepiece reticle to ± 2 μm. The primitive ball was noted for the positions of its top and the middle, as well as its diameter.

6.4 Results of Penetrometer Tests

6.4.1 Representation of the Quasi-static Penetration Data

Figure 6.3 shows a resistive pressure - depth curve obtained from a sample of the 25 μm flaky alumina powder. The maximum penetration depth in this test was 400 μm. This curve can be approximated by a power function

$$q = 5.38e5 \cdot z^{0.9} \text{ (Pa)}$$

which has a correlation coefficient r = 0.9802. The data points can also be fitted to a linear function

$$q = 1.17e6\ z \text{ (Pa)}$$

with a slightly lower correlation coefficient, r = 0.9729.

The penetration depths of the primitive balls, by experimental observation, are normally less than 200 μm. It is sensible to examine the penetrometer test data more closely within this range. Figure 6.4 is an exploded view of the data up to the depth of 200 μm. Table 6.2 summarizes the results from fitting the data with linear and power function. It suggests that both functions can represent the data well.

Table 6.2 Approximation equations for a quasi-static penetration curve in the shallow range ($z \leq 200$ μm)

Approximation Equations	Correlation Coefficient
$q = 1.29e6 \cdot z$	r = 0.9630
$q = 5.54e5 \cdot z^{0.908}$	r = 0.9614

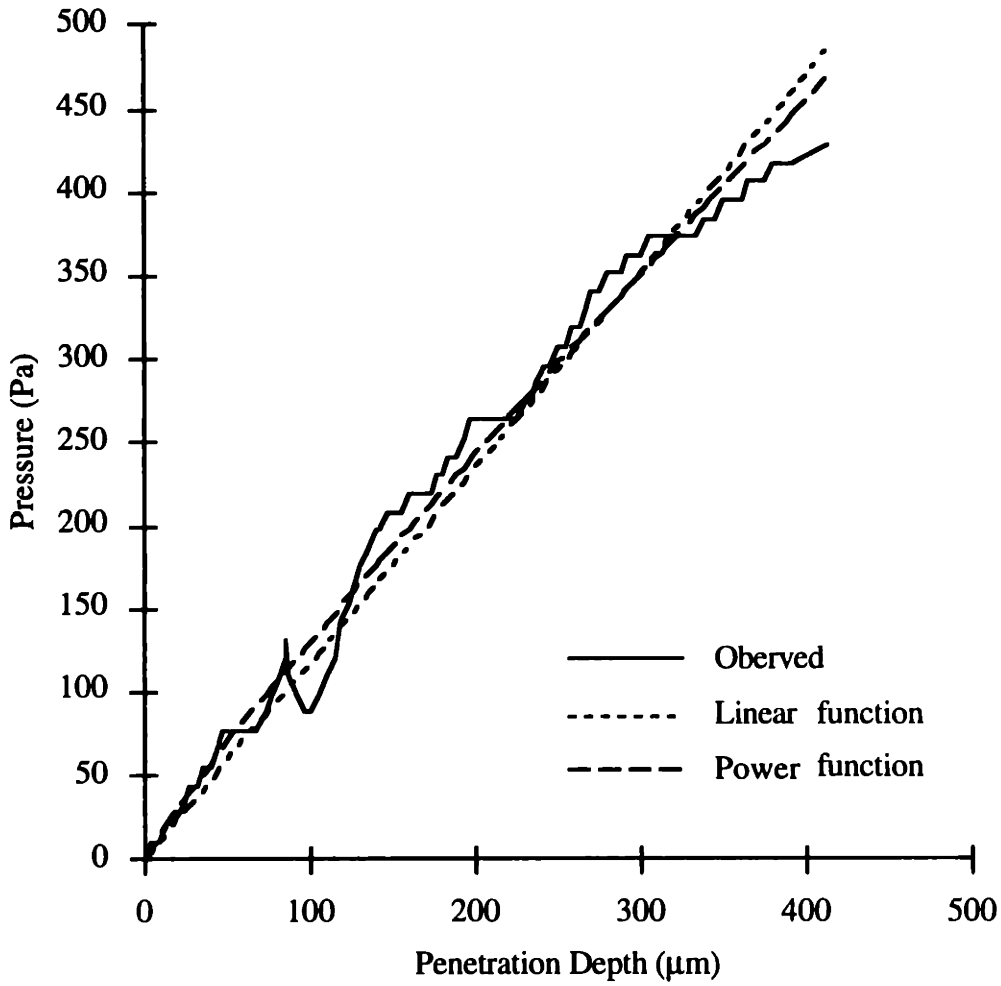

Figure 6.3 Quasi-static Penetration Curve (25 μm flaky alumina powder).

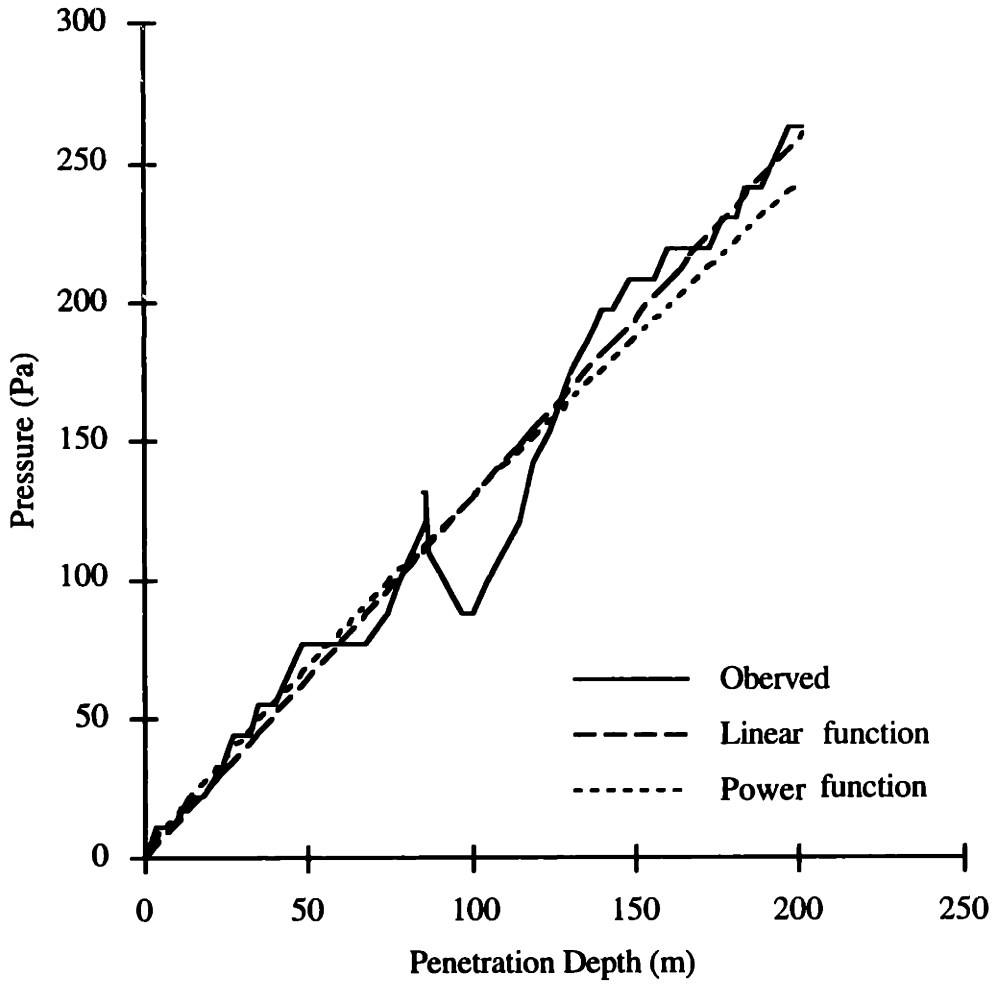

Figure 6.4 Approximation of penetration data for depth less than 200 μm with linear and power functions.

The purpose of the data fitting in relation to the model of impact penetration depth is to represent the pressure - penetration depth in a functional form, so that this relationship can be conveniently used in computations. While both a power and a linear function can represent the penetration curve well, the linear function is simpler. Using the linear form, the integration of the resistive pressure over the interface of the drop - powder mixture and dry powder bed yields a closed form solution of the penetration resistance force (Equations 5.33, 5.34. The derivation is given in Appendix III). Using the power function, the resistance force needs to be evaluated through numerical integration. From a computational point of view, the linear form is preferred for its efficiency.

On the other hand, if the penetrometer data deviates greatly from a linear relationship within the relevant penetration range, then non-linearity should be taken into account in the modeling computation. The approach can either be adopting the power function representation and integrating the resistance force numerically, or approximating the penetrometer penetration curve by two intercepting straight lines, as suggested in Chapter 5.

6.4.2 An Observation on the Relationship Between Powder Geometry and Packing Density in Quasi-static Penetration Behavior

It was shown in the last section that the quasi-static penetration curves can be well represented by a linear function between the resistive pressure and the penetration depth.

$$q = k\,z \qquad (6.1)$$

Figure 6.5 shows the value of k extracted from penetrometer test data for alumina powder beds of different packing densities and particle shapes.

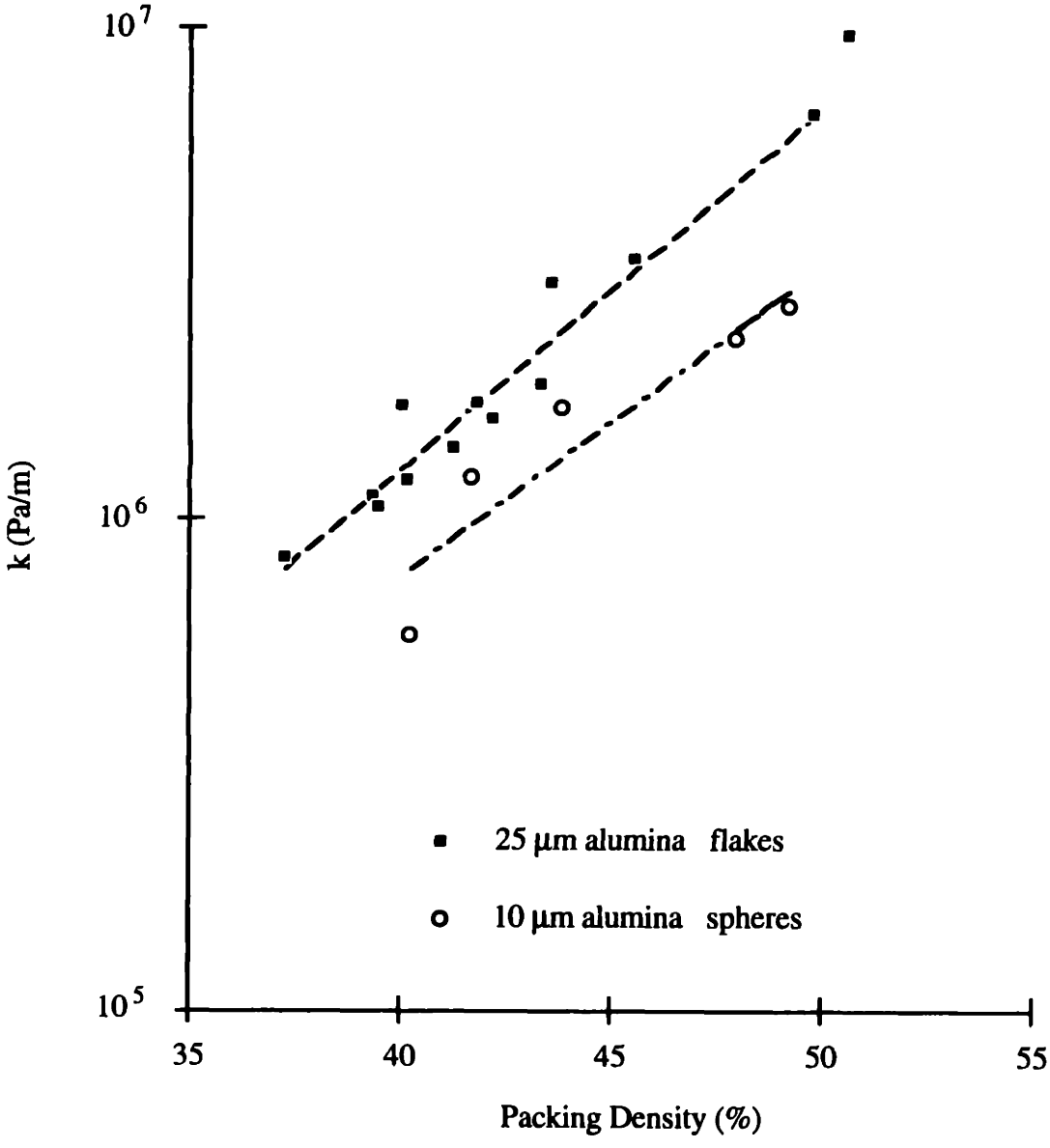

Figure 6.5 Slopes (k) of q - z curves vs. packing density

It is clear from Figure 6.5 that the k value for 25 μm flaky alumina powder increases with the packing density. This means that the resistance force increases faster with depth in denser powder beds. The k values are plotted in log scale, so that penetration resistance is sensitive to the packing density of the powder bed. These observations also apply to the data collected from samples of 10 μm spherical powder. So k value reflects the influence of packing density on powder bed's capacity of resisting deformation.

Figure 6.5 also shows that k value is affected by the shape of powder particles. If linear regression lines are plotted for data from both 25 μm flaky alumina powder beds and 10 μm spherical alumina powder beds, the line for the spherical powder lies below the line for flaky powder. This suggests that if the packing densities are the same, the spherical powder beds offers less resistance to a penetrating body. This is consistent with the fact that, comparing with flaky powder particles, spherical powder particles flow much easily.

Packing density and particle shape are not the only factors affecting k. Other factors, such as chemical composition of the power material , adhesion between particles, and the size of particles also affect k. The mechanisms of their effects on k are complicated. These factors may take effect directly. For example, strong adhesion between particles may increase resistance of the powder particle networks to an intruding body. Their effects may be indirect and act through other factors. For example, stronger adhesive forces between particles may cause the powder bed prepared by roller spreading/leveling to have a lower packing density. And, these factors may also interact between themselves, enhancing or canceling each other in their influence on the powder bed's resistance to penetration deformation.

The observations stated above indicate that k values, or the quasi-static penetration characteristic, is a comprehensive index of deformation behavior of a powder bed. A k value reflects the joint, combined effects of many chemical, mechanical and geometrical properties of the powder particles and the powder bed, as well as the way the powder bed is prepared and the history of the powder bed. It would take tremendous efforts to untangle these relationships. In contrast, a quasi-static penetration test is an a reliable and efficient way to assess a powder bed's behavior under penetration.

6.5 Experimental/Simulated Results of the Effect of Droplet Impact Velocity on Penetration Depth

Figures 6.6, 6.7, and 6.8 show the penetration depths measurements of water droplets with 80 μm diameter on 25 μm flaky alumina powder. The average packing density was 44.2%. The impact velocities were in the range of 3.7 - 9 m/sec. In all cases the penetration depths increases with initial impact velocity. The slope obtained by regressing the penetration depth on the impact velocity is significantly different from zero; the correlation coefficients between the penetration depth and impact velocity are from 0.89 to 0.96. Table 6.3 summarizes results of statistical analysis on the data.

Table 6.3 Statistical Analysis of Impact Penetration Depth - Impact Velocity Data (25 μm Flaky Alumina Powder)

Data	Estimation of Slope, β	S.E.(β)	p - value for H_0: $\beta = 0$	Correlation Coefficient
Figure 6.6	11.912	1.508	0.0005	0.962
Figure 6.7	13.356	2.686	0.0042	0.912
Figure 6.8	13.335	2.992	0.0042	0.894

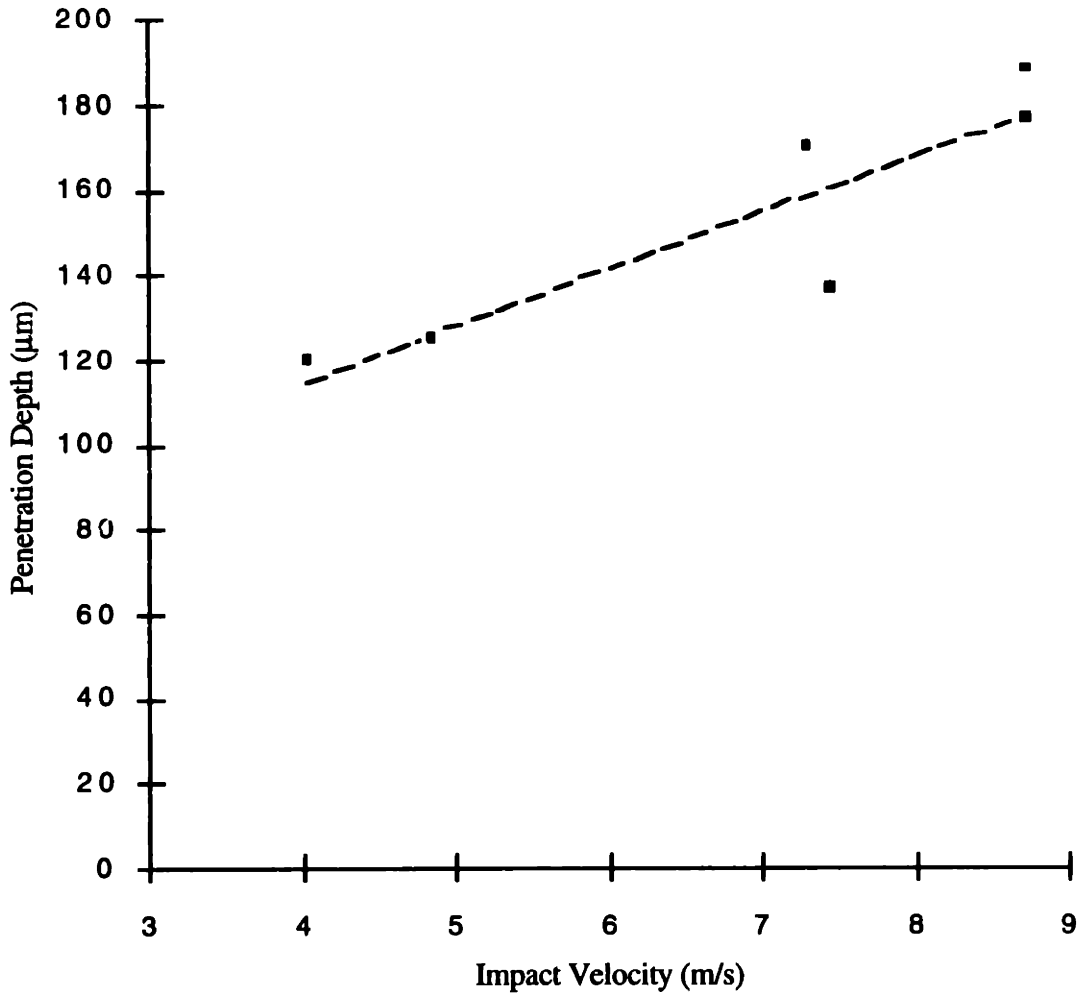

Figure 6.6 Measured impact penetration depth vs. the impact velocity (25 μm flaky alumina powder, k = 2.53 MPa/m).

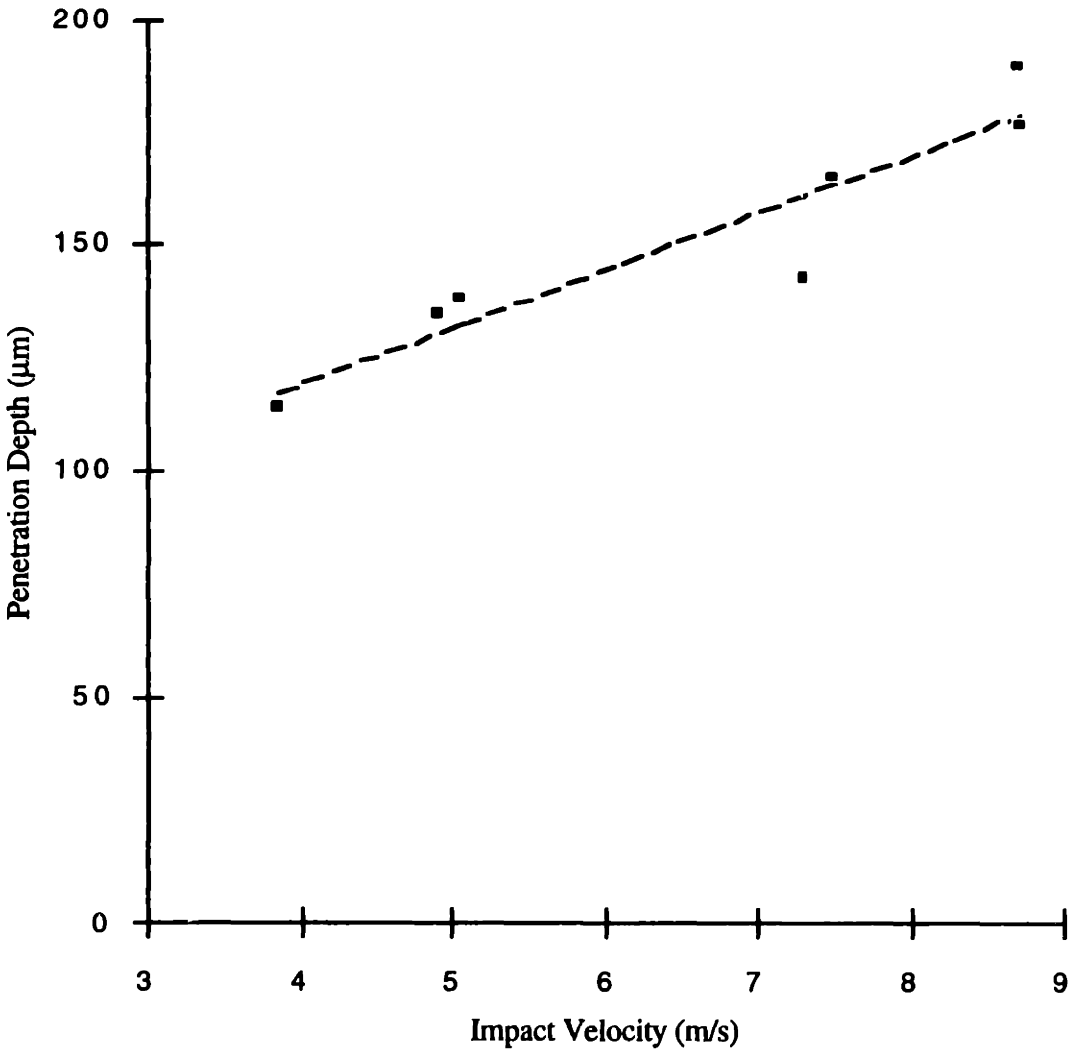

Figure 6.7 Measured impact penetration depth vs. the impact velocity (25 μm flaky alumina powder, k = 1.68 MPa/m).

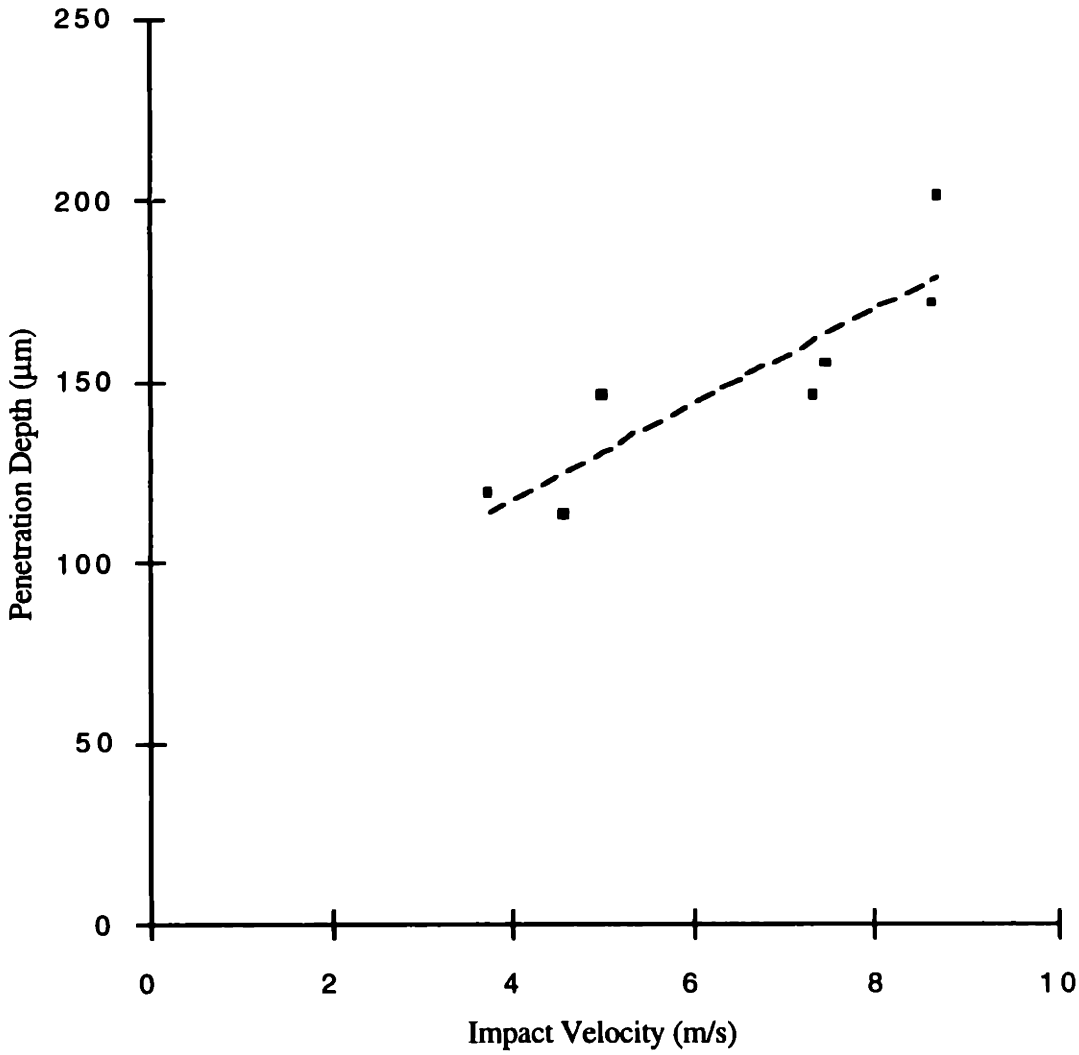

Figure 6.8 Measured impact penetration depth vs. the impact velocity (25 μm flaky alumina powder, k = 3.95 MPa/m).

Figures 6.9, 6.10 and 6.11 show the penetration depths predicted by the model. In running the simulation program, experimental conditions recorded in the impact penetration tests on 25 μm flaky alumina powder were used. The dynamic penetration stress assumed in the simulation was

$$q_d = q. \tag{6.2}$$

As seen in Figures 6.9, 6.10, and 6.11, the prediction curve parallels the experimental data in all the cases, which indicates that the model performs well in describing how the penetration depth changes with the impact velocity, except by a constant offset. The predicted penetration depths exceed the measured crater depths by 20 - 40 micrometers, and this overestimation is consistent in all the three cases. Both of the parallelism and the offset are important facts. If the predicted curves have slopes largely different from the experimentally evaluated penetration depth - impact velocity relationship, the model might have incorrectly represented the relationship between the two, or left out certain factors which were sensitive to the impact velocity variation in the investigated range. The parallelism indicates that is not the case.

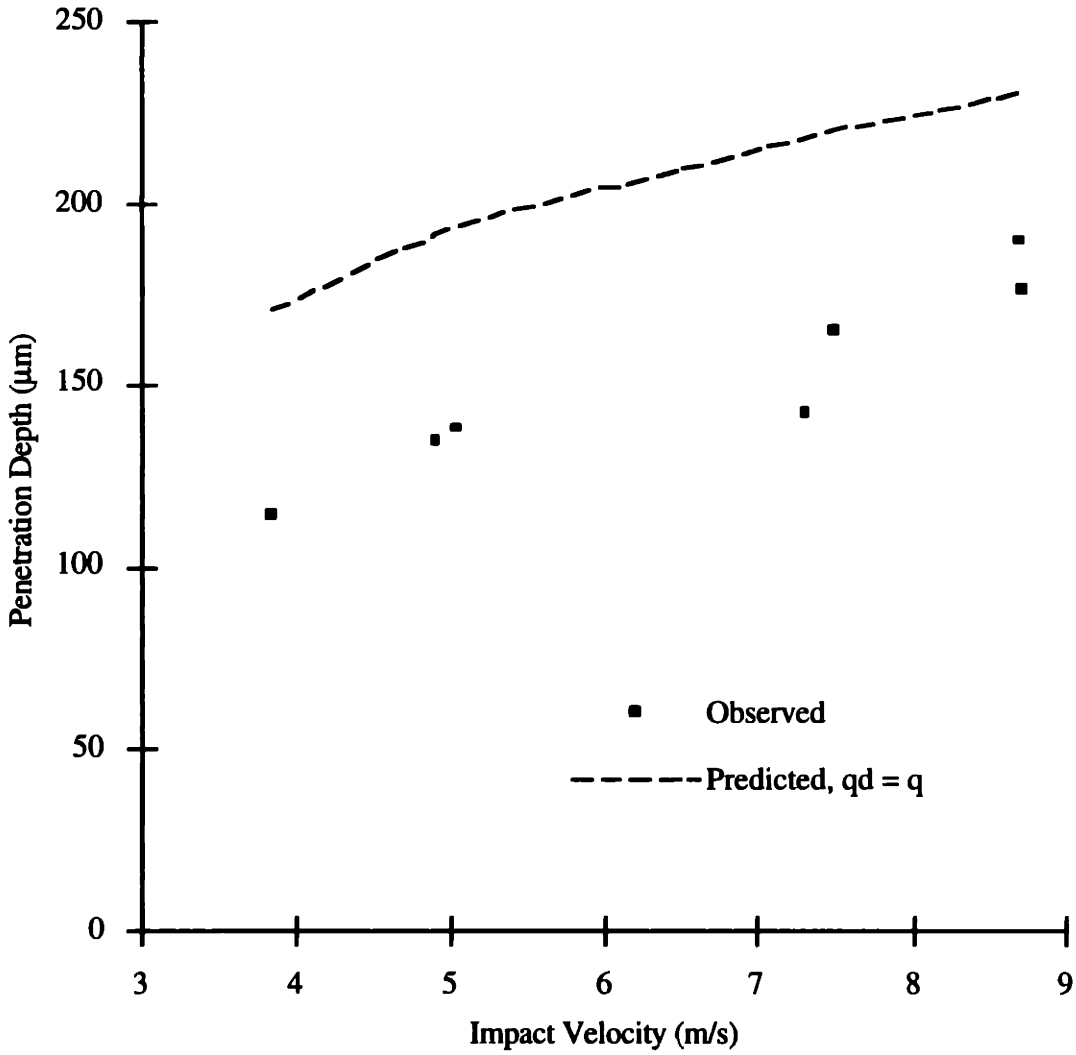

Figure 6.9 Impact penetration depth (predicted & measured) vs. the impact velocity (25 μm flaky alumina powder, k = 1.68 MPa/m).
q_d = q was used in the prediction.

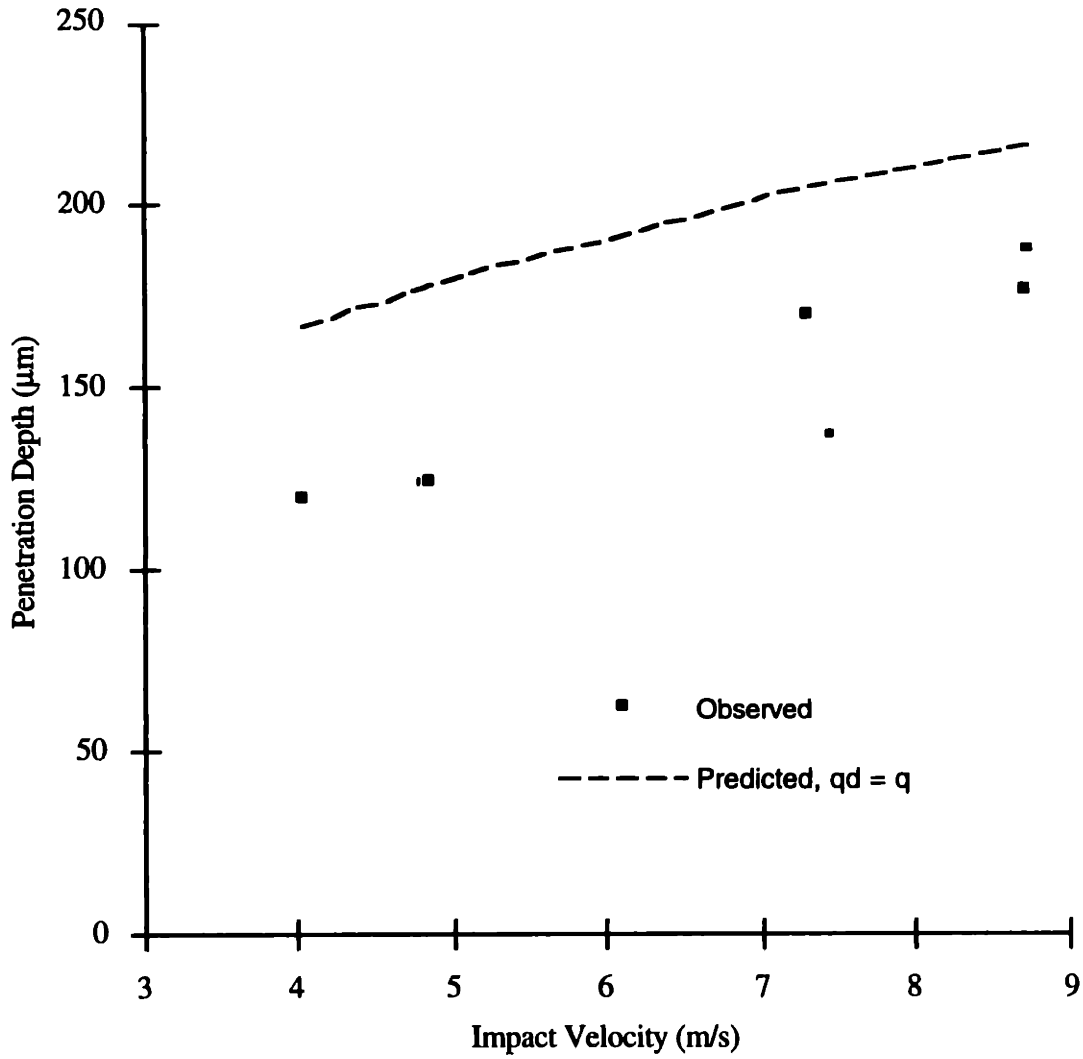

Figure 6.10 Impact penetration depth (predicted & measured) vs. the impact velocity (25 μm flaky alumina powder, k = 2.53 MPa/m).
q_d = q was used in the prediction.

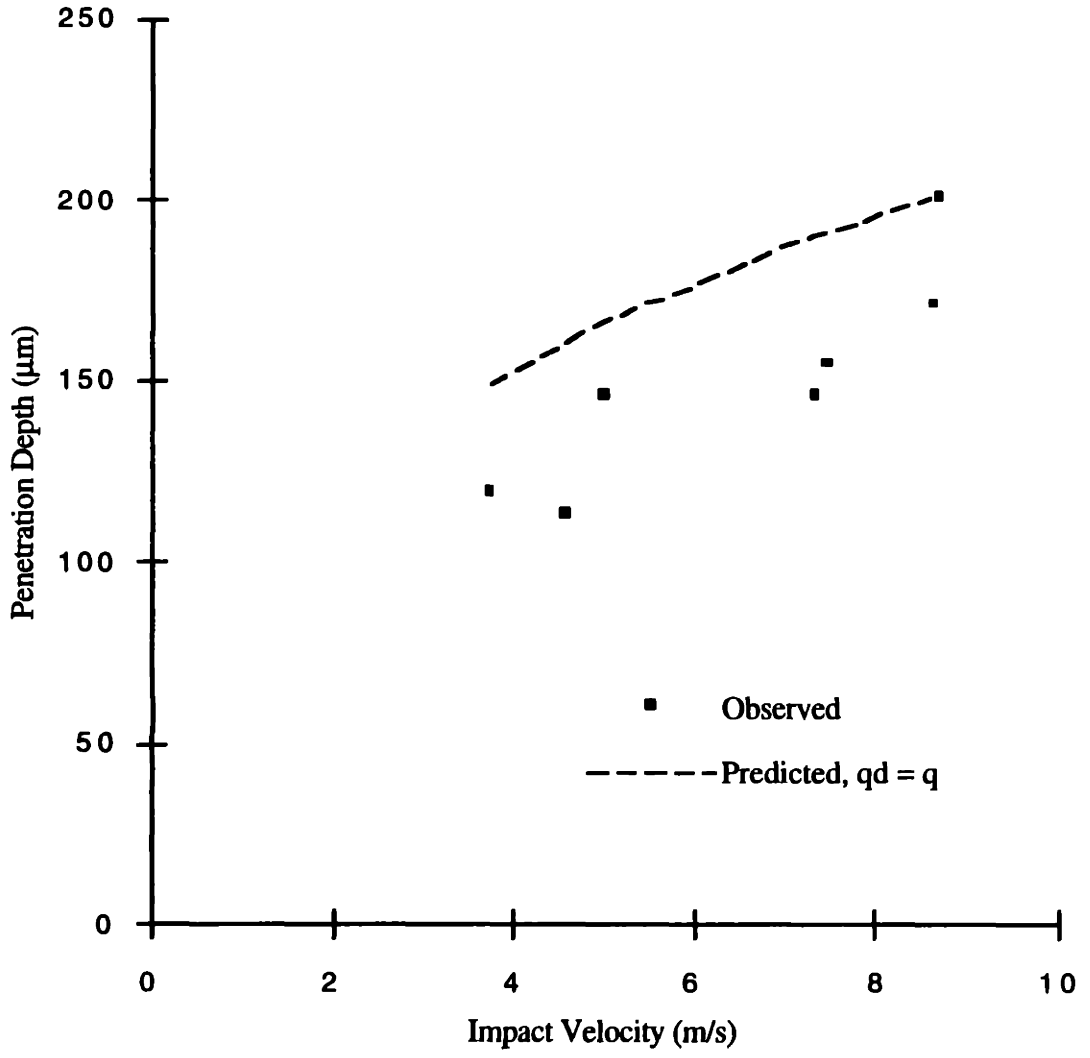

Figure 6.11 Impact penetration depth (predicted & measured) vs. the impact velocity (25 μm flaky alumina powder, k = 3.95 MPa/m).
q_d = q was used in the prediction.

On the other hand, the offset indicates that certain factors should be scrutinized to account for the overestimate. Two factors had been included in the model to account for the deceleration of the drop-powder mixture as it penetrates into the powder bed. One factor was the inertial term in the equation of motion, Equation 5.27. Later in this chapter it will be shown that the inertial effect has been adequately described by this inertial term. The other factor causing the drop - powder mixture to decelerate was the powder bed resistance to deformation. It appears that the powder bed resistance to penetration was underestimated by using Equation 6.2, where it was assumed that the powder bed resistance to a fast penetrating body was the same as its resistance to a quasi-static penetration.

As was discussed in Chapter 5, most materials exhibit higher strength in dynamic loading than in static loading. In impact penetration studies the dynamic strength of metals are often estimated as 3 - 4 times of the values obtained from static tests. Powder materials have dynamic stress proportional to the logarithm of the strain rate (Equation 5.22). The droplet impact speeds were a few meters per second, and the speed in penetrometer tests was 20 μm per second. Since the penetration speed in the two situations differs by 5 - 6 times in logarithmic scale, strain-rate effect should be expected. Equation 5.23 suggested to estimate the dynamic penetration resistance by

$$q_d = k' q, \qquad (6.3)$$

where $k' > 1$.

The value of k' can be estimated empirically by using different k' in the simulation program and comparing the penetration depth predicted by the model with the experimentally measured crater depth. For the data in Figure 6.9 this was done at one of the impact velocities, V_o = 3.84 m/sec. It was found that at this velocity, k' should be about 6. This k' (= 5.95) was used in the simulation program to predict the impact penetration depth at other velocities represented in Figure 6.9. The new predictions are shown in Figure 6.12. The observed data points distributed evenly around the prediction line, indicating that the errors are random. These may be attributed to local variation of powder bed strength and measurement error.

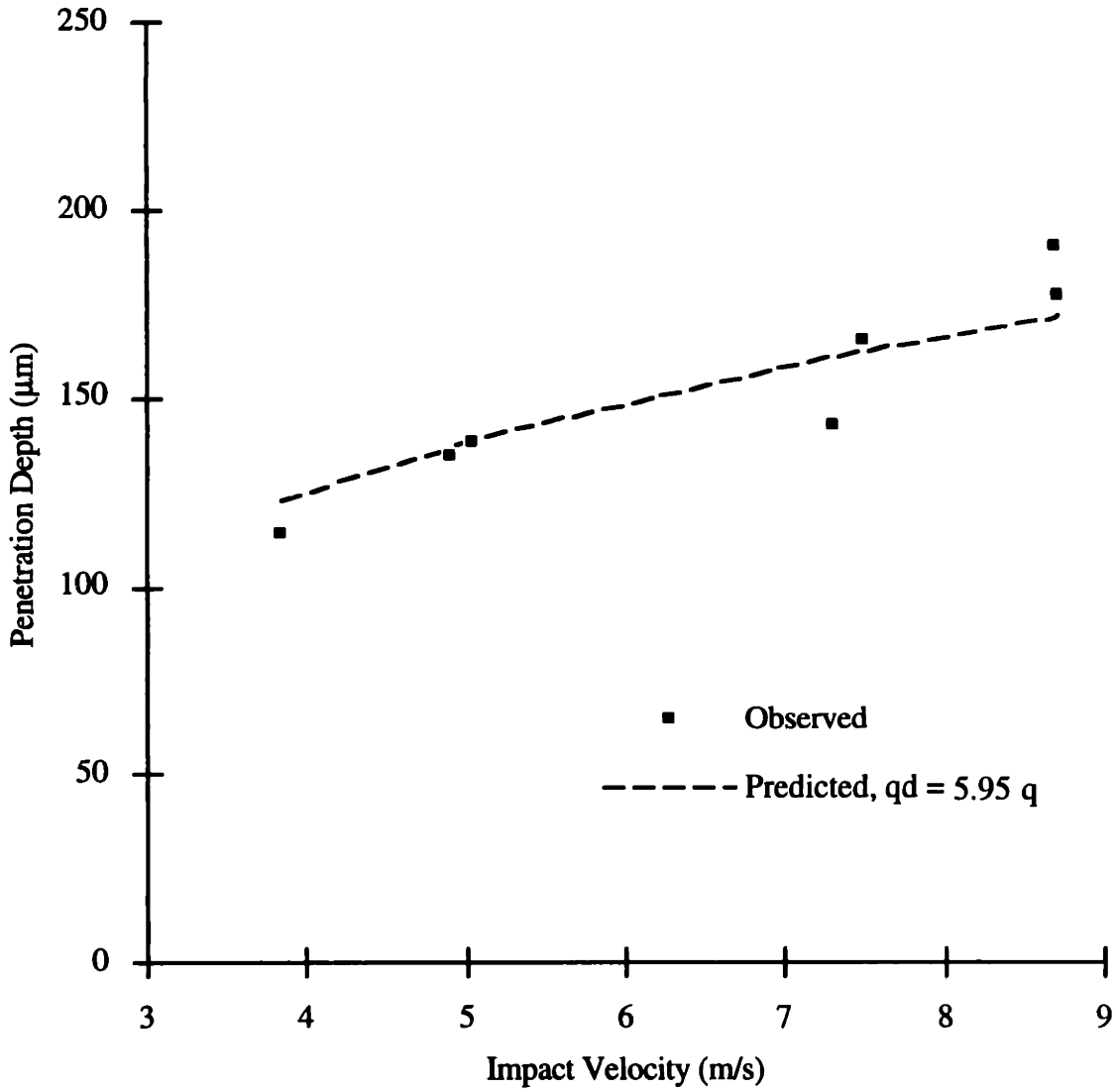

Figure 6.12 Impact penetration depth (predicted & measured) vs. the impact velocity (25 μm flaky alumina powder, k = 1.68 MPa/m).
q_d = 5.95 q was used in the prediction.

The same k' was used as a dynamic stress scaling factor in the simulation program to re-predict the impact penetration depths for the other two cases presented previously in Figures 6.10 and 6.11. The results are shown in Figures 6.13 and 6.14.

In Figure 6.12, the observed data points distributed evenly on both sides of prediction curve. However, the predictions in Figure 6.14 appears to have underestimated the penetration depth consistently by about 20 μm. Considering the particle's nominal size of 25 μm, 20 μm is not a large error. However, since the underestimate is systematic at all the data points, a dynamic stress scaling factor less than 5.95 might be more appropriate for this sample.

By trial at one impact velocity, V_o = 3.74 m/sec., k' was found to be 2.78. Estimating the dynamic stress by this value, the penetration depth at other velocities were predicted. The results are shown in Figure 6.15. The observed data points are now evenly distributed on both sides of the prediction curve, indicating a more accurate prediction.

The reason k' differs in the three cases may be attributed to the differences in the parameter k of the quasi-static penetration curve. The sample presented in Figure 6.15 had the largest k value compared with the other two, indicating this sample is stiffer. The powder particles in a more rigid powder bed would move less when acted on by an intruding body, so their strain-rate effects would thus be reduced.

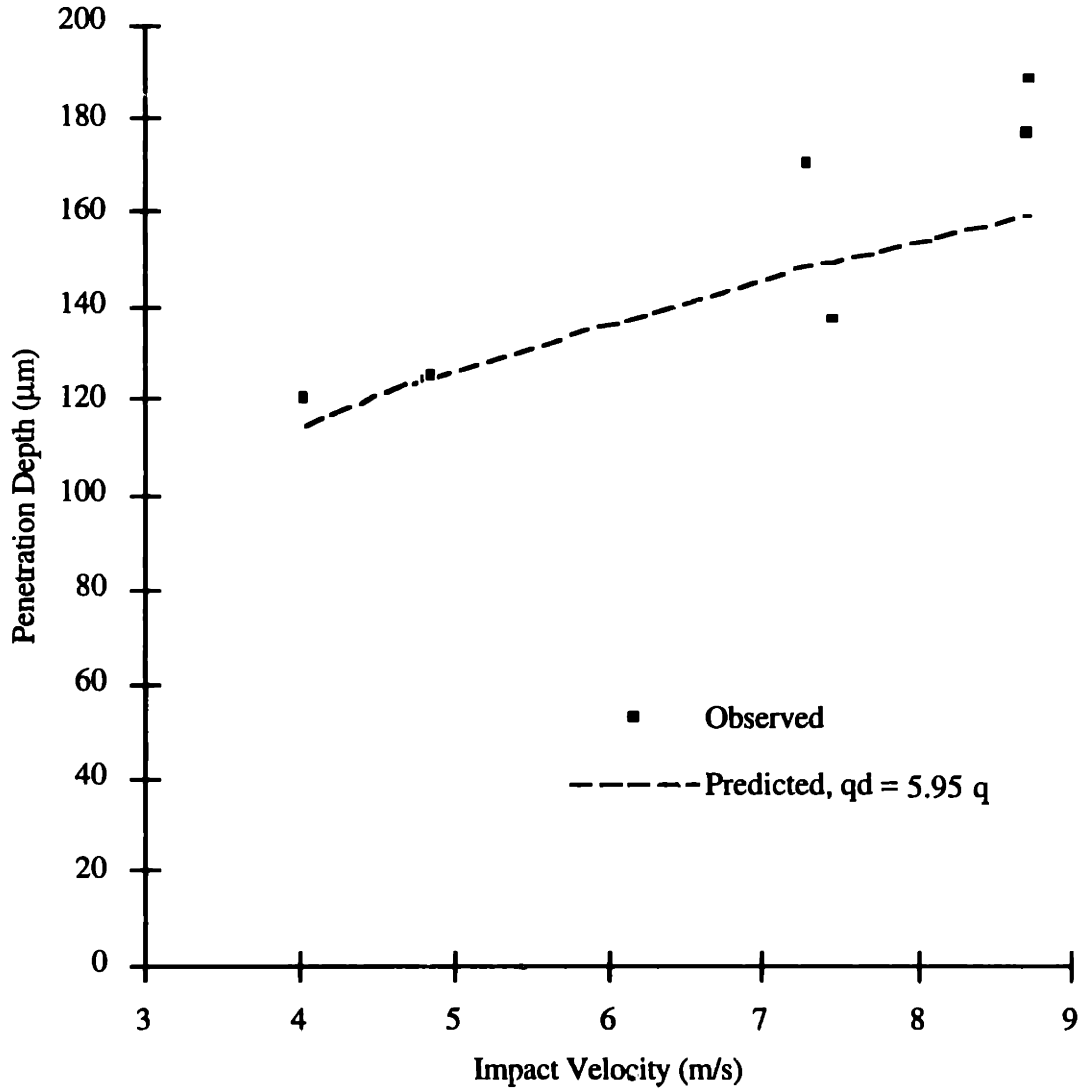

Figure 6.13 Impact penetration depth (predicted & measured) vs. the impact velocity (25 μm flaky alumina powder, k = 2.53 MPa/m).
q_d = 5.95 q was used in the prediction.

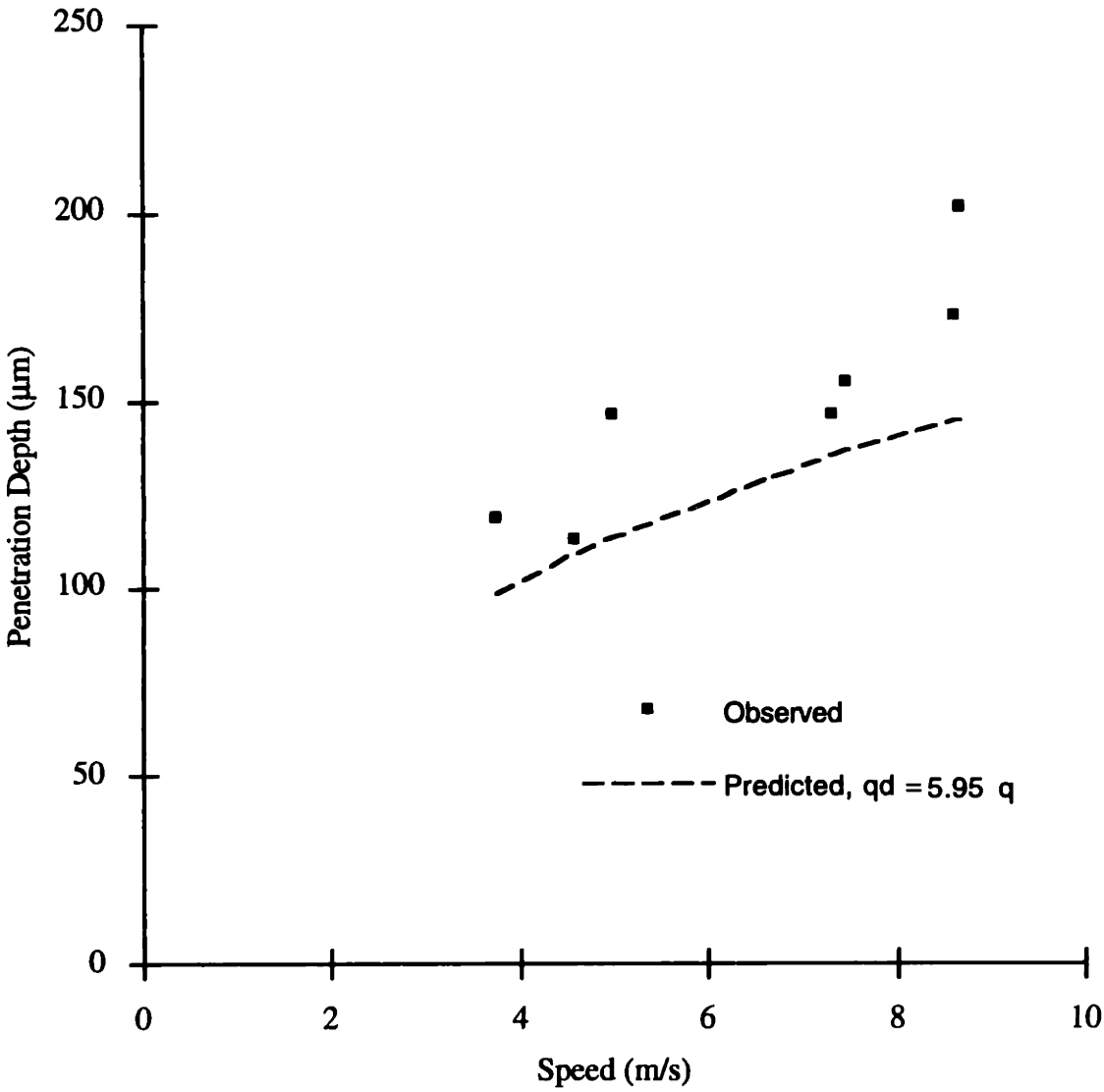

Figure 6.14 Impact penetration depth (predicted & measured) vs. the impact velocity (25 μm flaky alumina powder, k = 3.95 MPa/m).
q_d = 5.95 q was used in the prediction.

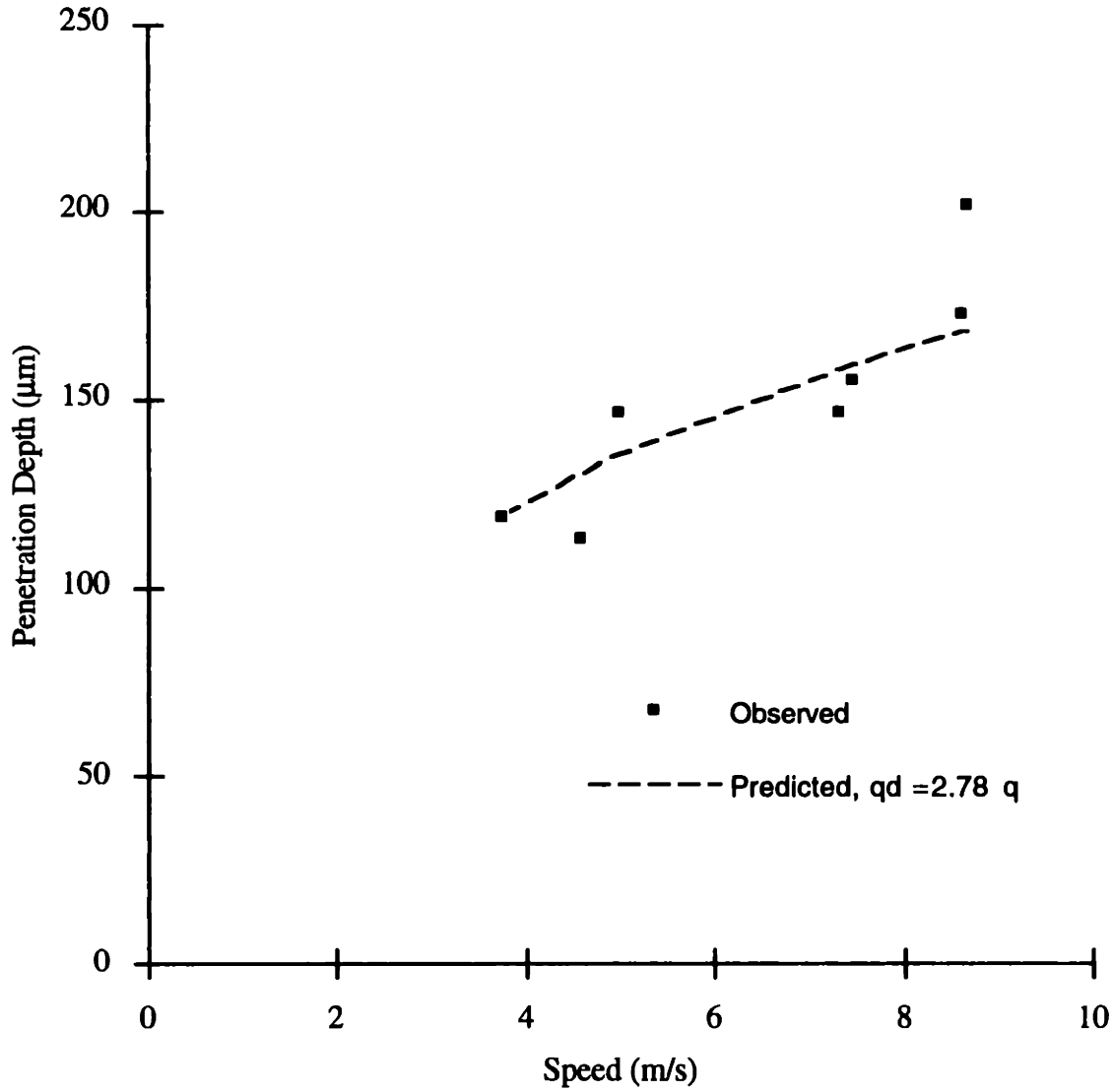

Figure 6.15 Impact penetration depth (predicted & observed) vs. the impact velocity (25 μm flaky alumina powder, k = 3.95 MPa/m).
q_d = 2.78 q was used in the prediction.

If the above observation is correct, then we can make the following postulation: For a powder bed that is more deformable, the dynamic stress scaling factor tends to be larger. The beds of the 10 μm spherical alumina powder falls into this category. Its behavior provides supporting evidence.

Figure 6.16 shows the results of impact experiment on the 10 μm spherical alumina powder. The dashed line in figure 6.16 represents the penetration depth prediction using a dynamic stress equal to the quasi-static penetration stress. The prediction overestimated the penetration depths by 70 μm, larger than those in the 25 μm alumina powder. Since the 10 μm spherical alumina powder is much easier to flow, this result appears to support the above postulation.

At the impact velocity, V_o = 10.5 m/sec, the k′ was re-estimated to be 7.6 for the 10 μm spherical alumina powder. This value was used to account for the dynamic stress to predict the penetration depths for other impact velocities. The new prediction is shown in Figure 6.16 (the solid line). It appears that k' = 7.6 estimated the dynamic stress well, so the predicted penetration depths are in fine agreement with the measurements.

Compared with the two kinds of powder bed of alumina powders, powder beds of the 5 μm stainless steel spheres are on the extreme stiff side of the strength spectrum. Not only its material density is almost two times higher than alumina, the sub-micron sized components in its content make the powder highly cohesive and can hardly flow. Consequently, the powder bed prepared with this powder has a very stiff characteristic penetration curve, exhibiting a high stiff modulus k (circa 400 MPa/m) in the initial linear range of the quasi-static penetration curve. On these beds, droplets with initial impact speed less than 10 m/sec barely created observable craters. In this type of situation, the impact penetration by droplets in the experimental range should cause much less strain-rate effect. At impact speed of 12 m/sec, the crater depth was on average 79 μm. The penetration depth was computed using the simulation program with a k' = 1, yielding a result of 82 μm. Because the limited range of impact speed in the experiment, 12 m/s was the highest impact speed obtained and the crater depths were measured at this single level. The method of "evaluating k' at one speed level and applying it to other speed levels" could not be exercised in this case.

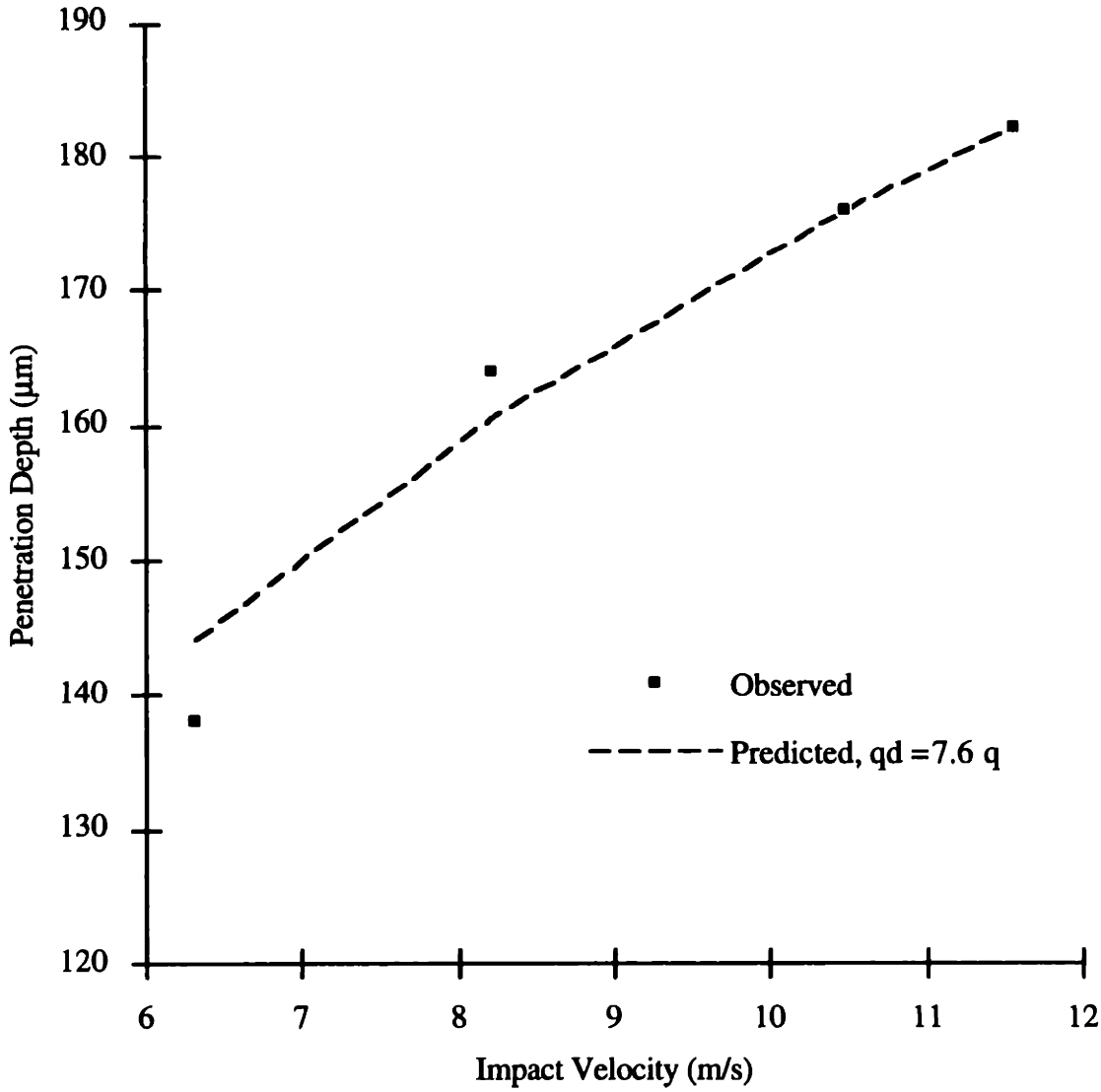

Figure 6.16 Impact penetration depth (predicted & measured) vs. the impact velocity (10 μm spherical alumina powder, k = 2.07 MPa/m).

The predicted and observed impact penetration depths for both 25 μm flaky alumina powder and 10 μm spherical alumina powder are summarized in Figure 6.17. The data for stainless steel powder evaluated at one level of impact speed is also included here.

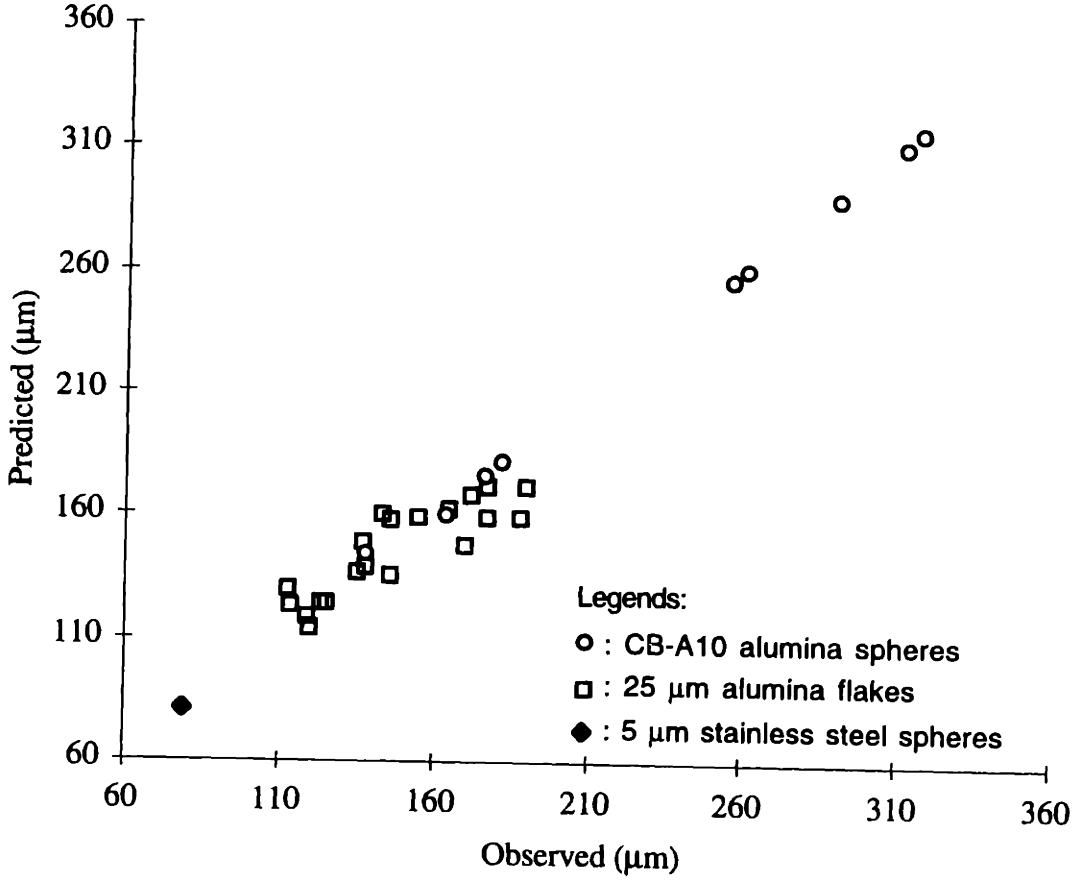

Figure 6.17 Predicted impact penetration depths vs. the experimentally observed depths.

6.6 An Investigation of the Inertial Effect

The model for predicting penetration depth, developed in Chapter 5 and tested in this chapter, recognizes two main factors which cause the deceleration of the drop -powder mixture during its penetration into the powder bed. One is the inertial factor, represented in the equation of motion, Equation 5.27, by $\rho_b \left(\frac{dz}{dt}\right)^2$. Since the liquid and powder are

capable of mixing with each other as the penetration progresses, the inertial effect is expressed through conservation of momentum, i.e. as the mass of the drop - powder increases due to accumulation of powder particles, the velocity of the body decreases. The second factor is q(z), which represents the powder bed's resistance to a penetrating body. As discussed in the last section, the dynamic stress at high strain rates can be a few times higher than in a quasi-static situations, and the dynamic stress scaling factor was estimated by trial calculations at one of the impact velocity. After this factor was thus estimated, it can be applied to other impact velocities in the investigated range.

We now consider the effects if the inertial term is also adjusted by a scaling factor. Hypothetically, this might be necessary in a situation where masses (powder particles) that are not in the moving body (the drop - powder mixture) were also accelerated to a velocity close to those in the drop - powder mixture. One such situation does exist and is studied in fluid mechanics. It is well known that, in order to accelerate a body inside a fluid, extra force is needed to accelerate the fluid which surrounds the body. For example, if the flow is solenoidal and a spherical body is accelerated in a liquid, then additional force is needed which equivalent to accelerate a liquid volume one-half the size of the sphere [White]. The "additional" mass is "virtual" mass, or hydrodynamic mass.

Simulations were run under this hypothetical scenario. Both the powder bed resistance and the mass terms were varied and their effects on the predicted penetration depth were examined. Figures 6.18 (for the 25 μm flaky alumina powder) and Figure 6.19 (for the 10 μm spherical alumina powder) show the typical results of these scenario runs. In each case, the effect of an increase in the mass term is to cause the prediction curve to deviate away from the experimentally evaluated penetration depth - impact velocity relationship. The curves become flatter, and the effect of velocity tends to be diminished. This behavior suggests that the inertial effect has been accounted for adequately in the original model. If there are particles outside the drop - powder mixture being accelerated, their number should be much smaller than the particles immersed in the drop - powder mixture, so they do not contribute significantly to the deceleration of the body of the mixture.

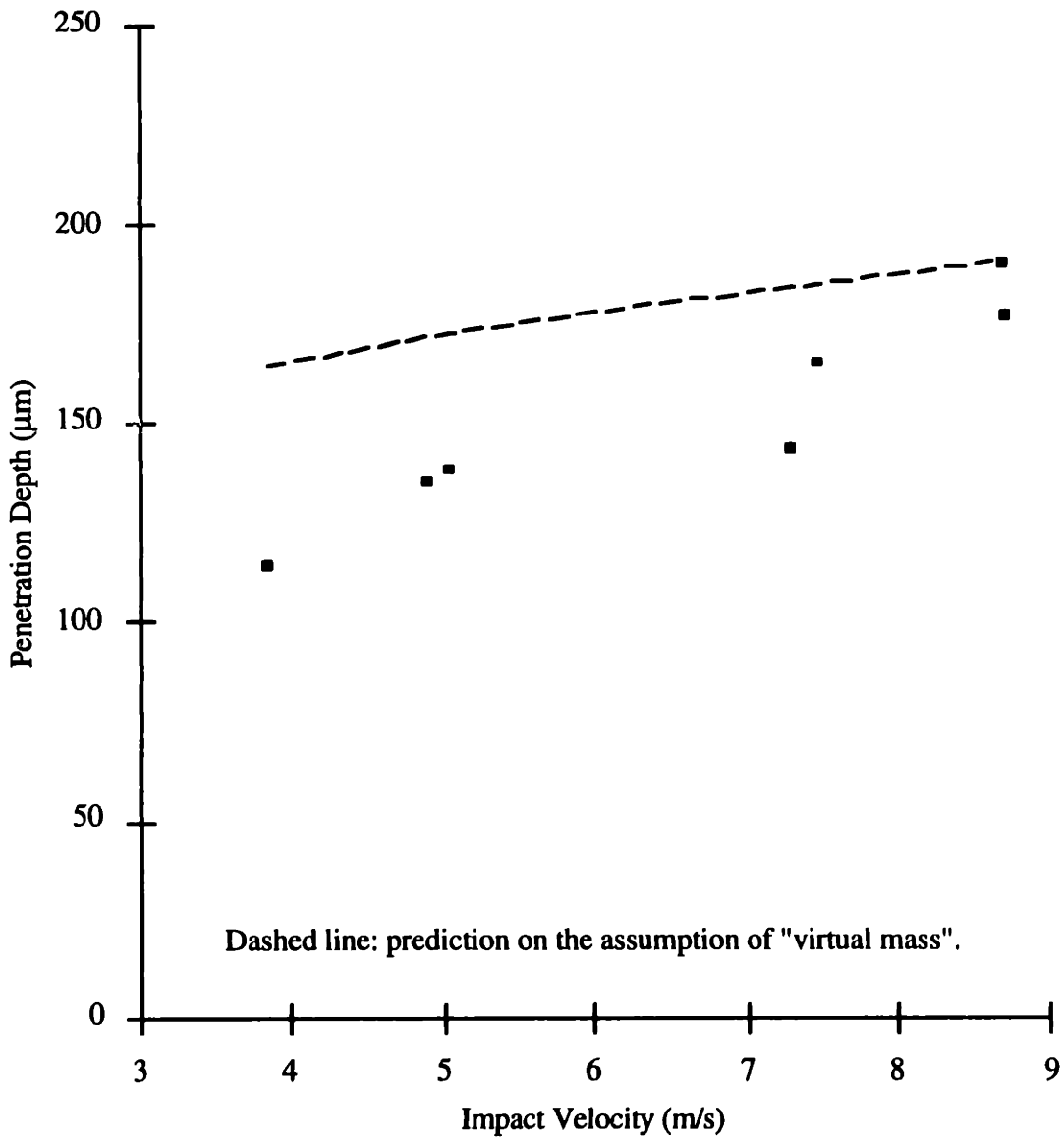

Figure 6.18 Simulation results for the investigation on inertial effect
(25 μm flaky alumina powder, k = 1.68 MPa/m)

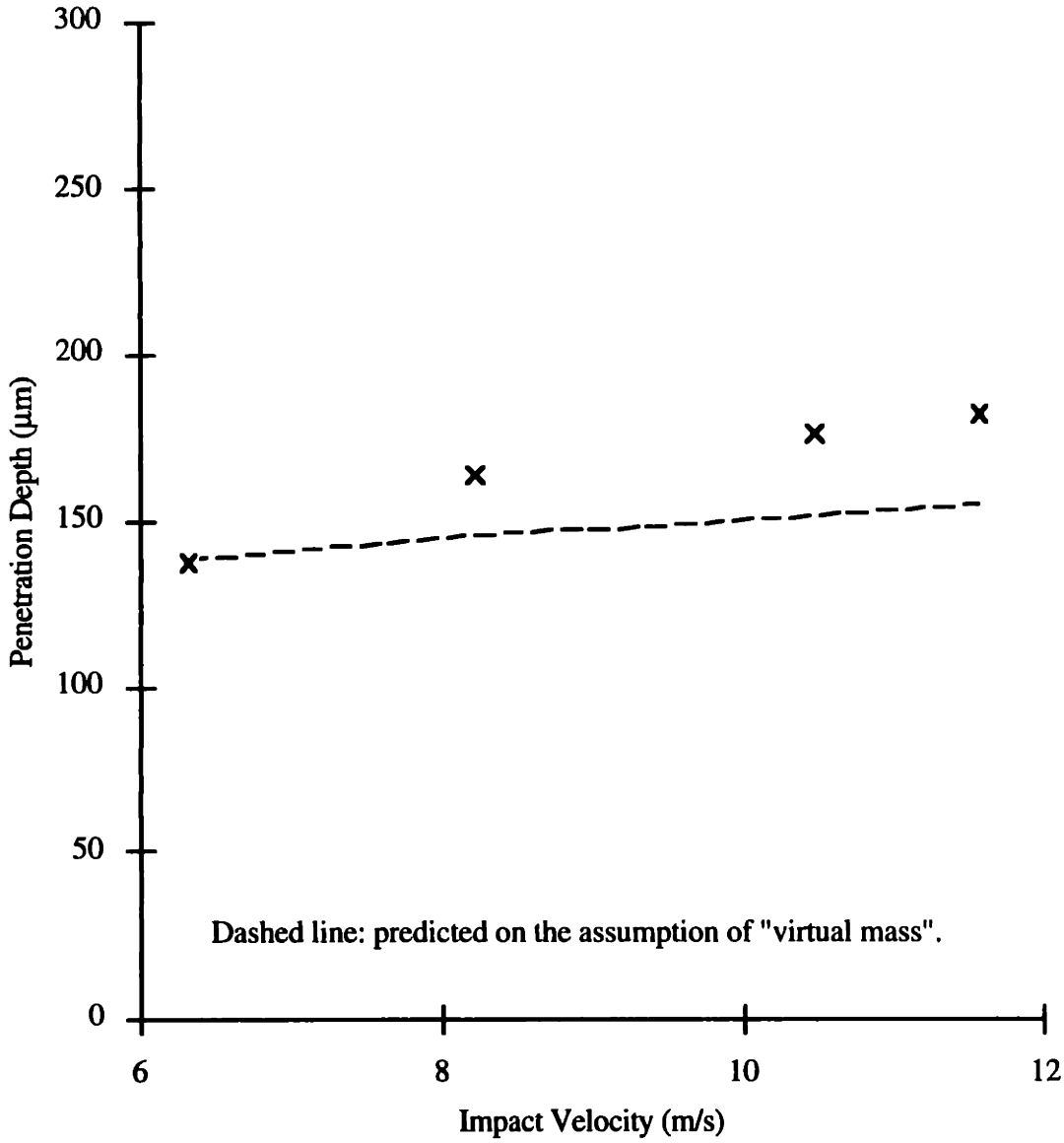

Figure 6.19 Simulation results for the investigation on inertial effect
(10 μm spherical alumina powder, k = 2.07 MPa/m)

6.7 Exploration of the Effect of Nozzle Size and Flow Rate on Penetration Depth by Simulation

Production rate and feature size, as discussed in Chapter 2, are two major considerations in selecting nozzle size for 3DP process. Production rate, or how much volume of powder is printed in unit time, is related to the volume flow rate of the liquid binder by the ratio of saturation, which should be kept constant. In order to raise production rate, the flow rate needs to be raised proportionally. Since flow rate is the product of the cross-sectional area of the nozzle, A, and the jet velocity, U, (Eq. 2.5), one or both of A and U needs to be increased.

Feature size, under given speed of raster scanning, depends on the size of the nozzle. Attaining smaller minimum feature size calls for using smaller nozzle. However, using smaller nozzle leads to higher droplet speed. The previous sections in this chapter presented experimental and simulation results showing that higher impact speed aggravates penetration when the droplet size is fixed. In a situation where the droplet size is changed corresponding to the change of droplet velocity, higher impact velocity may or may not result in deeper penetration, all depending on the specific combination of two parameters (size and speed). Using the penetration depth as a criterion for selecting operation parameter, the penetration model can be employed to explore the operation space specified in terms of flow rate, droplet size and speed.

Figure 6.20 shows results obtained by simulating the penetration using the single droplet impact model. Each curve is for a constant flow rate, ranging from 0.9 ml/min to 1.5 ml/min. The initial impact speed U is determined by Eq. 2.5, i.e.

$$U = \frac{Q}{\frac{1}{4}\pi d^2},$$

where Q is the flow rate and d is the diameter of the continuous stream, approximated by the diameter of the nozzle. For convenience, the two diameters are used interchangeably in the following discussion. It is assumed the jet is stimulated with a signal of the Rayleigh frequency (Eq. 2.3),

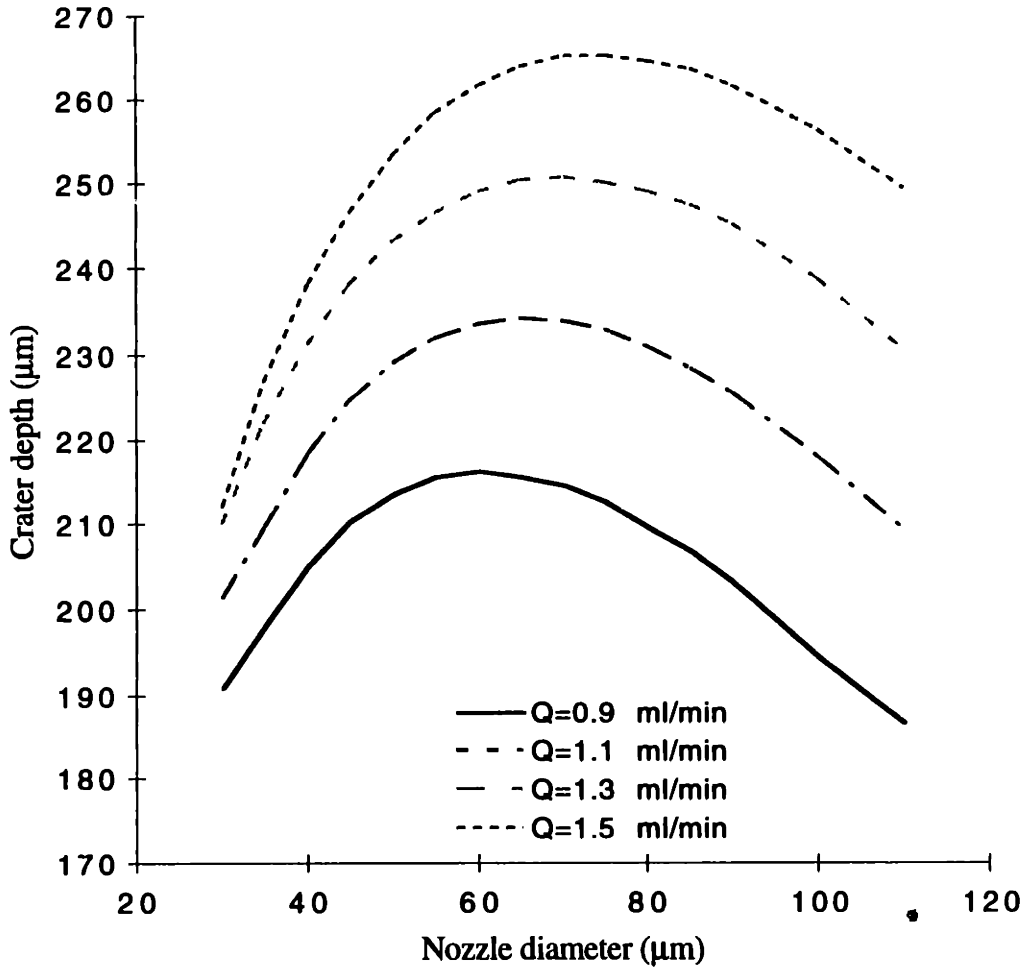

Figure 6.20 Nozzle size, volume flow rate and penetration depth.

$$f = \frac{U}{4.508\ d}.$$

The droplet diameter D, by Eq. 2.6,

$$D = 1.89\ d.$$

With the size and impact speed of the droplet known, the penetration depth is computed for a powder bed of the 10 μm spherical alumina powder.

The simulation results indicate that, at each level of flow rate and with the droplet diameter and speed both changing, the penetration depth increases with the nozzle size and reaches a maximum value, then declines with further increase of the nozzle size. For each flow rate, away from the maximal point, two different size nozzles can generate droplets to have the same penetration depth.

The nozzle size currently used in Three Dimensional Printing is about 40 μm, operated at a flow rate around 1.1 ml/min. According to the simulation results, further reduction of the nozzle size will cut back on the penetration. On the other hand, if it is desired to increase the nozzle size, for example, to get larger droplets, the nozzle diameter needs to be about 100 μm in order to keep the penetration depth at the current level. With nozzle diameter equal to 100 μm, the jet velocity would be about 4 times lower than the current value, down to the level of 2 to 3 meters per second. Aiming, or path perturbation of the droplet due to air flow is a major concern at this lower jet velocity range.

6.8 Conclusion

It has been shown, through comparing the results of simulation and experimental data, in this chapter that the penetration model of single droplet - loose powder bed impact developed in Chapter 5 is a useful tool for predicting the penetration depth in Three Dimensional Printing. The predicted relationship between penetration depth and impact velocity reflects well the experimentally observed relationship. The dynamic effect of powder bed resistance to an intruding aqueous droplet can be correlated to the powder bed's behavior in quasi-static penetration tests by impact test at one speed level. By combining this information with other readily available parameters of impact condition, the penetration depth can be predicted over the full speed range interested in Three Dimensional Printing to an accuracy comparable with the size of powder particles.

The simulation method based on this model can be used to explore the parameter space of printing conditions. Exploring such a space by experimental methods alone would be time consuming and expensive. By simulation it has been shown that the penetration

depth increases monotonically with flow rate of the liquid binder being printed. At each level of flow rate, assuming that the droplets are generated at the optimum (Rayleigh) frequency, the penetration depth reaches a maximum at a particular nozzle size. As the flow rate increases, the nozzle size yielding the maximum penetration depth also increases. This simulation tool helps to identify the proper operating points to satisfy requirements on flow rate, feature size and penetration depth.

CHAPTER 7

CONCLUSIONS

The principle of Three Dimensional Printing is selective binding of loose and fine solid particles into a solid form by precision placement of microscopic-sized liquid droplets into powder materials. Continuous jet printheads become the choice mechanism for binder delivery because of their potential in handling binders of high solid content and in meeting demands of industrial applications for high production rate and fine features. The high jet velocity associated with continuous jets makes droplet impact with loose powder particles an important issue in Three Dimensional Printing. This study recognized the connections between droplet impact and the quality of parts produced by Three Dimensional Printing, and identified various modes and major effects of droplet impact on powder beds. Extensive experiments have been carried out in this study to gain an understanding of the physical phenomena associated with impact between microscopic droplets and semi-infinite porous media consisting of fine particulate solids. The impact processes of single droplets of water on loose powder beds of hydrophilic materials were photographed and modeled for the first time. This study revealed the constructive aspect of such impact phenomena, i.e., the formation of particulate aggregates, in the Three Dimensional Printing process. This finding has led to a unique approach of modeling the cratering process of microscopic droplet impact on loose powder bed.

Even though inkjet printing techniques are commonly considered a category of non-impact printing technologies, the impact interaction between the ink droplets and the printing medium is an intrinsic aspect of any inkjet printing. With continuous media such as paper and film, the droplet reacts to the impact with large deformation and flow over the medium surface. In Three Dimensional Printing on a loose powder bed, the powder bed at the impact site also goes through substantial deformation, causing strong influences on the impact process as well as on the printing result. This study focused on a material system consisting of aqueous solutions and alumina particles. The droplets were of sizes a few tens of micrometers and the solid particles were of nominal sizes a fraction of the droplets'. The droplet speeds were around 10 meters per second, and the particles were laid down dry and not cemented before printing. It was found under these conditions that a single droplet

would form an aggregate of solid particles held together by the printed liquid in the pores, and that in the mean time the powder bed was deformed to create a crater, and that the crater wall was well separated from the printed powder conglomerate by a few micrometers. This gap cuts off the lateral path for the liquid to seep into the surrounding powders through capillary action, though not the path in the downward direction. In forming the powder aggregate, the particles underwent reorganization in packing, as evidenced by the orientation of particles over the surface. Overall the aggregate assumed a shape roughly spherical. This is the smallest structure that can be found in a part produced with Three Dimensional Printing, and thus defines the finest feature that can be created by the printing process. The size of this feature can be estimated by the volume of the droplet and the void ratio of the powder bed, or by using the void ratio inside the features, to be exact. Further reduction of the feature size requires reduction of the droplet size and powder size in accordance.

The small aggregate of powder particles can be extended into two dimensional figures by printing a train of droplets in a linear fashion with overlap in the droplet placement, and then by printing these lines close enough to each other to achieve line-to-line stitching, and obtaining a thin slice representing a cross section of the intended part. A part is built in the third dimension by accumulating these slices vertically and by relying on migration of the liquid binder for between-slice stitching. Parts built using linear droplet placement in powder beds which are not totally fixated display distinctively corrugated surfaces. This corrugated topography is a major factor contributing to the surface roughness of these parts. The surface roughness is aggravated when the powder beds are cohesionless where the particles are ejected and piled up irregularly as a result of jet impingement on these beds. Each of the three factors (corrugated topography, powder ejection and the geometry of individual particles and the packing of these particles) contributes to about one third of the roughness measured on the parts printed on loose powder beds with the material systems pertinent to this study. Methods of increasing the cohesive strength of the powder, some of which were investigated in this study, can effectively limit the particle movements and improve the surface texture. These methods have their side effects. Primitive features produced using these methods tend to be larger due to the lack of particle movement. In powder bed where the powder particles are totally kept from moving during printing, no gap is developed between the printed lines and its adjacent region, so that lateral percolation of the binder liquid is inhibited. Such sideward bleeding into unprinted area causes rougher side surfaces. This calls for finding effective measures, such as expediting the gelation of colloidal silica binder by lowering its pH value

once it gets into the powder bed, to contain the percolation while striking a balance to not compromise the line-to-line and layer-to-layer stitching, which depends on the percolation [Fan, 1990].

Surface quality of printed parts can be improved through other means such as alteration of printing pattern. Raster scanning, or linear continuous placement of droplets, is the first developed and still the most widely used printing pattern in Three Dimensional Printing, mainly because it requires minimum control on the jet. Additional capacities of controlling the droplet placement have been developed which, instead of simply turning the jets on and off, electrically charges the droplets to different levels. The droplets are deflected according to the charges they carry in a constant electrostatic field orthogonal to the rasters and fall on the powder bed around the scanning line to form desired patterns [Fan, 1990]. This technique of proportional deflection make it possible to adopt complicated droplet placement schemes to achieve smoother surfaces. One of such schemes is to create disjoint single primitive balls through each pass of scanning and then joining them together through multiple passes. This method is effective in diminishing the corrugated surface texture. In doing so the impact of single droplet on loose powder bed becomes the dominating printing mode. Questions such as how long it takes for a single droplet to form a powder aggregate and how far these aggregates penetrate into the powder bed are important ones to resolve in order to design the printing process on a rational basis.

The single impact of a water droplet on a loose powder alumina bed is a rapid and minute process. Typical printing conditions in Three Dimensional Printing have droplet diameter ca. 90 μm, impact speed ca. 10 m/sec., nominal powder sizes from 10 μm to 25 μm (with plenty of fine content), and powder bed packing ca. 40%. The impact deformation of the powder bed ceases within 1 ms. The crater formed has a rim diameter under 300 μm. The powder particle aggregate has a diameter around 160 μm; its bottom is at about 200 μm below the surface of the powder bed.

As shown by this study, it is possible to visualize and record this rapid and minute process with single frame stroboscopic photography by taking micrographs at sequentially delayed times. In order to assemble a series of photographs (with different droplets at different locations in the powder bed) to represent a single impact process, the powder sample needs to be prepared carefully to achieve the maximum uniformity possible. Instrumentation for measuring the speed of each individual droplet and for compensating

for speed variations, such as those required in this thesis, is also indispensable. To reveal the impact details in an opaque granulate medium, it is necessary to make the observation from the top of the powder bed. Containing the sample between glass walls and viewing the process from the side through the glass is not an option since the influences from the wall on the droplet, as well as on the particles, would be too great to be ignored in the domain under investigation.

The observations revealed that, under the conditions investigated, the formation of the aggregate (the intermingle of the liquid with the powder particles) and the formation of the crater (penetration of the liquid-powder mixture into the powder bed) occur simultaneously. Further analysis in this thesis, drawing results from several areas of research, has shown that this behavior is contingent on the physical and geometrical characteristics of the system involved. Among these characteristics are the highly hydrophilic nature of the particle surface, the impact speed of the droplet, the wetting-spreading speed of the liquid over the surface of the solid material, the large size of the droplet relative to that of the particles', the pore size, the low mechanical strength of the bed against impact, and in particular, the fact that loose, fine solid particles are dispersible in a wetting liquid. By comparison, a two-stage process (deformation/spreading and absorption) can be perceived for the impact between a droplet of large size and a surface of rigid porous medium.

The observations and analyses indicate that the mass increase of the evolving powder aggregate, starting with a single droplet and proceeding with the engulfing of solid particles into the liquid-powder mixture, is the dominating factor in the kinetics of the impact penetration. Meanwhile, the powder bed resistance to penetration reduces the momentum of the liquid-powder mixture. The resistance depends on the depth and speed of penetration, as well as the geometry of the penetrating body. The penetrating body, in the case under investigation, changes its size as more and more particles are engulfed. This in turn affects the rate of engulfing and the penetration resistance. Because high speed penetration into a cohesionless particular medium is not well understood in either soil mechanics or impact engineering, an empirical formulation relating the pressure to penetration depth was adopted, with modifications to take into account the strain rate effect.

These constituents were incorporated into a model to describe the movements of a liquid-powder mixture formed from a single droplet into a loose powder bed. The

penetration depths of powder aggregates formed from single droplets were obtained as results of numerical simulations.

Equipment was built and experiments were carried out to collect data on penetration depths at varied conditions of droplet size, impact speed, powder material, and powder bed stiffness. The observed penetration depths were compared with predictions given by the model. The results show that the predictions tend to overestimate the penetration depth if the penetration resistance is calculated based on penetration resistance-depth curves acquired through quasi-static tests. The over-estimate could be nearly 30% at low impact speeds. The strain rate effect of the penetration resistance-depth relation of powder beds was evaluated experimentally. Such evaluations can be performed at any droplet impact speed within the experimented range. Predictions with the corrected penetration resistance-depth relations showed much improved accuracy, and fitted well with the experimental results. Thus it is concluded that the model indeed captures the major aspects of the mechanisms governing the impact penetration. The simulation method based on the model developed in this thesis can be used as a tool to explore the space of operation parameters for process optimization.

Bibliography

Adamson, Arthur W.(1990) Physical Chemistry of Surfaces, 5th ed., Wiley, New York.

Al-Durrah, M.M. and Bradford, J.M. Parameters for describing soil detachment due to single waterdrop impact. Soil Science Society of America Journal **46** (1982) 836 - 840.

Allen, William A. and Mayfield, Earle B. and Morrison, Harvey L. Dynamics of a projectile penetrating sand. Journal of Applied Physics **28** (1957) 370 - 376.

Allen, William A. and Mayfield, Earle B. and Morrison, Harvey L. Dynamics of a projectile penetrating sand, Part II. Journal of Applied Physics **28** (1957) 1331 - 1335.

Anderson, Charles E., Jr. An overview of the theory of hydrocodes. Int. J. Impact Engineering. **5** (1987) 33 - 59.

Asai, Akira and Shioya, Makoto and Hirasawa, Shinichi and Okazaki, Takeshi. Impact of an ink drop on paper. Journal of Imaging Science and Technology **37** (1993) 205 - 207.

Bargmann, Heinz W. The mechanics of erosion by liquid and solid impact. International Journal of Solids Structures **29** (1992) 1685 - 1698.

Bekker, M.G.(1969) Introduction to Terrain Vehicle Systems. University of Michigan Press, Ann Arbor.

Billington, E.W. and Tate, A. (1981) The Physics of Deformation and Flow. McGraws-Hill, New York.

Bredt, James Frederic. Binder Stability and Powder/Binder Interaction in Three Dimensional Printing (Ph.D thesis). MIT. 1995.

Cazabat, Anne-Marie. How does a droplet spread? Contemporary Physics **28** (1987) 347 - 364.

Chandra, S. and Avedisian, C.T. On the collision of a droplet with a solid surface. Proc. R. Soc. London. A **432** (1991) 13 - 41.

Clyens, S. and Johnson,W. International Journal of Mechanical Science **19** (1977) 745 - 752.

Crandall, Stephen H. and Karnopp, Dean C. and Jurtz, Edward F., Jr. and Pridmore-Brown, David C. (1968) Dynamics of Mechanical and Electromechanical Systems. Robert E. Krieger, Malabar.

de Genne, P.G. Wetting: statics and dynamics. Review of Modern Physics **57** (1985) 827 - 863.

Dear, J.P. and Field, J.E. High-speed photography of surface geometry effects in liquid/solid impact. Journal of Applied Physics **63** (1988) 1015 - 1021.

Denesuk, M. and Smith, G.L. and Zelinski, B.J.J. and Kreidl, N.J. and Uhlmann, D.R. Capillary penetration of liquid droplets into porous materials. Journal of Colloid and Interface Science **158** (1993) 114 - 120.

Fan, Tailin. Three Dimensional Printing group literature. 1990.

Fan, Tailin, Lauder A., Sachs, E., and Cima, M. The surface finish in Three Dimensional Printing. Proceedings of the Third International Conference on Rapid Prototyping. University of Dayton, Ohio. 1992

Field, J.E. and Dear, J.P. and Orgren, J.E. The effects of target compliance on liquid drop impact. Journal of Applied Physics **65** (1989) 533 - 540.

Forrestal, M.J. and Luk, V.K. Penetration into soil targets. International Journal of Impact Engineering **12** (1992) 427 - 444.

Goldsmith, Werner. (1960) Impact: the Theory and Physical Behavior of Colliding Solids. Edward Arnold, London.

Goriatchkin, B.P., et al. (1936) Theory and Production of Agricultural Equipment. Moscow.

Harlow, F.H. and Shannon, J.P. The splash of a liquid drop. Journal of Applied Physics **38** (1967) 3855 - 3866.

Hinds, William C. (1982) Aerosol Technology: Properties, Behavior, and Measurement of Airborne Particles. John Wiley & Sons, New York.

Hohler, V. and Stilp, A.J. (1990) Long-Rod Penetration Mechanics. Chapter 5 of High Velocity Impact Dynamics. Edit. by Jonas A. Zukas. John Wiley & Sons, New York.

Huang, Y.C. and Hammit, F.G. and Yang, W.-J. Hydrodynamic phenomena during high-speed collision between liquid droplet and rigid plate. Journal of Fluids Engineering, Transactions of ASME **95** (1973) 276 - 294.

Iler, Ralph K. (1979) The Chemistry of Silica : Solubility, Polymerization, Colloid and Surface Properties, and Biochemistry . Wiley, New York.

Israelachvili, Jacob (1992). Intermolecular & Surface Forces, 2nd ed., Academic Press, Boston.

Jaeger, H.M. and Nagel, Sidney R. Physics of the granular state. Science **255** (1992) 1523 - 1531.

Johnson, W. (1972) Impact Strength of Materials. Edward Arnold, London.

Kendall, Kevin. Adhesion: molecules and mechanics. Science **263** (1994) 1720 - 1725.

Kralchevsky, P.A. and Paunov, V.N. and Ivanov, I.B. and Nagayama, K. Capillary meniscus interaction between colloidal particles attached to a liquid-fluid interface. Journal of Colloid and Interface Sciences **151** (1992) 79 - 94.

Lauder, A., Fan, Tailin, Cima, M., and Sachs, E. Three Dimensional Printing: surface finish and microstructure of rapid prototyped components. Synthesis and Processing of Ceramics: Scientific Issues. Boston, MA. 1991.

Liu, Chu-heng and Nagel, Sidney R. Sound in sand. Physics Review Letters **68** (1992) 2301 - 2304.

Loehr, K.F. and Lasek, A. Splashing of drops. Archives of Mechanics **42** (1990) 507 - 513.

Lord Rayleigh. On the capillary phenomena of jets. Proc. R. Soc. **29** (1879) 71 - 97.

Marmur, Abraham. Penetration and displacement in capillary systems of limited size. Advances in Colloid and Interface Science **39** (1992) 13 - 33.

Marmur, Abraham. Penetration of a small drop into a capillary. Journal of Colloid and Interface Science **122** (1988) 209 - 219.

Marmur, Abraham. The radial capillary. Journal of Colloid and Interface Science **124** (1988) 301 - 308.

Michaels, Steve. Three Dimensional Printing group literature. 1994.

Mitchell, James K. (1993) Fundamentals of Soil Behavior, 2nd edi. John Wiley & Sons, New York.

Nelson, Ralph D. Jr. (1988) Dispersion Powders in Liquids. Elsevier, New York.

Nicholas, Theodore and Recht, Rodney F. (1990) Introduction to Impact Phenomena. Chapter 1 of High Velocity Impact Dynamics. Edit. by Jonas A. Zukas. John Wiley & Sons, New York.

Panuccio, C.M. and Wayne, R.C. and Selig, E.T. Investigation of a plate index test for railroad ballast. Geotechnical Testing Journal **1** (1978) 213 - 222.

Paunov, V.N. and Kralchevsky, P.A. and Denkov, N.D. and Nagayama K. Lateral capillary forces between floating submillimeter particles. Journal of Collid and Interface Science **157** (1993) 100 - 112.

Reynolds, Osburne. Scientific Papers, Vol. 2 pp. 535 and 563.

Sachs, Emanuel M., Michael Cima, James Bredt, Alain Curodeau, Tailin Fan, and David Brancazio, CAD casting: direct fabrication of ceramic shells and cores by Three Dimensional Printing. Manufacturing Review **5** (1992) 117 - 126.

Savic, P. and Boult, G.T. (1955) The fluid flow associated with the impact of liquid drops with solid surfaces. National Research Council of Canada. Report No. Mt-26.

Stebnovskii, S.V.. Characteristics in the initial stage of the spreading of a drop on a solid surface. Journal of Applied mechanics and Technology Physics **20** (1979) 66 - 69.

Stow, C.D. and Hadfield, M.G. An experimental investigation of fluid flow resulting from the impact of a water drop with an unyielding dry surface. Proc. R. Soc. London. A **373** (1981) 419 - 441.

Stow, C.D. and Stainer, R.D. The physical products of a splashing water drop. Journal of the meteorological Society of Japan **55** (1977) 518 - 532.

Stringer, G.S. (1976) Erosion by Liquid Impact. Scripta Publishing Company, Washington DC.

Stulov, L.D. and Murashkevich, F.I. and Fuchs, N. The efficiency of collision of solid aerosol particles with water surfaces. Journal of Aerosol Science **9** (1978) 1 - 6.

Terzagi, K. and Peck, R.B. (1948) Soil Mechanics in Engineering Practice. John Wiley & Sons, New York.

Wachters, L.H.J. and Westerling, N.A.J. The heat transfer from a hot wall to impinging water drops in the spherical state. Chemical Engineering Science **21** (1966) 1047 - 1056.

Washburn, Edward W. The dynamics of capillary flow. The Physical Review, 2nd Series **17** (1921) 273 - 283.

White, Frank M. (1986) Fluid Mechanics. 2nd edi. McGraw-Hill, New York.

Wright, T.W. and Frank, K. Approaches to penetration problems. In Impact: Effects of Fast Transient Loadings, (edit. Ammann, Wing Kam Liu, Jost A. Studer and Thomas Zimmermann), Proceedings of the First International Conference on Effects on Fast Transient Loadings. Lausanne, August 26 - 27, 1987.

Wu, T.H. (1971) Soil Dynamics. Allyn and Bacon.

Yankelevsky, D.Z. Analysis of impact and penetration to geomaterials using engineering models. In Impact: Effects of Fast Transient Loadings, (edit. Ammann, Wing Kam Liu, Jost A. Studer and Thomas Zimmermann), Proceedings of the First International Conference on Effects on Fast Transient Loadings. Lausanne, August 26 - 27, 1987.

Zukas, Jonas A. (1990) Introduction to Penetration Mechanics. Chapter 4 of High Velocity Impact Dynamics. Edit. by Jonas A. Zukas. John Wiley & Sons, New York.

Zukas, Jonas A. (1990) Survey of Computer Codes for Impact Simulation. Chapter 9 of High Velocity Impact Dynamics. Edit. by Jonas A. Zukas. John Wiley & Sons, New York.

Appendix I

Size Distribution of Alumina Powders

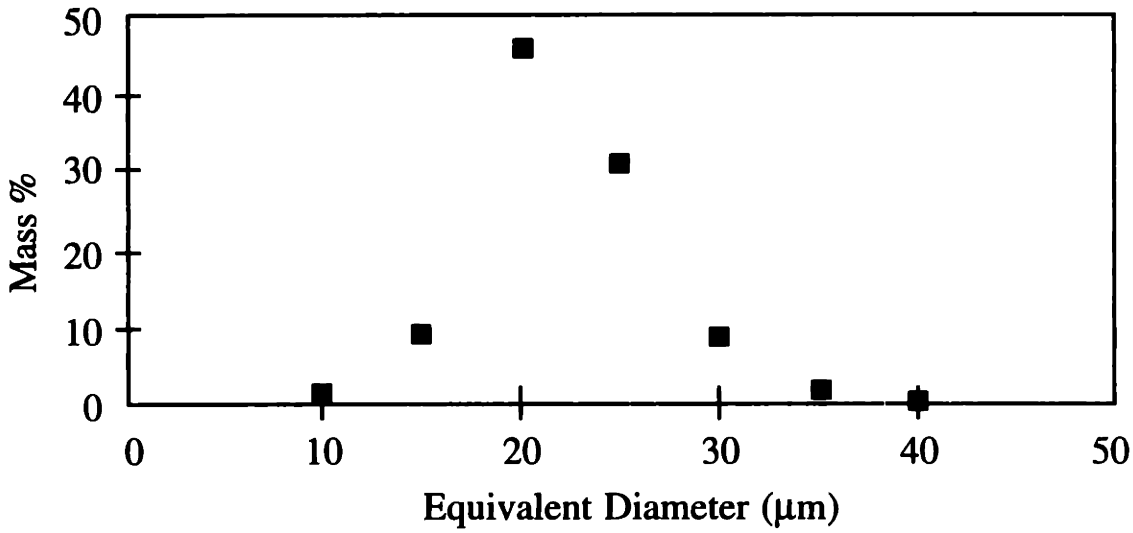

Electronic grade alumina flakes (Norton), nominal size: 25 μm

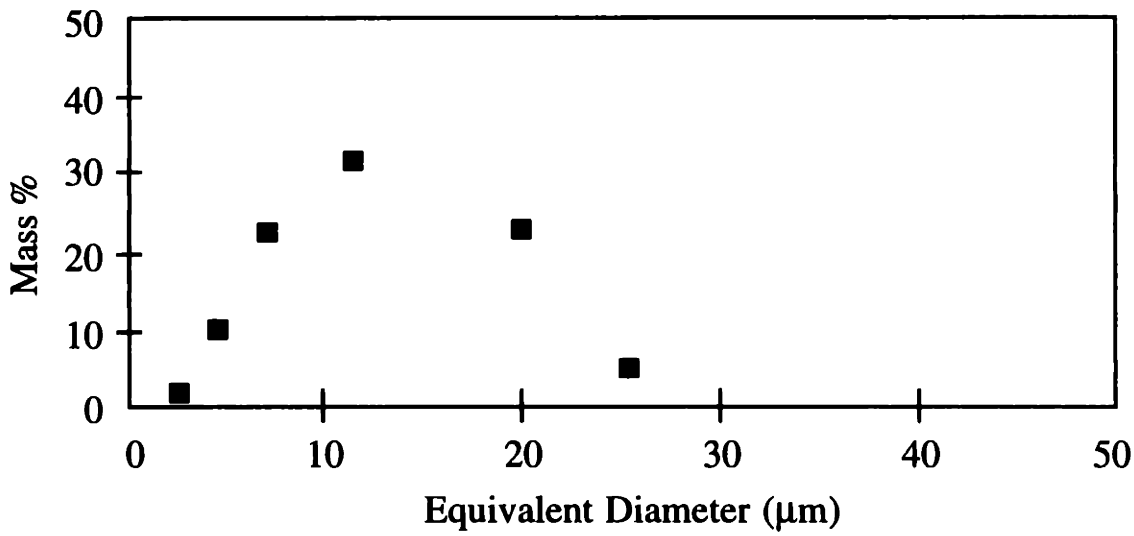

Alunabeads® alumina spheres (ICD), nominal size: 10 μm

Figure AI-1 Powder size distributions

Appendix II

Inertial Engulfing of a Solid Particle by a Moving Droplet

An important observation made in Chapter 5 is that in equilibrium state a small alumina particle should be engulfed by a water droplet. Stebnovskii's experiment showed that the initial spreading of a wetting liquid over a solid surface is rapid. So the engulfing of a micrometer-sized particle through wetting takes only microseconds.

It can be shown that, as long as the solid particle is not hydrophobic, the engulfing of a 10 μm-diameter alumina particle by a 80 μm-diameter water droplet is still a rapid process. This is mainly because the small particle, though pushed and accelerated by the droplet, moves much slower than the liquid and is quickly overtaken by it. We will show that by inertia alone is enough to effect engulfing of a particle by a moving droplet under the discussed conditions.

To simplify this order-of-magnitude assessment, we ignore the hydrophilic nature of alumina particles, i.e. we assume that the surface energy condition neither promote nor inhibit the spreading of water over the particle surface. Since wetting quickens the engulfing, assessment based on this simplification underestimates the rate of engulfing. To make the assessment of the rate of engulfing even more conservative, we over-estimate the force causing the particle to accelerate by assuming that it equals the stagnant pressure multiplied by the maximum cross-section area of the particle. The stagnant pressure derives from the speed difference between the liquid and the particle, $U_o - u_p$. Another simplification is to assume that $U_o - u_p$ is also the speed at which the liquid flows around the particle. Since the mass of a 10 μm diameter alumina sphere is 1/128 of the mass of a 80 μm diameter water droplet, it is accurate enough to ignore the velocity change of the liquid in the calculation here. Figure AII-1 depicts such an encounter between a droplet and a solid sphere.

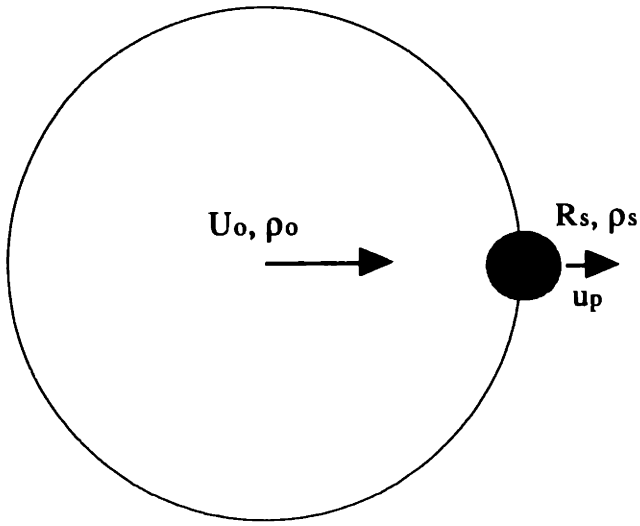

Figure AII-1 Inertial engulfing of a solid particle.

The acceleration of the solid particle is

$$\frac{du_p}{dt} = \frac{\text{Force on particle}}{\text{particle mass}} = \frac{\frac{1}{2}\rho_o(U_o - u_p)^2 \pi R_p^2}{\rho_p \frac{4}{3}\pi R_p^3} = \frac{3}{8}\frac{\rho_o}{\rho_p R_p}(U_o - u_p)^2 \qquad \text{(AII-1)}$$

where ρ is for density, R is for radius, U and u are for velocity, subscript o and p are for the droplet and the particle respectively.

Let t = 0 at the first moment the droplet touches on the particle, the displacement of the droplet, s, at time t is

$$s(t) = U_o t - \frac{8}{3}\frac{\rho_p R_p}{\rho_o} \ln\left(\frac{3}{8}\frac{\rho_o U_o}{\rho_p R_p} t + 1\right).$$

So by that time the liquid catches on the particle by the amount of

$$\Delta(t) = U_o t - s(t) = \frac{8}{3}\frac{\rho_p R_p}{\rho_o} \ln\left(\frac{3}{8}\frac{\rho_o U_o}{\rho_p R_p} t + 1\right). \qquad \text{(AII-2)}$$

The droplet engulfs the particle totally when $\Delta(T) = 2\ R_p$. From Eq. AII-2, this occurs at the time $t = T$,

$$T = \frac{8}{3} \frac{\rho_p R_p}{\rho_o U_o} \left[e^{\left(\frac{3}{4} \frac{\rho_o}{\rho_p}\right)} - 1 \right]. \qquad \text{(AII-3)}$$

In the example case, $R_p = 5\ \mu m$, $\rho_p/\rho_o = 4$ and $U_o = 10$ m/sec. Estimated by Eq.AII-3, the engulfing takes 1.1 μs, which is only 10% longer than the time for a 10 m/sec droplet moves over a distance of 10 μm. Over this period, the particle moves less than one micron.

According to Eq. AII-1, smaller particles accelerate and move faster than larger particles. So that as a droplet moves into a loose powder bed, it tends to carry the smaller particles further and leaves the larger ones behind. This type of particle separation is observable on close examination of printed primitives.

Appendix III

Powder Bed Resistance to the Pellet Movement

After the penetrating pellet geometry is simplified to a sphere and the penetration - resistance relation of the powder bed resistance is linearized with respect to the penetration depth, the external force acting on the pellet can be readily obtained. The contact area between the pellet and the powder bed is not constant, because (1) the size of the pellet increases as solid particles are incorporated into the pellet, and (2) before half of the pellet enters the powder bed, the presentation area increases with the penetration depth as shown in Figure AIII-1.

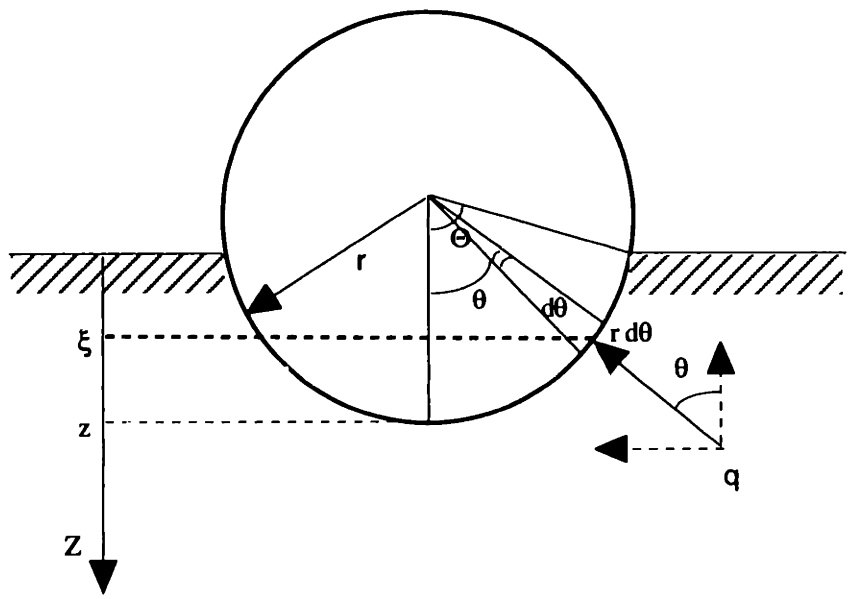

Figure AIII-1 Resistance to a penetrating pellet of liquid-powder mixture.

Suppose the sphere's bottom has reached depth z. The angle spanned by the crown buried in the powder bed at this moment is $\Theta = \cos^{-1}\frac{z - r}{r}$, where r is the radius of the pellet. As shown in Chapter 5 the pressure from the granular medium to a penetrating body, q, can be approximated by $q = K \xi^n$, where ξ is the depth of a point at which the pressure is calculated. The total force on the crown is:

$$F = \int_0^{\Theta} 2\pi K r^2 \sin\theta \cos\theta \, [z - r(1 - \cos\theta)]^n d\theta. \qquad \text{(AIII-1)}$$

It has been shown in Chapter 5 that for shallow depth n = 1 is a good approximation to the penetration curve. With n = 1, Equation AIII-1 has closed form solution,

$$F = 2\pi K r^2 \{ \int_0^{\Theta} (z - r) \sin\theta \cos\theta \, d\theta + r \int_0^{\Theta} \sin\theta \cos\theta^2 \, d\theta$$

$$= 2\pi K r^2 \{ \frac{z - r}{2} \sin^2 \Theta + \frac{r}{3}(1 - \cos^3\Theta) \}. \qquad \text{(AIII-2)}$$

With $\Theta = \cos^{-1}\frac{z - r}{r}$, Eq. AIII-2 becomes

$$F = \pi K r^2 (z - r) \, [1 - (\frac{z - r}{r})^2] + \frac{2\pi K r^3}{3} \, [1 - (\frac{z - r}{r})^3],$$

which can be simplified to

$$F = \pi K r^2 (z - r) + \frac{2\pi K r^3}{3} + \frac{\pi K (r - z)^3}{3}$$

$$= \pi k r^2 z - \pi k r^3 + \frac{2\pi K r^3}{3} + \frac{\pi K}{3} [r^3 - 3r^2 z + 3rz^2 + z^3]$$

$$F = K\pi z^2 (r - \frac{z}{3}) . \qquad \text{(AIII-3)}$$

Equation AIII-3 applies when $z \leq r$. When $z = r$, $F = \frac{2\pi K r^3}{3}$.

For $z \geq r$, $\Theta = \pi/2$. Equation AIII-2 becomes

$$F = K\pi r^2 (z - \frac{r}{3}) . \qquad \text{(AIII-4)}$$